Streamwise Homogeneous Turbulent Boundary Layers

Thesis by
Joseph Y. Ruan

In Partial Fulfillment of the Requirements for the
Degree of
Doctor of Philosophy

CALIFORNIA INSTITUTE OF TECHNOLOGY
Pasadena, California

2021
Defended 05/26/2021

Joseph Y. Ruan
ORCID: 0000-0002-9110-0458

ACKNOWLEDGEMENTS

First and foremost, I must thank my advisor, Prof. Guillaume Blanquart. His support and drive were fundamental to the results of this work.

I also would like to thank the members of my committee, Profs. Tim Colonius, Beverly McKeon and Melany Hunt for all of their input. Special thanks to both Tim and Beverly, who provided invaluable input on the different analytical tools used in this thesis.

The rest of my thanks is dedicated to Anna, and my friends and family. This would not have been possible without your support.

ABSTRACT

Boundary layers are everywhere and computing direct numerical simulations (DNS) of them is crucial for drag reduction. However, traditional DNS of flat-plate boundary layers are prohibitively expensive. Due to the streamwise inhomogeneity of the boundary layer, simulations of spatially growing boundary layer simulations require long domains and long convergence times. Current methods to overcome streamwise inhomogeneity (and allow for shorter streamwise domains) either suffer from a lack of stationarity or have difficult numerical implementation. The goal of this thesis is to develop and validate a more efficient method for simulating boundary layers that will be both statistically stationary and streamwise homogeneous.

The current methodology is developed and validated for the flat plate, zero pressure gradient, incompressible boundary layer. The Navier-Stokes equations are rescaled by a boundary layer thickness to produce a new set of governing equations that resemble the original Navier-Stokes equations with additional source terms. Streamwise homogeneity and statistical stationarity are verified through non-periodic and periodic simulations, respectively. To test the accuracy of the methodology, a sweep of Reynolds number simulations is conducted in streamwise periodic domains for $Re_{\delta^*} = 1460 - 5650$. The global quantities show excellent agreement with established empirical values: the computed shape factor and skin friction coefficient for all cases are within 3% and 1% of empirical values, respectively. Furthermore, to obtain accurate two-point correlations, it is sufficient to have a computational domain of length $14\delta_{99}$ and width $5\delta_{99}$, thus, leading to large computational savings by one-to-two orders of magnitude. This translates into increasing the largest possible Reynolds number one could simulate by about a factor of 3.

Thanks to the streamwise homogeneous nature of the simulation results, it is now possible to apply cost-efficient data-driven techniques like spectral proper orthogonal decomposition (SPOD; Towne *et al.* 2018) to extract turbulent structures. Particular emphasis is place on identifying structures for waves in the inner and outer layers. To interpret these structures, 1D resolvent analysis (McKeon & Sharma 2010) is leveraged. The peak location for the extracted inner wave is captured by traditional resolvent analysis, assuming a parallel flow. However, the peak location for the extracted outer wave differs from that predicted by the classic 1D resolvent analysis by 20%. Recovering the peak location requires including in the resolvent operator the mean wall-normal velocity profile and the streamwise growth of the boundary

layer.

This methodology has natural extensions to slowly growing boundary layer flows, including thermal boundary layers, rough wall boundary layers and mild pressure gradient flows.

PUBLISHED CONTENT AND CONTRIBUTIONS

[1] J. Ruan and G. Blanquart. "Direct numerical simulations of a statistically stationary streamwise periodic boundary layer via the homogenized Navier-Stokes equations". In: *Physical Review Fluids* 6.2 (Feb. 2021). DOI: 10.1103/physrevfluids.6.024602.
The author of this thesis developed the methodology, performed the simulations, prepared the data, and wrote the manuscript.

[2] J. Ruan and G. Blanquart. "Error estimation of one-point statistics of a homogenized streamwise periodic boundary bayer". In: *Physical Review Fluids* (Under Review).
This manuscript is currently under review. The author of this thesis developed the methodology, performed the simultations, prepared the data, and wrote the manuscript.

TABLE OF CONTENTS

LIST OF ILLUSTRATIONS

Number *Page*

LIST OF TABLES

Chapter 1

INTRODUCTION

1.1 Background

It would be little exaggeration to say that climate change and environmental sustainability may well be one of the defining problems of the century. With increasing air tourism, and the fact that the aviation industry contributes at minimum 2% [1] of the total CO_2 emissions globally, efficiency in air travel plays an important role in reduction of greenhouse gas emissions. While there are concerted efforts to discover and implement alternative fuels, in the mean time, drag reduction, especially for aircrafts, remains a key component of carbon reduction strategies. It is also in direct alignment with the financial interests of aviation industries. Fuel costs make up nearly 15-20% [2] of total costs for aircrafts and even a 10% difference in fuel efficiency can result in millions of dollars saved. Minimizing drag will always serve as a key motivator for increased study into wall-bounded flows.

But what causes drag to begin with? Drag is proportional to the shear stress at the wall

$$\tau_w = \mu \frac{\partial \overline{u}_1}{\partial x_2}|_{x_2=0} \tag{1.1}$$

where τ_w is the wall shear stress, μ the kinematic viscosity of the fluid, $\overline{u}_1$, the ensemble averaged streamwise velocity component, and x_2 is the wall-normal location centered at the wall. From an inspection of this equation, one finds that the critical aspect to drag is the mean velocity gradients at the wall. Because fluids are capable of undergoing near infinite amounts of shear, effectively being capable of sticking to a surface (called the *no slip* condition), a continuous velocity gradient is induced between the free-stream and the surface. Strong gradients lead to stronger skin friction. These gradients are strongly intensified by orders of magnitude as the boundary layer transitions from a laminar regime to fully developed turbulence. Throughout the years, creative designs to reduce drag have been tested, whether through variated roughness on the wall, linear control of wall-normal jets, or other changes to wall conditions [3–5]. These methods have been shown to decrease drag from as little as 5% and even up to 20% under various conditions [4]. Unfortunately, such methods are often either Reynolds number-specific or dependent on other conditions such as pre-existing pressure gradients and wall curvature. Reducing drag

on ship freighters has been shown to potentially reduce fuel usage by over 20%, [5] and there is potential for similar gains for commercial aircrafts as well.

1.1.1 The zero-pressure gradient boundary layer

Boundary layers develop in many complex conditions and are highly sensitive to (1) heat transfer effects, (2) pressure gradients, and (3) roughness. Each of these variables provides yet another dimension that compounds the difficulty in simulating the flow. Naturally, the most fundamental turbulent boundary layer studied is that of the incompressible zero-pressure gradient smooth flat plate turbulent boundary layer (IZPGSFPTBL). However, even the study of the most fundamental boundary layer remains difficult due to one key feature: streamwise inhomogeneity.

Streamwise inhomogeneity remains the key roadblock especially for numerical simulations of boundary layer flow. Provided this hurdle is overcome, simulations with heat transfer, pressure gradients, and roughness will be more forthcoming. Consequently, this thesis will focus on developing and validating methods specifically for overcoming streamwise inhomogeneity effects in IZPGSFPTBL as a proof-of-concept. Descriptions are given in Chapter 6 (the conclusion) for how one can use this method to potentially include heat transfer, pressure gradient, and roughness effects.

But what about streamwise inhomogeneity makes boundary layer study so difficult? To answer this question, we must first describe boundary layer flows' nearest fundamental relative: channel flows.

Channel flows are flows between two infinite, parallel flat plates, driven by a streamwise pressure gradient. They share similarities with boundary layers in that near the wall, there is a thin layer of high shear due to the "no slip" condition mentioned previously. The key distinction is that canonical channel flows are statistically homogeneous in the streamwise direction, usually interpreted analytically and incorporated in simulations as streamwise periodic boundary conditions. This simple observation reduces several of the complexities of the governing equations. Channel flows are also fully internal flows and so boundary conditions can often be more conveniently specified than for external flows.

The analogy between channel and boundary layer flows near the wall is often tantalizingly good. The mean streamwise velocity profiles even share many of the same features: a near-wall viscous sublayer, a logarithmically growing mean velocity (known as the log layer), and then a wake far from the wall. In the inner

layer, where growth of the boundary layer is logarithmically slow, the boundary layer often behaves similarly to channel flow. Turbulent streaks have been found in both flows, often with long streamwise lengths and near the wall, the heartbeat of turbulent structures, sometimes referred to as the "engine of turbulence" [6] are quite similar. A set of similarity variables near the wall ($u_\tau = \sqrt{\tau_w/\rho}, \delta_\nu = \mu/(\rho u_\tau)$, where ρ is fluid density) can be used to scale both profiles to overlap in the viscous sublayer ($x_2/\delta_\nu \lesssim 5$), the buffer layer ($5 \lesssim x_2/\delta_\nu \lesssim 30$), the mesolayer ($30 \lesssim x_2/\delta_\nu \lesssim 300$), and nearly overlap in the log layer (collectively called the inner region). Although there have been arguments for whether profile in the log layer differs by $1-2\%$ [7], the overall qualitative agreement is quite clear.

Differences, however, manifest once out of the log layer. Boundary layers are inherently streamwise inhomogeneous and grow. The rapid growth of the outer scale δ_{99}, or the height where the mean streamwise velocity ($\overline{u}_1$) profile reaches 99% of the free-stream velocity, extends the boundary layer deep into a quiescent free-stream. This entrains irrotational flow from the free-stream to continuously enter the boundary layer, drastically changing the biome of turbulent structures present in the flow. Channel flows, on the other hand, are not quiescent anywhere in the domain, even far from the wall. Coles (1956) showed that the boundary layer features an extensive wake will encompass a large and roughly consistent portion of the boundary layer, which is far different from channel flow far-wall behavior.

Even comparisons of inner layer statistics between channel and boundary layer flows face difficulties. Usually, comparisons are made by matching the channel flow friction Reynolds number $Re_\tau^{channel} = h/\delta_\nu$, where h is the channel half-height, with the boundary layer friction Reynolds number $Re_\tau = \delta_{99}/\delta_\nu$. This Reynolds number is an indicator of so-called "scale separation" as δ_{99} is representative of the largest structures in the flow and δ_ν is representative of the smallest structures of the flow. The majority of channel flow is dominated by inner-scaling (with δ_ν, u_τ). It has even been argued, based on log layer location and thickness [9], that the two Reynolds numbers for comparison should in fact be $Re_\tau^{channel}$ and $Re_{\delta^*} = \rho\delta^* u_{1,\infty}/\mu$, where $\delta^* = \int_0^\infty (1-\overline{u}_1/u_{1,\infty})dx_2$ is the displacement thickness. However some of the largest channel simulations have been at $Re_\tau^{channel} \approx 5000$ and have a log layer spanning at least a decade in x_2/δ_ν, whereas boundary layer simulations at $Re_{\delta^*} \approx 5000$ barely have any indication of a logarithmic layer. Difficulty reaching high enough Reynolds numbers to observe asymptotic behavior (similar to channel flows) is a key hurdle yet to overcome for boundary layers.

The streamwise growth of the boundary layer is directly due to presence of a quiescent free-stream and a solid wall. The combination of these boundary conditions imposes several restrictions on analytical methods. The boundary layer also requires careful tripping methods, and in all cases, long streamwise extents are needed. One must always keep in mind that the current visible turbulent behaviors were potentially caused upstream under the circumstances of a different Reynolds number. Convergence also becomes a limiting factor. Specifically, the growth of the boundary layer forces the expansion of the flow and drastically changes different mean quantities, like drag and the shape of the mean velocity profiles. For example, a boundary layer can have a 10% change in Reynolds number over the course of $10\delta_{99}$. It has been shown [10, 11] that there is remarkable scatter in boundary layer data. These restrictions carry over to simulations research as well. Due to streamwise inhomogeneity, the methods and expectations of channel flow do not always translate well to boundary layers, thus potentially stunting boundary layer research.

1.2 Numerical limitations and difficulties

Numerically, the difference between the two flows becomes more stark. Boundary layers are often simulated in the streamwise growing regime and often require inflow conditions. As mentioned previously, boundary layers often have an origin as well a distance from their transition to turbulence. The simulation of transition is often expensive and can span large swathes of simulation domain. The most common methods to avoid simulating transition have injected flows with either synthetic turbulence [12] or using recycling and rescaling [13], where flow is taken from an upstream plane, rescaled, and used as an inlet plane. The costs for the latter can be upwards of 25% of the streamwise domain, if not longer, and in general the costs for both can reach 30% of the streamwise domain as turbulence from any inflow requires recovery from the inlet [14].

Costs from the recycling-rescaling operation have been notably high especially due to spurious linking in the observed turbulent structures [15]. To relax periodic linking, the recycle domain is often further extended [14, 16]. However, as noted by [16], the impact of periodicity can still seen even $30\delta_{99,\text{inlet}}$ from the inlet.

Additionally, wall-bounded domains require long streamwise extents to fully capture turbulent structures of length $20\delta_{99}$ [17–20], known as very-large-scale motions (VLSMs). These turbulent structures remain controversial and it has been argued by [21, 22] that the longer structures in shortened domains still exist, but aliased

into "linked" structures, and that the very-large-scale-motions (VLSM) are merely spanwise meandering structures of much shorter length $O(3-4\delta_{99})$. While these arguments serve as *a priori* justifications for shorter streamwise domains, the general consensus has been to err on the side of caution, usually requiring domains much longer than potentially necessary.

There are further difficulties with respect to computational implementation. As the boundary layer grows in space ($d\delta^*/dx_1 > 0$), momentum is displaced away from the wall, and mass leaves through the top surface of the computational domain ($u_{2,\infty} > 0$). This transpiration velocity is an often overlooked boundary layer quantity. Because it is small compared to the free-stream velocity ($u_{2,\infty} \sim 0.005u_{1,\infty}$), it is difficult to resolve in experimental data and overall difficult to validate numerically. Moreover, to enforce global mass conservation in incompressible DNS, an *a priori* streamwise dependence of $u_{2,\infty}$ must be imposed over the entire domain[13, 14, 18]. The imposition of $u_{2,\infty}$ consequently enforces a particular boundary layer growth rate. This is easily seen by integrating continuity ($u_{2,\infty} = u_{1,\infty}\frac{d\delta^*}{dx_1}$). Under these conditions, one might ask if boundary layer simulations with fixed growth rates are even true DNS.

The high simulation cost makes it difficult for boundary layer simulations to consistently reach higher Reynolds number, reaching at most $Re_\tau \approx 4000$ [23], using a staggering 34 billion grid points. A smaller (but still impressively large) boundary layer simulation (4 billion grid points) by Wu *et al.* (2017) took over 5 calendar years to complete. A similar boundary layer simulation by Orlu *et al.*(2013) (3 billion grid points) used over 9 million cpu-hours. Pushing the Reynolds number limit faces further difficulties. The numerical grid requirements scale with $Re_\tau^{9/4}$, and it isn't any exaggeration to say that some of the most expensive simulations conducted have been boundary layer simulations.

Beyond increasing Reynolds number simulations, a new age of data-driven techniques [25, 26] has emerged, owing to significant advances in numerical efficiency and storage space. These techniques have proven crucial in understanding behavior in pipe flows, jets, channel flows, and more [27–29]. The goal of each of these techniques is to extract the underlying motions inherent to the flow and the governing mechanisms for them. The largest turbulent structures are known to contain over 50% of turbulent kinetic energy [9], and for the purposes of drag reduction, they can have serious impacts on the near wall behavior. It has been found that part of the reason many of the current drag reduction methods work is that they interfere

with the development of coherent structures near the wall [30, 31].

All of these discoveries require terabytes if not petabytes of data. Because turbulent flow is near-stochastic, gigabytes of data are already needed to converge one-point statistics, but terabytes of data are often needed to converge time-averaged two-point statistics. While there are plenty of methods that focus on extracting spatially coherent structures (proper orthogonal decomposition), the clear focus has been on temporally and spatially developing structures, thus increasing the data storage hurdle. In addition, the different data-driven techniques scale with the number of data points: superlinearly at minimum and potentially quadratically at worst.

How popular are these data-driven methods with respect to boundary layers? At the moment, there are several early applications of these methods, specifically for transition [32]. The application of proper orthogonal decomposition, spectral proper orthogonal decomposition (SPOD) and dynamic mode decomposition (DMD) for turbulent structure extraction tends to become prohibitively expensive. For simulations similar in size to Orlu (2013), each data file is at minimum 100 GB. For popular and trusted data-driven techniques such as DMD, and SPOD, there are heavy requirements for the number of data files needed for 2D inhomogeneous flows, on the order of 10,000 data files. In contrast, streamwise homogeneous flows like pipe and channel flows do not require as many data files and have been shown to use even 3000 data files effectively [27]. Shorter streamwise domains (for pipe and channel flows) also reduce storage size by at least an order of magnitude, making the overall endeavor much more manageable.

The dual concerns of high Reynolds flow behavior and turbulent structure extraction for boundary layer flows are critical to this thesis. The key issue preventing advancement is the streamwise inhomogeneity of the boundary layer.

1.3 Historical treatment of streamwise periodicity

To combat the high computational expense of a growing boundary layer, scientists developed methods to impose streamwise periodicity. Some of the earliest studies [33, 34] have focused on running boundary layer simulations that were periodic for short periods of time. This methodology was known, by the community, as the Temporal DNS.

Domains would often be roughly $(3-6\delta_{99})$ in streamwise length, $(1-3\delta_{99})$ in width and $(2-3\delta_{99})$ in height [33, 34] . More recent methods [35] have focused on running simulations with larger streamwise and spanwise extent to contain more turbulent

structures. As the name implies, the TDNS do not reach statistical stationarity. While the flow produces profiles that are quantitatively and qualitatively accurate, the convergence leaves much to be desired. When imposing periodic boundary conditions on a boundary layer, it can be readily shown from the governing equations that the boundary layer grows in time. Specifically, the displacement thickness grows at a rate of $u_{1,\infty}^{-1}\partial_t\delta^* = 1/2C_f = \tau_w/(\rho u_{1,\infty}^2)$.

The idea of the TDNS was to conduct the simulation as if in a moving frame of reference (at a speed of $u_{1,\infty}$). In this frame of reference, the free-stream would stay constant while the wall would move in the opposite direction, and a boundary layer would form in time. Conceptually, the strength of this method was that, with a limited domain size, one could potentially reach higher Reynolds numbers. With the added benefit that boundary layers grow "slowly" (as mentioned, the nondimensionalized displacement thickness growth rate is $1/2C_f \sim O(10^{-3})$), the boundary layer may remain at the desired Reynolds number long enough for statistics to be sampled [33].

These methods however, do not meet modern standards for convergence. For most growing boundary layers, the eddy turnover time $\delta_{99}/u_\tau \approx 100\delta^*/u_{1,\infty}$. Ideally a streamwise simulation would be sampled over at least one eddy turnover time. Assuming a skin friction coefficient $C_f \approx 2\times10^{-3}$, over a single eddy-turnover time, the boundary layer thickness would have had a relative growth of 10%. For TDNS, there is little time ($0.1\delta_{99}/u_\tau$) to actually converge statistics before the Reynolds number has changed by over 1%. Modern standards often call for sampling times for a single Reynolds number of at least $10\delta_{99}/u_\tau$, about two orders of magnitude larger than that possible by the TDNS. Although modern TDNS can boast larger streamwise domains ($O(10\delta_{99})$) [35], the improvement in convergence is not nearly enough to make up for the severe lack in overall convergence.

To counteract statistical transience, Spalart & Leonard (1985) developed a technique to leverage self-similarity. For example, the mean streamwise velocity profile has the following inner layer and outer layer self-similar scalings

$$\overline{u}_1 = u_\tau f_i(x_2/\delta_\nu) \qquad \overline{u}_1 = u_\tau f_o(x_2/\delta_{99}) + u_{1,\infty} \tag{1.2}$$

where f_i, f_o are the inner and outer layer similarity functions, respectively. A wall-normal coordinate η would match $x_2^+ = x_2/\delta_\nu$ in the inner layer ($x_2^+ < 15$) and match x_2/δ_{99} in outer layer ($x_2 > 0.1\delta_{99}$). The simulation would then be solved following

coordinates of η. The multiple velocity scales $u_\tau, u_{1,\infty}$ also have streamwise growth rates and their growth terms were included in the coordinate transformation.

The method furthermore decomposed streamwise derivatives into "fast" and "slow" derivatives, which allowed for a different set of source terms than conventional coordinate transformations. Then, the authors implemented different rescalings for the mean and turbulent fluctuations. Each layer involved different source terms of different types, each with requirements for closure. To solve for the "slow" and "fast" growth terms instantaneously, a linear system based on the log law and integrated streamwise momentum equation was solved at each time-step. Finally, to handle the nonlinear change of η between the inner and outer regions, a "switching" function was used in the "log layer" at a prescribed x_2^+.

Although complicated, the method would allow one to focus on a specific Reynolds number throughout the simulation and furthermore avoid simulating all previous Reynolds number prior to it. The resulting simulation was statistically stationary and produced both two-point and one-point statistics that, for its time, were surprisingly accurate, given the modern perspective of how the simulations were heavily under-resolved with $\Delta x_1^+ \approx 20, \Delta x_3^+ \approx 10$. However, the near wall rms profiles for various Reynolds numbers did not collapse under inner-scaling (scaling velocities with u_τ and length-scales with δ_ν). At the time the authors considered the complicated rescaling of the fluctuations to be the cause of issues and that perhaps the computation of the metrics related to the "slow-growth" and "fast-growth" terms were not accurate enough.

Consequently, a new method was developed by Spalart in 1987. Multiple periodic boundary layer stations were chosen to be simulated. The first station at a low Reynolds number, would be simulated using the previous method. Stations at higher Reynolds numbers would compute the "slow" derivatives using the values already established at the lower Reynolds number. For example, partial differentiation in the streamwise coordinate of δ_ν would be given by $\partial_{x_1}\delta_\nu = (\delta_{\nu,\text{station1}} - \delta_{\nu,\text{station2}})/(x_{1,\text{station1}} - x_{1,\text{station2}})$, where the difference in streamwise locations would be estimated by $1/2C_f \approx \partial_{x_1}\theta \approx (\theta_1 - \theta_2)/(x_{1,\text{station1}} - x_{1,\text{station2}})$, for constant kinematic viscosity ν, and free-stream velocity $u_{1,\infty}$.

The simulations would increase their Reynolds number in a consecutive manner. Again, for its time and resolution limits, there was agreement of mean and rms profiles with experimental profiles. The study even showed that at the spanwise and wall-normal rms velocity profiles show limited inner-scaling.

Another key issue became apparent: in order to simulate larger Reynolds number flows with this method, one would have to simulate several streamwise stations with lower Reynolds numbers. As it became increasingly more straightforward to directly simulate the entire boundary layer, Spalart's method soon fell out of favor since the computational savings would become nearly negligible. The idea of streamwise periodic boundary layers would largely fall by the wayside, and with it, its ability to drastically reduce simulation cost.

1.4 Objectives and outline

The key limiting problem for boundary layer simulations is the streamwise inhomogeneity of the boundary layer. For both the hopes of achieving higher Reynolds numbers, and being able to apply state-of-the-art data extraction techniques, a computational framework allowing streamwise homogeneity is critical. To develop such a technique, we limit ourselves to the study of the incompressible, zero-pressure gradient, smooth flat-plate boundary layer. This thesis focuses employing streamwise periodicity via a single length-scale rescaling of the Navier-Stokes equations and validates the simulation of streamwise periodic boundary layer flows. This thesis has the following objectives:

1. Develop a new rescaling method that vastly simplifies Spalart's (1987) method for the restricted case of the smooth flat-plate boundary layer.

2. Quantify performance of the new method from *a priori* and *a posteriori* perspectives with respect to one-point statistics.

3. Describe how the method behaves with high Reynolds number behavior and quantify how the method affects sensititve parameters like transpiration velocity $u_{2,\infty}$.

4. Prescribe computational domain size recommendations.

5. Investigate turbulent structures either predicted via resolvent analysis [38] or extracted from data sets via spectral proper orthogonal decomposition [25].

This thesis has the following structure. The governing equations, corresponding simulations, and results are presented in Chapter 2, fulfilling Objectives 1 and 2. Portions of Objecitve 3 are satisfied by the investigation of the transpiration velocity for the periodic boundary layer in Chapter 3. The rest of Objective 3 and Objective

4 are completed in Chapter 4 in descriptions of the two-point correlations. Finally, Chapter 5 fulfills Objective 5.

Chapter 2

DIRECT NUMERICAL SIMULATIONS OF A STATISTICALLY STATIONARY STREAMWISE PERIODIC BOUNDARY LAYER VIA THE HOMOGENIZED NAVIER-STOKES EQUATIONS

[1] J. Ruan and G. Blanquart. "Direct numerical simulations of a statistically stationary streamwise periodic boundary layer via the homogenized Navier-Stokes equations". In: *Physical Review Fluids* 6.2 (Feb. 2021). DOI: 10.1103/physrevfluids.6.024602.

There is currently no computational framework for the simulation of boundary layers that is 1) statistically homogeneous in the streamwise direction, 2) statistically stationary, and 3) fully closed. The objective of the present work is to propose a new framework to improve on Spalart's preliminary method such that it does not rely on auxiliary simulations for closure. The overall concept remains the same: to use periodic boundary conditions and a scaling enforced by a coordinate transformation to keep the boundary layer statistically stationary.

We will detail the principles of the transformation in Section 2.1 and conduct extended domain simulations in Section 2.2 to justify streamwise statistical homogeneity. We highlight the numerical methods in Section 2.3. In Section 2.4, we present validation and comparisons to DNS data from Refs. [39] and [14] and empirical fits by Refs. [10, 11]. Finally, in Section 2.5, we discuss computational savings.

2.1 Analysis of stationary boundary layer

The goal of this section is to describe the new proposed method of simulating flat plate turbulent boundary layers. It begins with a description of the spatial transformation, and a discussion of the simplifications leading to the final set of equations.

2.1.1 Transformation of the Navier-Stokes equations

The flat plate turbulent boundary layer is analyzed in the Cartesian coordinate system using index notation such that the velocity components in the Cartesian streamwise (x_1), wall-normal (x_2), and spanwise (x_3) directions are u_1, u_2, and u_3 respectively.

With pressure and density as P and ρ, respectively, the incompressible Navier-Stokes equations for mass and momentum conservation are

$$\frac{\partial u_j}{\partial x_j} = 0 \tag{2.1}$$

$$\frac{\partial u_i}{\partial t} + u_j \frac{\partial u_i}{\partial x_j} = -\frac{1}{\rho}\frac{\partial P}{\partial x_i} + \nu \frac{\partial^2 u_i}{\partial x_j^2} \tag{2.2}$$

We now apply a coordinate transformation from x_i to ξ_i which rescales the wall-normal coordinate by a streamwise varying C^2 function $q = q(x_1)$.

$$\xi_1 = x_1 \qquad \xi_2 = \frac{q_0}{q} x_2 \qquad \xi_3 = x_3 \tag{2.3}$$

where $q_0 = q(x_0)$ is a normalization constant that is yet to be determined. Applying this coordinate transformation directly to the Navier-Stokes equations yields the following set of equations for mass and momentum conservation.

$$\frac{\partial u_j}{\partial \xi_j} = \xi_2 \frac{q'}{q}\frac{\partial u_1}{\partial \xi_2} + H_c \tag{2.4}$$

$$\begin{aligned}\frac{\partial u_i}{\partial t} = -u_j \frac{\partial u_i}{\partial \xi_j} - \frac{1}{\rho}\frac{\partial P}{\partial \xi_i} + \nu \frac{\partial^2 u_i}{\partial \xi_j^2} + \xi_2 \frac{q'}{q} u_1 \frac{\partial u_i}{\partial \xi_2} \\ + H_p(u_i) + H_\nu(u_i)\end{aligned} \tag{2.5}$$

where

$$H_c = \left(1 - \frac{q_0}{q}\right)\frac{\partial u_2}{\partial \xi_2} \tag{2.6}$$

$$\begin{aligned}H_p(u_i) = \delta_{1i}\frac{1}{\rho}\frac{q'}{q}\xi_2 \frac{\partial P}{\partial \xi_2} + \\ \left(\frac{q - q_0}{q}\right)\left(\delta_{2i}\frac{1}{\rho}\frac{\partial P}{\partial \xi_2} + u_2 \frac{\partial u_i}{\partial \xi_2}\right)\end{aligned} \tag{2.7}$$

$$\begin{aligned}H_\nu(u_i) = \nu\left[1 - \left(\frac{q_0}{q}\right)^2 + \left(\xi_2 \frac{q'}{q}\right)^2\right]\frac{\partial^2 u_i}{\partial \xi_2^2} \\ + \nu\left[2\left(\frac{q'}{q}\right)^2 - \frac{q''}{q}\right]\xi_2 \frac{\partial u_i}{\partial \xi_2} - 2\nu\xi_2 \frac{q'}{q}\frac{\partial^2 u_i}{\partial \xi_1 \partial \xi_2}\end{aligned} \tag{2.8}$$

where δ_{ij} is the delta-Dirac function, H_c is an additional continuity term, H_p contains convective and pressure additional metric terms, and H_ν contains the viscous metric

terms. The equations as shown are exact and equivalent to the original Navier-Stokes equations. At the moment, $q(x_1)$ still requires a closure equation for the transformed Navier-Stokes equations to be complete. There are several possible choices to choose from such as the 99% boundary layer thickness δ_{99}, the displacement thickness δ^*, and the momentum thickness θ. Each choice yields a unique and mathematically valid coordinate transformation.

2.1.2 *a priori* analysis

We perform a budget analysis of the streamwise and wall-normal momentum equations Eq. 2.4-2.7 and the turbulent kinetic energy equation Eq. C.1-C.4. This *a priori* analysis is performed using the DNS data from Ref. [14] near $Re_{\theta_0} = 4000$.

Any *a priori* analysis of Eq. 2.4-2.7 requires estimates for the function $q(x_1)$. This function is here approximated by $\theta(x_1)$, and justification for the estimate will be given in Section 2.1.4. Empirical fits from [10] provide value for $\frac{\theta'}{\theta}\theta_0$ at $Re_{\theta_0} = 4000$.

We start with the streamwise momentum equation. First, we evaluate all terms at $q = q_0$. This reduces H_p to a single term, removes a term from H_ν, and completely eliminates H_c. We also group the main convective terms, $C_{NS} = u_1\partial u_1/\partial\xi_1 + u_2\partial u_1/\partial\xi_2 + u_3\partial u_1/\partial\xi_3$, and the main viscous terms, $V_{NS} = \nu(\partial^2 u_1/\partial\xi_1^2 + \partial^2 u_1/\partial\xi_2^2 + \partial^2 u_1/\partial\xi_3^2)$. The source term for this equation is given by $Src = q'/q\xi_2 u_1\partial u_1/\partial\xi_2$. Figure 2.1a shows the budget analysis of the streamwise momentum equation. All terms have been first averaged over time and spanwise coordinate, represented by $\langle\cdot\rangle_{\xi_3,t}$, and then the inner-scaled absolute values of these averages are plotted. Notably, the main convective terms the wall to balance the main viscous terms and the source term is not dominant.

As expected, the most dominant terms are the convective and viscous terms, C_{NS} and V_{NS}. Furthermore, Fig. 2.1a shows that the convective metric term $\xi_2 u_1\,(q'/q)\,\partial u_1/\partial\xi_2$ is the most dominant of the additional metric terms. It balances the main convective terms near the end of the logarithmic region and throughout the wake region ($80 < \xi_2^+ < 2000$). In contrast, the viscous metric term H_ν is over six orders of magnitude smaller than the streamwise convective term throughout the entire boundary layer. Similarly, the H_p term is at least three orders of magnitude smaller than the streamwise convective metric term until the end of the wake region near the free-stream. From an *a priori* perspective, the neglecting of H_ν and H_p is justified.

One can also apply a similar analysis to the wall-normal momentum equation. In

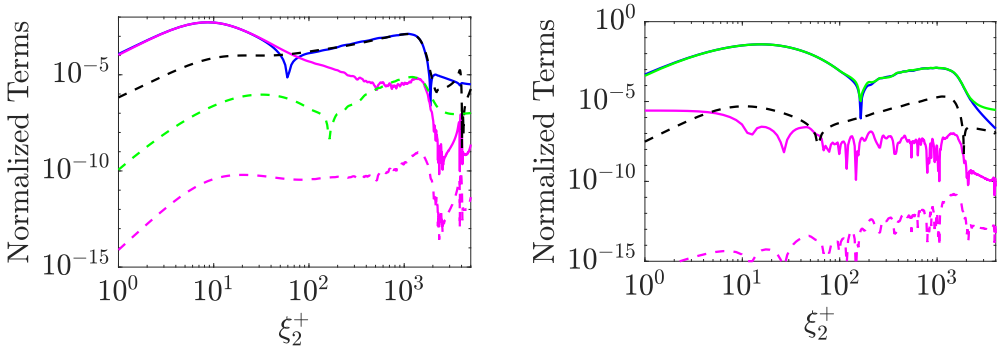

(a) streamwise momentum budget

(b) wall-normal momentum budget

Figure 2.1: Budgets of (a) streamwise momentum and (b) wall-normal momentum equations from DNS data (Ref. [14]). Lines: (solid black) $\langle C_{NS}\rangle_{\xi_3,t}$; (solid magenta) $-\langle V_{NS}\rangle_{\xi_3,t}$; (solid green) $\langle P_{NS}\rangle_{\xi_3,t}$; (dashed black) $-\langle Src\rangle_{\xi_3,t}$; (dashed green) $-\langle H_p\rangle_{\xi_3,t}|$; (dashed magenta) $-\langle H_\nu\rangle_{\xi_3,t}$.

this case, the convective terms are bundled as $C_{NS} = u_1\partial u_2/\partial\xi_1 + u_2\partial u_2/\partial\xi_2 + u_3\partial u_2/\partial\xi_3$, and the main viscous terms are collected in $V_{NS} = \nu(\partial^2 u_2/\partial\xi_1^2 + \partial^2 u_2/\partial\xi_2^2 + \partial^2 u_2/\partial\xi_3^2)$. The remaining terms are the mean pressure gradient term $P_{NS} = 1/\rho\partial P/\partial\xi_2$ and the source term $Src = q'/q\xi_2 u_1\partial u_2/\partial\xi_2$. Figure 2.1b shows the budget analysis of the wall-normal momentum equation. Again, all terms have been first averaged over time and spanwise coordinate, and then the inner-scaled absolute values of these averages are plotted.

In this case, the balance between the pressure and the convective terms dominates the entire budget. The magnitude of the source term is between that of the convective and viscous terms. The viscous metric term remains 7 orders of magnitude smaller than the pressure and convective terms throughout the boundary layer and thus can justifiably be neglected in the wall-normal momentum equation. Near the free-stream ($\xi_2^+ > 2000$), the source term and the convective term balance the pressure gradient term.

Finally, one can apply a similar analysis to the turbulent kinetic energy equation (Appendix A.3) and track relative contributions of the H_p, H_ν and the source term. The results are shown in Fig. 2.2. The metric source term contribution balances the turbulent advection term which is at least three orders of magnitude below the dominant budget terms. Throughout the boundary layer, the contributions of both H_ν and H_p to the kinetic energy budget remain several orders of magnitude lower than the dominant budget terms. From an *a priori* perspective, their impact on turbulent intensities is negligible.

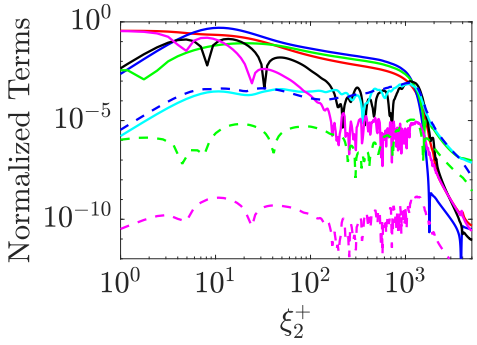

Figure 2.2: Mean turbulent kinetic energy budget from DNS data (Ref. [14]). Lines: (solid black) Turbulent production, (red) Dissipation, (green) pressure diffusion, (black) Turbulent diffusion, (cyan) advection, (magenta) Viscous diffusion, (dashed green) H_p contribution, (dashed magenta) H_ν contribution, (dashed black) metric source term contribution.

2.1.3 Streamwise variation of source terms

The previous subsection presented an *a priori* budget analysis of the governing equations for a specific streamwise location $x_1 = x_0$. The net conclusion was that for this particular streamwise location, H_p, H_ν and H_c are negligible in comparison to the other terms in the governing equations. However, it is also important to quantify the streamwise extents for which the terms H_c, H_p, H_ν remain negligible.

The time and spanwise averaged H_c term is given by

$$\left(1 - \frac{q_0}{q}\right) \frac{\partial \langle u_2 \rangle_{\xi_3,t}}{\partial \xi_2} \tag{2.9}$$

In order for H_c to be negligible, the ratio of H_c to dominant terms in continuity must be small. Specifically, one can compute the ratio of H_c to the gradient of mean wall-normal velocity and find that it is $1 - q_0/q(x_1) \approx q_0'/q_0\xi_1$. Following the same approximation that $q \sim \theta$, then $q_0'/q_0 \approx \theta_0'/\theta \approx 1/2C_{f,0}/\theta_0$. For $Re_{\theta_0} = 4000$, $C_f \approx 3\times10^{-3}$. For a ratio of 10% , one can have a streamwise extent of $\xi_1 \approx x_0 \pm 60\theta_0$ and for a 1% ratio, one can have a streamwise extent of $\xi_1 \approx x_0 \pm 6\theta_0$. Since the skin friction coefficient slowly decays with Reynolds number, for increasing Reynolds number, this streamwise extent is only expected to increase.

The time and spanwise averaged $H_p(u_i)$ term is provided by

$$\langle H_p(u_i) \rangle_{\xi_3,t} = \underbrace{\left(1 - \frac{q_0}{q}\right) \left\langle \left(\delta_{2i} \frac{1}{\rho} \frac{\partial P}{\partial \xi_2} + u_2 \frac{\partial u_i}{\partial \xi_2} \right) \right\rangle_{\xi_3,t}}_{\text{Term 1}} + \underbrace{\delta_{1i} \left\langle \frac{1}{\rho} \frac{q'}{q} \xi_2 \frac{\partial P}{\partial \xi_2} \right\rangle_{\xi_3,t}}_{\text{Term 2}} \tag{2.10}$$

It's easy to estimate the magnitude of Term 1 because it has the same analytical form of terms currently in the momentum equations. In the mean streamwise momentum equation, Term 1 simplifies to the Reynolds shear stress scaled by $1-q_0/q$. Following a similar argument as for H_c, it can be shown that Term 1 is less than 10% of the dominant Reynolds shear stress term for a streamwise extent of $120\theta_0$ centered on x_0. The pressure gradient term $((1 - q_0/q)/\rho\partial P/\partial\xi_2)$ in H_p only appears in the wall-normal momentum equation and can be directly compared to the wall-normal pressure gradient term. Again, a streamwise extent of $120\theta_0$ centered on x_0 is sufficient to keep the magnitude of this term an order of magnitude less than the other terms in the wall-normal momentum equation.

Term 2 has no immediate analogue in the streamwise momentum equation for direct comparison. To estimate term 2, we follow von Kármán (1930) and approximate the mean wall-normal pressure gradient in Cartesian coordinates by

$$\frac{1}{\rho}\frac{\partial\langle P\rangle_{x_3,t}}{\partial x_2} \approx -\left\langle u_2\frac{\partial u_2}{\partial x_2}\right\rangle_{x_3,t} \tag{2.11}$$

This estimate (Eq. 2.11) comes from a balance of the wall-normal momentum equation and is consistent with the wall-normal budget shown in Fig. 2.1b. Then, Term 2 is approximated by

$$\frac{1}{\rho}\frac{q'}{q}\xi_2\frac{\partial\langle P\rangle_{\xi_3,t}}{\partial\xi_2} = \frac{1}{\rho}\frac{q'}{q}x_2\frac{\partial\langle P\rangle_{x_3,t}}{\partial x_2} \approx -\frac{q'}{q}\left\langle x_2u_2\frac{\partial u_2}{\partial x_2}\right\rangle_{x_3,t} = -\frac{q'}{q}\left\langle \xi_2u_2\frac{\partial u_2}{\partial\xi_2}\right\rangle_{\xi_3,t} \tag{2.12}$$

The magnitude of Term 2 can be compared to the magnitude of the nominally dominant source term in the streamwise momentum equation, namely $q'/q\xi_2\langle u_1\partial u_1/\partial\xi_2\rangle_{\xi_3,t}$. This comparison is similar to comparing the magnitudes of $\partial\langle u_1^2\rangle_{\xi_3,t}/\partial\xi_2$ and $\partial\langle u_2^2\rangle_{\xi_3,t}/\partial\xi_2$. The ratio of these two terms is at most 10^{-3} throughout the boundary layer for $Re_{\theta_0} = 4000$, is independent from the length of the domain, and is expected to decrease with increasing Reynolds number.

The time and spanwise averaged H_ν is given by

$$\langle H_\nu(u_i)\rangle_{\xi_3,t} = \underbrace{\nu\left[1-\left(\frac{q_0}{q}\right)^2+\left(\xi_2\frac{q'}{q}\right)^2\right]\frac{\partial^2\langle u_i\rangle_{\xi_3,t}}{\partial\xi_2^2}}_{\text{Term 3}} + \underbrace{\nu\left[2\left(\frac{q'}{q}\right)^2-\frac{q''}{q}\right]\xi_2\frac{\partial\langle u_i\rangle_{\xi_3,t}}{\partial\xi_2}}_{\text{Term 4}} \tag{2.13}$$

Term 3 is just the mean wall-normal viscous term in the respective momentum equations scaled by $\left[1-(q_0/q)^2+(\xi_2q'/q)^2\right]$. Given that the mean velocity profiles all sharply decay past $\xi_2 > \delta_{99,0}$, it is appropriate to restrict our analysis to

$\xi_2 < \delta_{99,0} \approx 7\theta_0$. Then, the ratio of Term 3 to the mean wall-normal viscous term is approximated by

$$1 - \left(\frac{q_0}{q}\right)^2 + \left(\delta_{99,0}\frac{q'}{q}\right)^2 \approx 2\xi_1\left(\frac{q_0'}{q_0}\right) + \left(7\theta_0\frac{q_0'}{q_0}\right)^2 \tag{2.14}$$

where a Taylor expansion has been applied. If one uses that $q \sim \theta$, then $q_0' \approx 1/2C_f$. For $Re_{\theta_0} = 4000$, the ratio of Term 3 to the mean wall-normal viscous term is less than 10% for a streamwise extent of $60\theta_0$. Again, with increasing Reynolds number (decreasing C_f), this streamwise extent is only expected to increase.

Term 4 has no immediate analogue in any of the momentum equations, but it bears resemblance to the dominant source term of each equation. For simplicity, we will focus on the streamwise momentum equation. In this case, the ratio between Term 4 and the dominant source term is given by

$$\frac{\nu\left[2\frac{q'}{q} - \frac{q''}{q'}\right]\langle\frac{\partial u_1}{\partial \xi_2}\rangle_{\xi_3,t}}{\langle u_1\frac{\partial u_1}{\partial \xi_2}\rangle_{\xi_3,t}} \approx \frac{Re_{\theta_0}^{-1}\left[C_f + \frac{1}{\sqrt{2}\kappa}C_f^{3/2}\right]}{\langle u_1/u_{1,\infty}\frac{\partial u_1}{\partial x_2}\rangle_{\xi_3,t}/\langle\frac{\partial u_1}{\partial x_2}\rangle_{\xi_3,t}} \tag{2.15}$$

where we have used that, provided $q \sim \theta$, as $qq''/q' \approx \partial C_f/\partial Re_\theta Re_\theta$ for constant $u_{1,\infty}$ and ν, and given the Coles-Fernholz relation, this is approximately $-\sqrt{2}/\kappa C_f^{3/2}$, where κ is the Kármán constant. Equation 2.15 is not easily computed. However, if one considers the maximum magnitude of the numerator and the maximum magnitude of the denominator over the boundary layer, the ratio is consistently less than 10^{-4} for streamwise extents in excess of $x_1 = x_0 \pm 30\theta_0$.

Based solely on the mean values of each of the additional source terms, it has been shown that for streamwise extents of $60\theta_0 \approx 40\delta^* \approx 7\delta_{99}$, the terms H_p, H_ν, and H_c all remain at approximately one order of magnitude smaller than the other terms in the governing equations.

2.1.4 Simplified equations and closure

We can now make the following two critical assumptions:

1. The governing equations evaluated at $q(x_1) = q_0$ are valid for a narrow streamwise domain centered at $x_1 = x_0$.

2. There exists a function $q(x_1)$ such that ensemble-averaged quantities are both statistically stationary and statistically homogeneous in the ξ_1, ξ_3 directions.

Given both assumptions and with the neglecting of H_ν and H_p, the governing equations simplify to

$$\frac{\partial u_j}{\partial \xi_j} = \xi_2 \frac{q_0'}{q_0} \frac{\partial u_1}{\partial \xi_2} \tag{2.16}$$

$$\frac{\partial u_i}{\partial t} = -u_j \frac{\partial u_i}{\partial \xi_j} - \frac{1}{\rho} \frac{\partial P}{\partial \xi_i} + \nu \frac{\partial^2 u_i}{\partial \xi_j^2} + \xi_2 \frac{q_0'}{q_0} u_1 \frac{\partial u_i}{\partial \xi_2} \tag{2.17}$$

These are the final governing equations to be solved via streamwise periodic simulation. Section 2.2 presents an *a posteriori* analysis justifying both the neglecting of H_ν and H_p and the streamwise statistical homogeneity of Eq. 2.16-2.17.

The use of both assumptions and the neglecting of H_ν and H_p mean that the governing equations can be more accurately described as homogenized Navier-Stokes equations (HNSE). Consequently, simulations utilizing this set of equations are still DNS but do not directly solve the NSE. The rest of the chapter seeks to compare the solutions of the HNSE to experimental and numerical solutions to the NSE.

We now seek to generate a closure equation for q_0'/q_0 by considering the ξ_2 integrated continuity and streamwise momentum equations in conservative form.

$$\begin{aligned} &\int_0^\infty \left(\frac{\partial u_1}{\partial \xi_1} + \frac{\partial u_3}{\partial \xi_3} \right) d\xi_2 + u_{2,\infty} \\ &\qquad = \frac{q_0'}{q_0} \int_0^\infty \left(\xi_2 \frac{\partial u_1}{\partial \xi_1} \right) d\xi_2 \end{aligned} \tag{2.18}$$

$$\begin{aligned} &\int_0^\infty \left(\frac{\partial \rho u_1}{\partial t} + \frac{\partial \rho u_1 u_j}{\partial \xi_j} + \frac{\partial P}{\partial \xi_1} \right) d\xi_2 \\ &= \frac{q_0'}{q_0} \int_0^\infty \left(\xi_2 \frac{\partial \rho u_1 u_1}{\partial \xi_1} \right) d\xi_2 + \int_0^\infty \mu \frac{\partial^2 u_1}{\partial \xi_k^2} d\xi_2 \end{aligned} \tag{2.19}$$

We now ensemble average Eq. 2.18-2.19 and denote ensemble averaged quantities by $\langle\cdot\rangle$. Applying Assumption 2 yields the following equations.

$$u_{2,\infty} = \frac{q_0'}{q_0}\int_0^\infty \left(u_{1,\infty} - \langle u_1\rangle\right) d\xi_2 = \frac{q_0'}{q_0} u_{1,\infty}\delta^* \tag{2.20}$$

$$u_{1,\infty}u_{2,\infty} + \frac{\tau_w}{\rho} = \frac{q_0'}{q_0}\int_0^\infty \left({u_{1,\infty}}^2 - \langle u_1 u_1\rangle\right) d\xi_2 \tag{2.21}$$

where $\tau_w = \mu\langle\partial u_1/\partial\xi_2\rangle|_{\xi_2=0}$ is the wall shear stress. Some further manipulation gives our final closure equation.

$$\frac{q_0'}{q_0} = \frac{\tau_w/\rho}{\int_0^\infty \left(u_{1,\infty}\langle u_1\rangle - \langle u_1 u_1\rangle\right) d\xi_2} \tag{2.22}$$

This expression fully closes the simplified governing equations (Eq. 2.16-2.17) and is used in the streamwise periodic numerical simulations of Section 2.3.

Before discussing the results, it is interesting to estimate *a priori* the right hand side of the above equation. The von Kármán momentum integral equation for a flat-plate boundary layer estimates the growth rate of the momentum thickness by

$$\theta' = \frac{\tau_w}{\rho u_{1,\infty}^2} \tag{2.23}$$

By definition,

$$u_{1,\infty}^2\theta = \int_0^\infty \left(u_{1,\infty}\langle u_1\rangle - \langle u_1\rangle\langle u_1\rangle\right) d\xi_2 \tag{2.24}$$

The streamwise fluctuations $\langle u_1' u_1'\rangle$ are known to scale with u_τ^2, whereas the streamwise mean velocity profile scales with $u_{1,\infty}^2$ in the outer layer, which encompasses the majority of the boundary layer. Thus, for the majority of the boundary layer $\langle u_1\rangle^2 \gg \langle u_1' u_1'\rangle$ and so, within the wall-normal integral, $\langle u_1\rangle^2 \approx \langle u_1^2\rangle$. With this approximation, the von Kármán momentum integral equation becomes

$$\frac{\theta'}{\theta} \approx \frac{\tau_w/\rho}{\int_0^\infty \left(u_{1,\infty}\langle u_1\rangle - \langle u_1 u_1\rangle\right) d\xi_2} = \frac{q_0'}{q_0} \tag{2.25}$$

Table 2.1: DNS parameters for the streamwise non-periodic turbulent boundary layer simulation cases.

Dataset	L_x	Governing Eq.	Closure Eq.	Time δ_{99}/u_τ
BL_Cart	$15\delta_{99}$	Eq. 2.1-2.2	None	15
BL_Full	$15\delta_{99}$	Eq. 2.4-2.8	Empirical Value	30
BL_Simp	$15\delta_{99}$	Eq. 2.16-2.17	Empirical Value	30
BL_Plus	$15\delta_{99}$	Eq. 2.4-2.8	$1.1 \times$ Empirical Value	15
BL_Minus	$15\delta_{99}$	Eq. 2.16-2.17	$0.9 \times$ Empirical Value	15
BL_Per	$7.5\delta_{99}$	Eq. 2.16-2.17	Eq. 2.22	30

This completes the intuition that $q(x)$ scales like $\theta(x)$ and furthermore provides an estimate for q_0'/q_0.

$$\frac{q_0'}{q_0} \approx \frac{\theta'}{\theta} = \frac{1}{2\delta^*} C_f H_{12} \tag{2.26}$$

where $C_f = \tau_w / \left(\frac{1}{2}\rho u_{1,\infty}^2\right)$ is the skin-friction coefficient and $H_{12} = \delta^*/\theta$ is the shape factor.

Note that the closure equation ensures a statistically stationary flow and consequently the solution will be specific to a single Reynolds number. This is in direct contrast with recycling and rescaling methods which solve for a range of Reynolds numbers but also use flow at high Reynolds number stations as a substitute for a low Reynolds number inflow. The net effect of the closure equation (Eq. 2.22) is to allow the current method to avoid unphysical inflows by focusing on a single Reynolds number.

2.2 Spatially developing simulations

We conduct six sets of boundary layer simulations, each solving a different set of governing equations and boundary conditions, summarized in table 2.1. The results are used to justify assumptions (1) and (2), and the simplifications made to the governing equations in Section 2.1.2.

2.2.1 Simulations and numerical methods

With the exception of BL_Per, all of the cases have streamwise non-periodic boundaries in an inflow/outflow set-up. Case BL_Per corresponds to the most "modified" case: it solves Eq. 2.16-2.17 with Eq. 2.22 and implements streamwise periodic boundary conditions. Case BL_Simp also solves Eq. 2.16-2.17 but does not use streamwise periodic boundary conditions. Case BL_Full solves Eq. 2.4-2.8 and

contains all of the previously neglected terms. Cases BL_Full and BL_Simp use empirical relations for low Reynolds number [11] for the closure of q_0'/q_0 by approximating $q \approx \theta$. Cases BL_Plus and BL_Minus differ from BL_Simp by using a closure for q_0 artificially increased and decreased by 10%, respectively. Finally, case BL_Cart solves the regular Cartesian Navier-Stokes equations (Eq. 2.1-2.2).

All of the cases have periodic spanwise directions and non-periodic wall-normal directions. The bottom of the domain is treated with a no-slip boundary condition, and the top of the computational domain is treated with a Neumann boundary condition. Each of the five inflow/outflow cases use planes from case BL_Per as an inflow (at $\xi_1 = 0$). All of the streamwise non-periodic cases use convective outflow conditions at the streamwise outlet and have mass conservation conducted at the streamwise outlet. In contrast, case BL_Per has mass conservation conducted at the wall-normal outlet. The top of the computational domain requires vertical transpiration for all six cases. BL_Cart imposes a transpiration velocity given by Ref. [10], similar to Ref. [14]. For the remaining cases, Eq. 2.18 shows that any closure for q_0'/q_0 directly provides a value for $u_{2,\infty}$.

All of the cases have the same spanwise length of $L_z = 2.6\delta_{99}$ and wall-normal height of $L_y = 3.4\delta_{99}$. They all have the same spatial resolution: $\Delta x^+ = 9, \Delta y^+_{\text{min}} = 0.3, \Delta z^+ = 6$. The key difference between the streamwise periodic and streamwise non-periodic cases is the streamwise domain length. BL_Per has a domain length of $L_x = 7.5\delta_{99}$, whereas the rest of the cases have a domain length of $L_x = 15\delta_{99}$. It is known from [40] that the flow recovers from this particular inflow technique after $\sim$ 4-5δ_{99}. Accounting for potential outflow effects of at most $\sim 2\delta_{99}$, this leaves about $8\delta_{99}$ of uncontaminated statistics.

Each set of governing equations is solved using the computational solver NGA [41]. The numerical code solves the conservative-variable formulation of the low-Mach Navier-Stokes equations with staggered finite difference operators and uses a fractional step method to enforce continuity. The code is run fully second order in space and time.

2.2.2 Results

Figures 2.3ab present the normalized displacement thickness and momentum thickness averaged in ξ_3 and in time for the streamwise non-periodic cases. Each of the streamwise non-periodic simulation cases is affected by the convective outflow condition, seen in case BL_Cart. Each of the displacement thickness and mo-

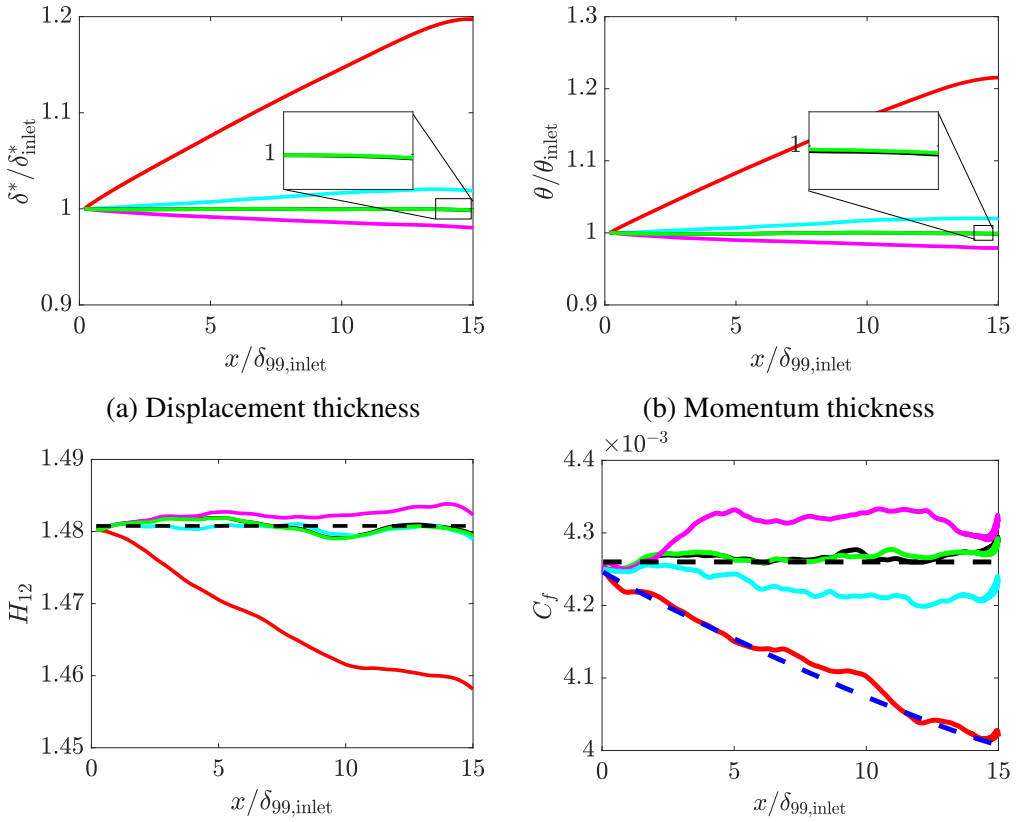

(a) Displacement thickness

(b) Momentum thickness

(c) Shape factor

(d) Skin friction coefficient

Figure 2.3: streamwise variation of (a) displacement thickness (δ^*), (b) momentum thickness (θ), (c) shape factor (H_{12}) and (d) skin friction coefficient (C_f). Lines: (solid black) BL_Full; (solid green) BL_Simp; (solid cyan) BL_Minus; (solid magenta) BL_Plus; (solid red) BL_Cart; (dashed black) BL_Per; (dashed black) scaled empirical fit [11] to match inlet skin friction coefficient

mentum thickness plots deviate in slope at about $1\delta_{99}$ from the streamwise outlet. Because BL_Cart represents a spatially developing boundary layer, the displacement thickness increases from its original inflow value. The present increase by about 20% is expected given that $d\delta^*/dx = u_{2,\infty}/u_{1,\infty}$ and the imposed value of $u_{2,\infty}/u_{1,\infty} \approx 3\times10^{-3}$. Cases BL_Full and BL_Simp are indistinguishable and show relatively constant values of δ^* and θ with fluctuation magnitudes of $\pm 0.3\%$ of the inflow nominal value. The thicknesses of BL_Plus and BL_Minus show immediate departures from the nominal value, by approximately 2% of the original inflow value.

Refs. [42] and [43] underscore the need for consistency when comparing DNS profiles of boundary layers. For the sake of comparison, integral and global quantities are computed as described by Ref. [42]. Specifically, the shape factor, H_{12} is

evaluated as

$$H_{12} = \frac{\int_0^{\delta_{99}} (1 - \overline{u}_1/u_{1,\infty}) d\xi_2}{\int_0^{\delta_{99}} (\overline{u}_1/u_{1,\infty})(1 - \overline{u}_1/u_{1,\infty}) d\xi_2} \tag{2.27}$$

where, for the remainder of this section, the $\bar{\cdot}$ represents temporal and spanwise averaging. Similarly, the wall shear stress is evaluated by $\tau_w = \mu \partial \overline{u}_1 / \partial \xi_2|_{\xi_2=0}$. Figure 2.3c presents the shape factor for the non-streamwise periodic cases. BL_Cart has a shape factor that monotonically drops by 2% from its inflow value, as expected from empirical fits by [10] with respect to Reynolds number. BL_Plus and BL_Minus also exhibit a slowly varying shape factor, changing by approximately ±0.3% from the inflow value. This is in contrast with BL_Full and BL_Simp, whose shape factors are virtually identical and do not exhibit major mean variations.

Figure 2.3d presents the skin friction coefficient, averaged in ξ_3 and in time for the non-streamwise periodic cases. Case BL_Cart features a decreasing skin friction coefficient over the domain, consistent with increasing Reynolds number. The skin friction coefficients of BL_Plus, BL_Minus, BL_Full, and BL_Simp have fluctuations of about 1% of their expected mean value. Any variations of the value with streamwise distance are masked by these fluctuations. Again, BL_Simp and BL_Full are virtually indistinguishable.

Figure 2.4 shows temporal and spanwise averaged profiles of $\overline{u}_1$, $u_{1,\text{rms}}$, $u_{2,\text{rms}}$ and $-\overline{u_1' u_2'}$ from Case BL_Simp and BL_Full. These profiles are extracted from three streamwise locations: near the inlet ($\xi_1 = 0$) and outlet ($\xi_1 = 13\delta_{99}$) for Case BL_Simp, and in the middle of the domain ($\xi_1 = 7.5\delta_{99}$) for both cases BL_Simp & BL_Full. The mean streamwise velocity profiles are within ±0.5% of each other. The streamwise and wall-normal rms collapse within ±1% of each other. The Reynolds stress profiles show a strong collapse in both the inner and outer regions.

Overall, these streamwise non-periodic simulations show that under a rescaling by $q(x)$, the resulting flow does not feature observable streamwise inhomogeneities over a sizeable streamwise domain. The neglecting of H_ν and H_p terms and the use of streamwise periodic conditions under Eq. 2.16-2.17 are consequently justified.

2.3 Numerical set-up of streamwise periodic simulations

The present section outlines the simulations conducted in streamwise periodic domains. It clarifies domain constraints and initial conditions, and describes additional

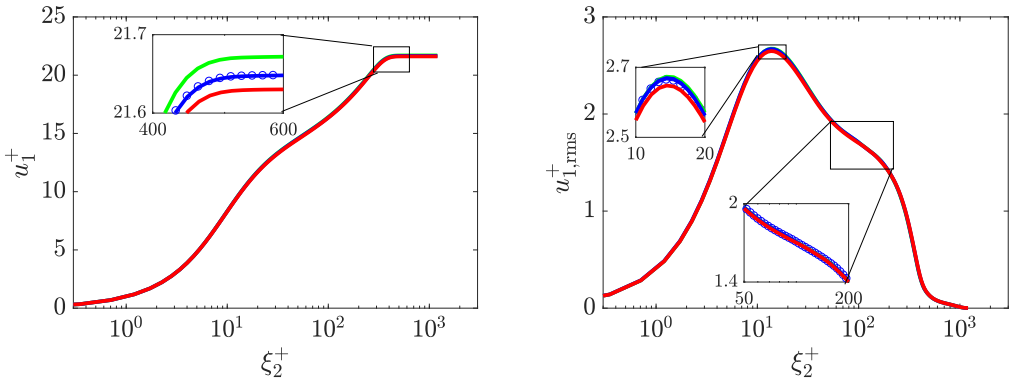

(a) streamwise velocity

(b) streamwise rms

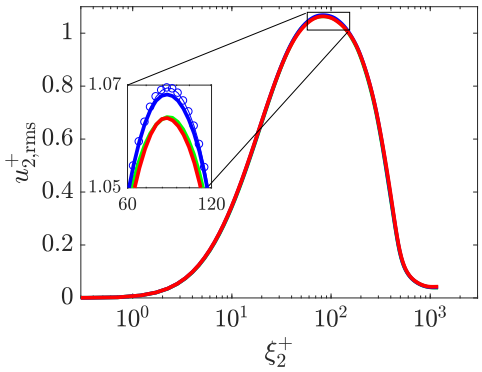

(c) Wall-normal rms

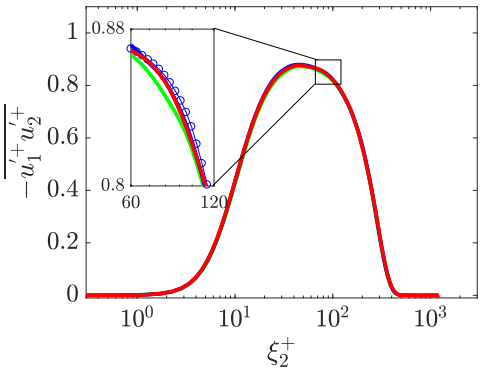

(d) Reynolds shear stress

Figure 2.4: Inner scaled (a) mean streamwise velocity $\overline{u_1^+}$, (b) streamwise rms ($u_{1,\mathrm{rms}}^+$), (c) wall-normal rms ($u_{2,\mathrm{rms}}^+$), and (d) Reynolds shear stress $-\overline{u_1'^+ u_2'^+}$, averaged over time and spanwise direction (ξ_3) for Case BL_Simp at different streamwise locations and BL_Full at the middle of the domain. Symbols : (green) BL_Simp at $\xi_1 = 0$ (inlet), (black) BL_Simp at $\xi_1 = 7.5\delta_{99}$, (red) BL_Simp at $\xi_1 = 13\delta_{99}$, ∘ BL_Full at $\xi_1 = 7.5\delta_{99}$.

numerical techniques used during simulation.

2.3.1 Simulation cases

We now solve Eq. 2.16-2.17 with streamwise periodic boundary conditions for four different Reynolds numbers, summarized in table 2.2. Case BL1460 is equivalent to BL_Per. Cases BL2830, BL3550 and BL5650 were chosen for direct comparison against the DNS and experiments of [39].

The domain size, (L_x, L_y, L_z), is determined primarily by the sizes of the largest turbulent structures. The pressure fluctuations are known to reach the furthest out of the boundary layer to about $2.4\delta_{99}$ [16], setting the minimum requirement for

Table 2.2: DNS parameters for the turbulent boundary layer simulation cases.

Dataset	Re_{δ^*}	Initial Condition	Nx × Ny × Nz	Sample Time δ_{99}/u_τ
BL1460	1460	Blasius + white noise	$300 \times 120 \times 160$	30
BL2830	2830	Fully turbulent field from BL1460	$530 \times 160 \times 280$	15
BL2830Wn	2830	Blasius + white noise	$530 \times 160 \times 280$	15
BL2830Eig	2830	Blasius + white noise and streamwise mode	$530 \times 160 \times 280$	15
BL2830H	2830	Fully turbulent field from BL5650	$530 \times 160 \times 280$	15
BL2830Sill	2830	Fully turbulent field from [14]	$530 \times 160 \times 280$	15
BL3550	3550	Fully turbulent field from BL2830	$648 \times 230 \times 338$	15
BL5650	5650	Fully turbulent field from BL2830	$968 \times 326 \times 512$	15

wall-normal height. We set our domain height to $18\delta^* \sim 3\delta_{99}$ to fully capture these fluctuations. Since low-momentum streaks are approximately $0.5\delta_{99}$ in width [18, 44], we opt for a spanwise width of $14\delta^* \sim 2.5\delta_{99}$ which is comparable to the domain size of Ref. [39]. The large-scale motions (LSMs) corresponding to bulges or hairpin packets have a maximum streamwise length of $3\delta_{99}$ [45–49]. In contrast, the very-large-scale-motions (VLSMs) have lengths of up to $10\delta_{99}$ in the streamwise direction [47–49]. Lee & Sung (Ref. [18]) have found that these structures have a mean streamwise length of less than $6\delta_{99}$, and that statistically over 95% of the turbulent structures in their DNS had streamwise lengths of $< 6\delta_{99}$. And so, we opt for a domain of $40\delta^* \sim 7\delta_{99}$ in streamwise length.

The resolution is chosen so that the smallest turbulent structures can be adequately resolved. The streamwise and spanwise grids are uniform with $\Delta x^+ = 9, \Delta z^+ = 6$ which is comparable to the resolution parameters of Sillero *et.al* [14] ($\Delta x^+ \approx 7$, $\Delta z^+ \approx 4.7$) and Orlu *et.al* [39] ($\Delta x^+ \approx 8.5$, $\Delta z^+ \approx 4$). The wall-normal domain uses a hyperbolic stretching with 8 points in the viscous sub-layer, ($\xi_2 < 5\delta_\nu$), with $\Delta y^+_{\text{min}} \approx 0.3$. This is comparable to the wall-normal resolution of Sillero *et.al* [14] who also had 8 points in the viscous sub-layer at the inlet and that of Orlu *et.al* [39] who had 10 points in the viscous sub-layer at their lowest Reynolds number. To improve accuracy, we opt to use 4th order finite difference spatial operators. Appendix A.1 compares the effect of both higher and lower finite difference spatial operators on case BL1460.

Cases BL2830, BL3550, and BL5650 are sampled over a period of 15 δ_{99}/u_τ whereas Case BL1460 is sampled over a period of 30 δ_{99}/u_τ. BL1460 was run for longer specifically to gather temporal statistics of the global quantities, e.g. skin friction coefficient and shape factor.

BL1460 uses a laminar boundary layer superimposed with white noise of fixed amplitude $0.1u_{1,\infty}$ as an initial condition. Cases BL2830, BL3550 and BL5650 use fully turbulent fields from lower Reynolds number simulations as initial conditions. For example, BL5650 uses fields from BL2830, and BL2830 uses fields from BL1460. It will be shown in Section 2.3.1 that the statistically stationary solution is independent of the initial conditions used. The use of already turbulent fields as an initial condition greatly reduces the duration of the numerical transient when compared to using a laminar boundary layer as an initial condition. For completeness, laminar flows initialized with turbulent fields are shown in Appendix A.2.

To investigate the transient period, a set of turbulent cases were run at $Re_{\delta^*} = 2830$

with varying initial conditions. This specific Reynolds number was chosen to investigate the impact of using both higher and lower Reynolds number fields as initial conditions. The complete list of different cases are also shown in Table 2.2. Each case has the same domain size and resolution as BL2830. BL2830Wn utilizes only white noise with an amplitude of $0.1u_{1,\infty}$. Lower amplitudes of white noise are found to be insufficient to directly trigger turbulence and cause the flow to re-laminarize, similar to what can occur in LWS recycling [50, 51]. BL2830Eig uses the same initial field as BL2830Wn but with a single superimposed streamwise mode as well as its corresponding wall-normal eigenfunction which are both based on stability analysis from Ref. [52]. Taking further inspiration from Ref. [37], cases BL2830 and BL2830H use fully turbulent fields from cases BL1460 and BL5650, respectively, after interpolating them to the appropriate resolution. Finally, case BL2830Sill uses an instantaneous data file from Ref. [14] at $Re_{\delta^*} = 5650$. A streamwise section of $\sim 7\delta_{99}$ is taken and then interpolated to match the appropriate resolution.

2.3.2 Implementation of q_0'/q_0

In practice, the ensemble averages used in Eq. 2.22 to calculate q_0'/q_0 are approximated by spanwise and streamwise averages. From this value, the given metric terms are calculated, and the continuity and momentum equations (Eq. 2.16-2.17) are further solved at each time step. In this way, the simulation is fully independent of any a priori information and undercuts Ref. [37]'s original need for upstream stations. However, over the course of a simulation, computational errors may accumulate and cause δ^* to eventually drift. This could ultimately result in a substantial temporal drift in all integrated quantities and profiles. To prevent this, we implement a single relaxation term in the streamwise momentum equation to relax δ^* to a targeted value δ^*_{d}.

$$\frac{\partial u_1}{\partial t} = -u_j\frac{\partial u_1}{\partial \xi_j} - \frac{1}{\rho}\frac{\partial P}{\partial \xi_1} + \nu\frac{\partial^2 u_1}{\partial \xi_j^2} + \xi_2\frac{q_0'}{q_0}u_1\frac{\partial u_1}{\partial \xi_2} + \frac{\alpha}{u_{1,\infty}}\frac{(\delta^* - \delta^*_{\mathrm{d}})}{\delta^*}\xi_2 u_1\frac{\partial u_1}{\partial \xi_2} \tag{2.28}$$

where the time-scale $\alpha = u_\tau/\delta_{99}$ is chosen so as to not introduce an additional time-scale in the flow. It should be noted that this relaxation term is the only method of prescribing a specific δ^* to the simulation. Volumetric integration of Eq. 2.28

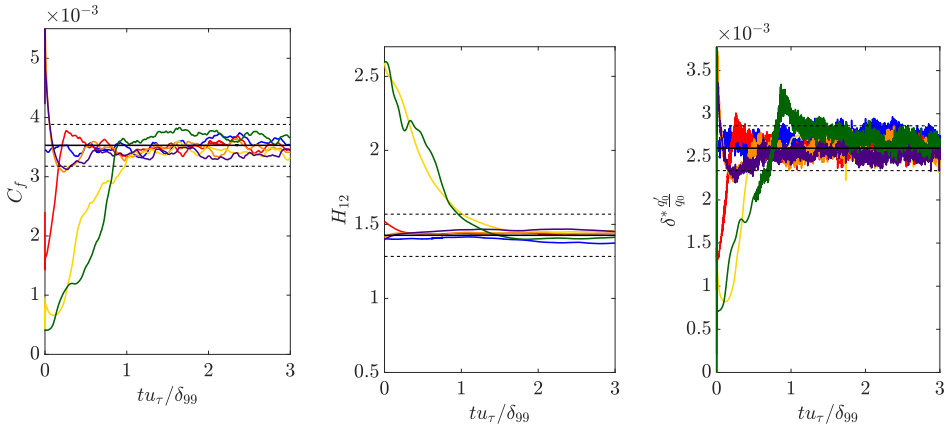

(a) Skin friction coefficient (b) Shape factor (c) Closure term

Figure 2.5: Temporal evolution of (a) skin friction coefficient C_f, (b) shape factor H_{12}, and (c) normalized closure term $\delta^* \frac{q_0'}{q_0}$, for the turbulent cases shown in table 2.2. Lines: (black) BL2830 in the statistical steady-state, (gold) BL2830Wn, (green) BL2830Eig, (red) BL2830, – (orange) BL2830H, (purple) BL2830Sill, (solid black) empirical values, (dashed black) ±10% of empirical values for C_f and H_{12}

directly shows that the relaxation term describes to first-order an exponential decay of the instantaneous δ^* towards the desired value.

Results from the simulation cases described in table 2.2 are given in this section. In particular, integrated quantities such as shape factor H_{12}, skin friction coefficient C_f, and the various moments of u_1 are presented in comparison to values found in the literature.

2.4 Results and verifications

2.4.1 Transient behavior

A major benefit of periodic boundary conditions is the independence of the statistical steady-state solution from the initial conditions. Here, we present transient behavior for turbulent boundary layers from a variety of initial conditions.

The shape factor is still calculated by Eq. 2.27 and the wall shear-stress is still calculated by $\tau_w = \mu \overline{\partial u_1/\partial \xi_2}|_{\xi_2=0}$. However, for the current and following sections, $\bar{\cdot}$ will denote averaging in time and in both spanwise and streamwise directions. Figure 2.5 shows the transient behavior of each turbulent case listed in table 2.2. After a "wash-out" time, the flow reaches a statistical stationary state. Regardless of the initial condition, the integral quantities converge to the same statistical steady-state values. Moreover, cases BL2830Wn and BL2830Eig show a much slower

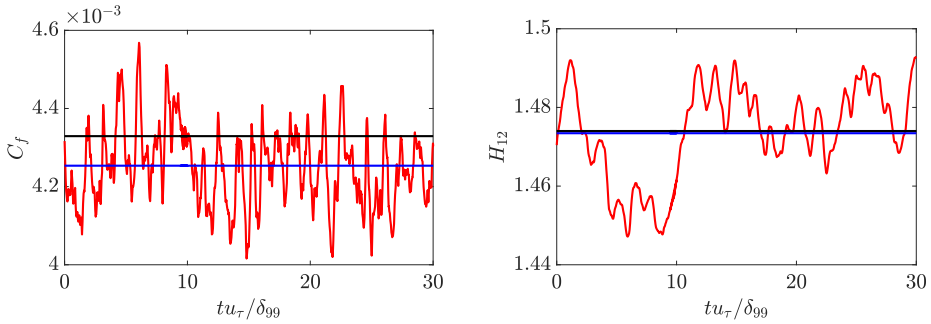

(a) Skin friction coefficient (b) Shape factor

Figure 2.6: Temporal Evolution of (a) C_f and (b) H_{12} for case BL1460. Colors: (red) instantaneous values, (black) mean value, and (black) empirical value.

convergence than the other cases by at least a factor of 4. This provides justification for using lower Reynolds number turbulent fields as initial conditions for higher Reynolds number simulations, similar to extended TDNS methods [33]. Case BL2830Sill demonstrates that even streamwise non-periodic initial data can still be used as an initial condition to achieve the same results.

The transient period lasts at most $2\delta_{99}/u_\tau$ and can be as short as $0.5\delta_{99}/u_\tau$. As expected these transient periods are far shorter than with laminar initial fields. It has been argued by Nagib *et al.* (2007) [53] that the appropriate turbulent boundary layer time-scale is δ_{99}/u_τ. Transient periods on the same order of magnitude are to be expected. To further quantify the temporal evolution, Figure 2.5c shows $\delta^* q_0'/q_0$ over time for the cases presented in table 2.2. During the transient period, $\delta^* q_0'/q_0$ grows from its initial value to the nominal turbulent value.

Under statistically stationary conditions, the C_f has an rms of 2.2 % of its mean value and its fluctuations have an integral timescale of $\sim 0.3\delta_{99}/u_\tau$ as shown in Fig. 2.6a. In contrast, H_{12} has an rms of 0.8% of its mean value with a much larger integral timescale of $\sim 1.9\delta_{99}/u_\tau$, as shown in Fig. 2.6b. Both of the integral timescales for skin friction and shape factor were calculated by first computing the two-time autocorrelation function during the statistically steady regime and then integrating the function only up to the autocorrelation function's first zero-crossing. $\delta^* q_0'/q_0$ has fluctuations similar to C_f rather than H_{12} and these can already be seen in Fig. 2.5c. These temporal oscillations are due to the approximation of ensemble averages by planar averages in the evaluation of Eq. 2.22.

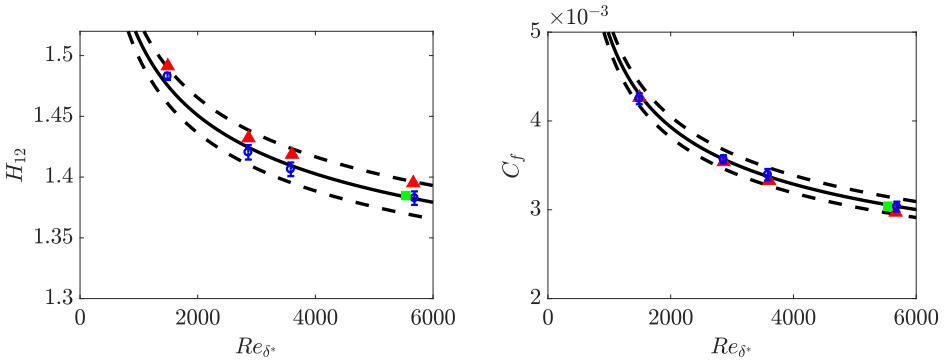

(a) Shape factor (b) Skin friction coefficient

Figure 2.7: (a) Shape factor H_{12} as a function of Reynolds number Re_{δ^*}. Solid line represents empirical fit by [10], and dashed lines indicate ±1%. (b) Skin friction as a function of Re_{δ^*}. Solid line represents the extended Coles-Fernholz relation with $\kappa = 0.384, C = 3.3, D_0 = 182, D_1 = -2466$ [11]. Dashed lines indicate ±3%. Symbols: △(red) DNS [39]; □ (green) DNS [14]; ○ (black) current study.

2.4.2 Integral and global quantities

Monkewitz *et al.* [10] generated empirical fits of experiments for H_{12} against Reynolds number and these will be used as a guide for appropriate values. Similarly, we use Chauhan's extended Coles-Fernholz skin friction relation

$$\sqrt{\frac{2}{C_f}} = \frac{1}{\kappa}\ln(Re_{\delta^*}) + C + D_0\frac{\ln Re_{\delta^*}}{Re_{\delta^*}} + \frac{D_1}{Re_{\delta^*}} \tag{2.29}$$

with $\kappa = 0.384$, $C = 3.3$, $D_0 = 182$, and $D_1 = -2466$ [11]. While there are a broad variety of composite profiles, the previous empirical profiles use up-to-date experimental data and account for low Re effects.

The final values of H_{12} obtained for the simulation cases are shown in Fig. 2.7a alongside the empirical fit in the numerical results with 1% error margins. Error bars were evaluated consistent with the method used in Ref. [54]. Noticeably the calculated values are within ± 0.7% of the empirical values. Following suit, the skin friction coefficient, C_f, is compared against the extended Coles-Fernholz skin friction relation [11]. The results are shown in Fig. 2.7b with corresponding error bars, and the given simulations are within at most ±2.5% of the empirical values. It is interesting to note that the present results are closer to the composite fit of the experimental data than the DNS results of Ref. [39].

2.4.3 Mean velocity profiles

Figure 2.8 displays the inner-scaled mean streamwise velocity profiles of the different Reynolds number simulation results plotted against those of [39]. Since the shape factors of growing and homogeneous boundary layers are within 1% of each other, it is no surprise that the streamwise mean velocity profiles show similar agreement. The maximum numerical uncertainty in u_1^+ and $u_{1,rms}^+$ for all cases was 0.003 and 0.01, respectively, estimated using the methodology of [55].

We also compute the log-intercept function $\Psi^+ \equiv u_1^+ - \kappa^{-1}\ln(\xi_2^+)$ and the log-indicator function $\Xi \equiv \xi_2^+ du_1^+/d\xi_2^+$. These two functions are often used to calculate the two constants required by the log-law. A nominal value of $\kappa = 0.384$ was used. Figure 2.8c shows that at lower Reynolds numbers, the log-layer is not yet formed. This is indicative of inadequate scale-separation. As the Reynolds number increases, however, a log-layer appears to form around $\xi_2^+ = 40-100$ for $Re_{\delta^*} = 5650$. The log-intercept function is similarly constant in the log-layer and also appears to plateau for $\xi_2^+ = 40-100$. Experimental data [39] are also plotted for both the log-intercept and log-indicator functions and show good agreement with the current simulations. In particular, near the wake region ($\xi_2^+ \gtrsim 800$), the profiles given for $Re_{\delta^*} = 3550$ agree better with experimental results than the corresponding profiles from the DNS of Ref. [39]. Ref. [39] noted that due to low resolution near the wall, the velocity profile of the experimental data for $\xi_2^+ < 15$ is under-resolved. This is represented by a large scatter in experimental data for the log-indicator function.

The Reynolds stress and rms velocity profiles are shown with inner scaling in Fig. 2.9. All of the profiles exhibit a near-wall peak, and the peak locations coincide with those of the profiles from Ref. [39]. There is a minor deviation in $u_{1,\mathrm{rms}}^+$ in the log-layer and wake region at around $\xi_2^+ \approx 100-200$ of at most 5%. The experimental results for $Re_{\delta^*} = 3550$ and 5650 [39] are also plotted and show good agreement with the current study in the region of deviation. Interestingly, in the region $\xi_2^+ = 100-200$, the experimental data for $Re_{\delta^*} = 3550$ stand at equal distance between our DNS results and the previous DNS results of Ref. [39]. The $u_{2,\mathrm{rms}}^+$ profile features slightly higher values near the free-stream. These fluctuations can be somewhat reduced by extending the domain in the wall-normal direction. However, in the present formulation, the $u_{2,\mathrm{rms}}$ will never reach zero. Indeed, from integration of continuity (Eq. 2.16), $u_{2,\infty} = (q_0'/q_0)u_{1,\infty}\delta^*$. Since the closure for q_0'/q_0 is not an *a priori* fixed quantity, q_0'/q_0 varies in time, and hence the transpiration velocity also fluctuates in time. As mentioned previously, due to the low near-wall resolution of Ref. [39],

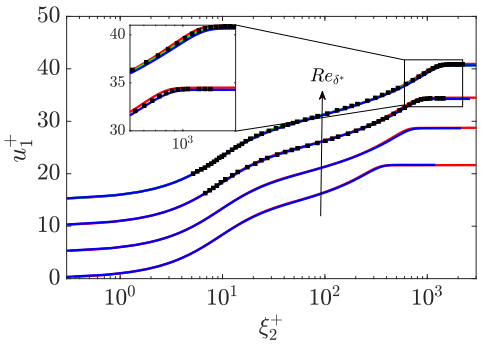

(a) streamwise velocity

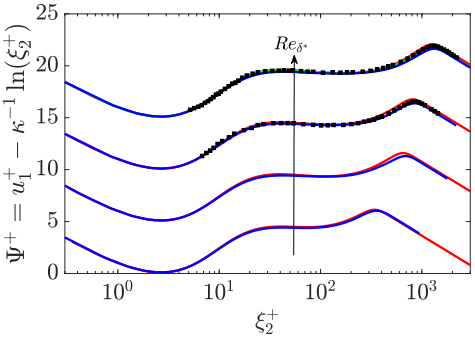

(b) Log-intercept function

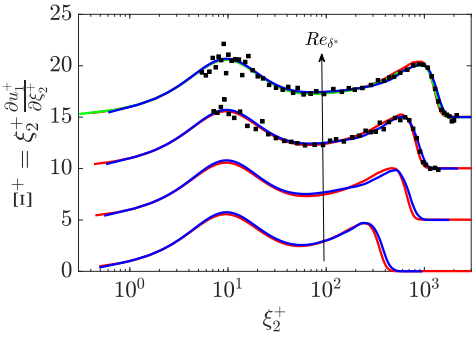

(c) Log-indicator function

Figure 2.8: Mean inner scaled (a) streamwise velocity (u_1^+), (b) log-intercept function $\Psi^+ \equiv u_1^+ - \kappa^{-1}\ln(\xi_2^+)$ with $\kappa = 0.384$, (c) log-indicator function $\Xi \equiv \xi_2^+ \frac{\partial u_1^+}{\partial \xi_2^+}$ vs. ξ_2^+ for different Reynolds numbers. From bottom to top, shifted by $5u_1^+$: $Re_\delta^* = 1460, 2830, 3550, 5650$. Legend: (red) [39] DNS data; (black) present work; (green) [14]; □ (black) [39] experimental data.

the inner layer peak for experimental data at $\xi_2^+ \sim 15$ is not fully captured. Finally, a small deviation may be observed in the spanwise and wall-normal rms velocity profiles in the near-wall region.

2.5 Computational cost

The most popular method of boundary layer simulation remains the spatially growing boundary layer. However, this computational method is more computationally expensive than the current framework for three main reasons: an overall longer streamwise domain, slower statistical convergence, and smaller time-step.

Spatially developing boundary layer simulations require large streamwise domains to reach the largest Reynolds numbers. Inflow generation methods, such as recycling and rescaling, heavily reduce the overall simulation cost by bypassing transition and increasing the initial Reynolds number. The recycling domain covers

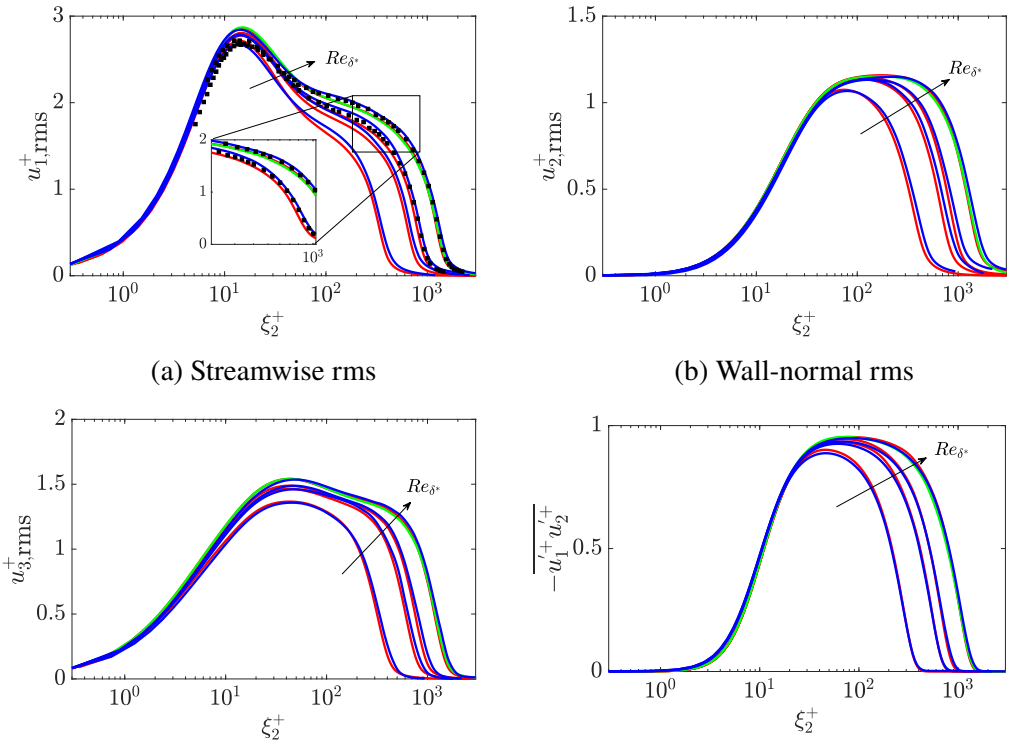

(a) Streamwise rms

(b) Wall-normal rms

(c) Spanwise rms

(d) Reynolds shear stress

Figure 2.9: (a) $u^+_{1,\mathrm{rms}}$ (b) $u^+_{2,\mathrm{rms}}$ (c) $u^+_{3,\mathrm{rms}}$ (d) $-\overline{u_1'^+ u_2'^+}$ vs. ξ_2^+ for different Reynolds numbers. From bottom to top: $Re^*_\delta = 1460, 2830, 3550, 5650$. Legend: (red) [39] DNS data; (black) current study; (green) [14]; □ (black) [39] experimental data.

a large portion of the streamwise domain and for Ref. [14], the recycling domain was $115\delta_{99,\text{recy. inlet}} \approx 44\delta_{99,\text{prod. inlet}}$. Moreover, all simulations that use inflow generation techniques must also undergo an "eddy-turnover recovery length" that increases with inlet Reynolds number [14]. Over this distance, none of the calculated statistics match empirical values within appropriate tolerance. For Ref. [14], this length-scale encompassed over a quarter of their production domain ($27\delta_{99,\text{prod. inlet}}$ out of a domain of $110\delta_{99,\text{prod. inlet}}$). In summary, a recycling and rescaling set-up like that of Ref. [14] would therefore require an upstream domain length of at least $71\delta_{99,\text{prod .inlet}}$ or 48 $\delta_{99,0}$, where $\delta_{99,0}$ is the boundary layer thickness at the location where statistics are extracted. Ref. [39] required $56\delta_{99,0}$ to reach the given Reynolds number as well. In contrast, our simulation at a Reynolds number of 5650 (BL5650) only required a streamwise domain of $7\delta_{99,0}$. Therefore, the proposed method reduces the streamwise domain by about an order of magnitude.

Statistical convergence is another limiting factor of boundary layer simulation. Due to the growth of the boundary layer, the streamwise distance for which the boundary

layer thickness remains within ±0.5% of a specific value is approximately $1\delta_{99}$. Thus streamwise developing boundary layer simulations are only able to average over streamwise slabs of approximately $1\delta_{99}$ in streamwise length. In contrast, the current method uses a streamwise domain of $7\delta_{99}$ in length and due to statistical homogeneity in the streamwise direction, the current method can average over a larger sample. In other words, the current method is expected to be seven times faster at converging statistics.

Finally, for a streamwise developing boundary layer DNS, the wall-normal resolution is determined by the inner layer thickness at the inlet (i.e. the lowest turbulent Reynolds number in the flow) so that all inner layer dynamics are fully resolved. Since the inner layer grows with streamwise distance, by the end of the production domain, the flow is over-resolved in the viscous sublayer. For example, the inner layer grew by 12% and by 20% for Refs. [14] and [39], respectively. In addition, the convective Courant-Friedrichs-Lewy (CFL) number in the wall-normal direction is usually the leading constraint on the time-step size for flat plate boundary layer DNS owing in large part to the wall-normal stretching of the mesh. Thus, Refs. [39] and [14] have time-steps that could potentially be 20% and 12% larger, respectively, if the high fidelity simulations could be run on grids with the ideal resolution. Because the proposed method uses a q'/q calculated specifically to keep δ^* constant, it will maintain the initial boundary layer thickness. Since viscosity is prescribed and the free-stream is far from the boundary layer, the method effectively specifies a single Reynolds number for the simulation. Therefore, an ideal resolution can be used and, consequently, a larger time-step can be applied. Overall, the expected savings from a more ideal wall-normal resolution and larger time-steps is at least 25%.

The net cost reduction from the proposed method is about two orders of magnitude and is theoretically independent of the streamwise and spanwise domain length of the proposed method. For example, although a domain $14\delta_{99}$ in length would use twice the number of streamwise grid-points, it would also have twice the sample range. Similar statements can be made for the spanwise direction as well.

Given a potential computational cost reduction of one to two orders of magnitude (by a factor of ~ 60), one might wonder: if one had the computational resources of Orlu *et al.* (2013), whose largest Reynolds number was $Re_{\delta^*} = 5650$ ($Re_\tau \approx 1300$), then what would be the largest Reynolds number achieved using the rescaling methodology? The computational domain of Orlu *et al.* (2013) had dimensions of $L_x \approx 55\delta_{99}$, $L_y \approx 3\delta_{99}$, $L_z \approx 2.5\delta_{99}$, based on δ_{99} measured at the streamwise

location where $Re_{\delta^*} = 5650$. The domain also had resolution requirements of $\Delta x^+ \approx 7$, $\Delta y^+_{\mathrm{m}in} \approx 0.3$ and $\Delta z^+ \approx 4$, and was sampled for a total of $40\delta_{99}/u_\tau$ over streamwise slabs of $1\delta_{99}$ for a total computational cost of 9 million cpu-hours.

The computational savings allow for a reduction in streamwise domain size to $7\delta_{99}$, a reduction in sample time by a factor of 7, and optimization of time-step and wall-normal grid resolution. However, the domain size requirements are in terms of δ_{99}, while the grid resolution requirements are in terms of δ_ν. Similarly, the sample time requirement is in terms of δ_{99}, and the time-step is constrained by flow near the wall, and so it will be in highly dependent on δ_ν. The overall computational cost therefore roughly scales like Re_τ^4. In other words, the computational cost reduction of 60 corresponds to an increase in Re_τ of approximately 2.8. Therefore, if one had the computational resources of Orlu*et al.* (2013), one could reach a total $Re_{\delta^*} \approx 17500$ ($Re_\tau \approx 3600$). For reference, the lower limit for the existence of an inertial subrange in the velocity spectra for pipe flows was estimated by McKeon & Morrison (2007) to be at $Re_\tau^{pipe} \gtrsim 5000$. Assuming the same limit for boundary layer flow, one would only require ~ 33 million cpu-hours.

2.6 Conclusion

A new method for simulating flat-plate turbulent boundary layers has been presented. The proposed method solves the Navier-Stokes equations in rescaled coordinates and was derived based on the assumption that self-similarity holds locally for a turbulent boundary layer. The method improves upon Spalart's original work by removing the dependence on lower Reynolds number simulations.

To derive the method, we rescaled the wall-normal coordinate by a single length-scale, $q(x_1)$, and found by an *a priori* analysis that the additional terms resulting from rescaling counterbalances the Reynolds stresses in the wake region, thus keeping the boundary layer statistically stationary. To complete the derivation, we made two critical assumptions: (1) the modified Navier-stokes equations hold over a narrow streamwise domain and (2) after rescaling, the flow is statistically stationary and statistically homogeneous in streamwise and spanwise directions. The key requirement for the use of this methodology is that $q'/q\delta_{99} \ll 1$. The method was then applied to a variety of Reynolds number cases, and the integral quantities and profiles were presented. The shape factor and skin friction coefficients were within $\pm 1\%$ and $\pm 3\%$ of aggregated experimental fits, respectively. Near $\xi_2^+ = 100$, the $u^+_{1,\mathrm{rms}}$ compares favorably with the experimental values and deviates with respect

to the DNS of [14] and [39] by about 5%. The mean wall-normal velocity profile was also compared to that of Refs. [14] and [39]. Overall, the method was computationally less expensive than competing simulations by one to two orders of magnitude.

Chapter 3

ERROR ESTIMATION OF ONE-POINT STATISTICS OF A HOMOGENIZED STREAMWISE PERIODIC BOUNDARY LAYER

Although much of the current literature on boundary layer simulation has been focused on the inflow conditions [13, 14, 16, 18, 39, 42], the majority of the streamwise growing boundary layer simulations [14, 16, 18, 39, 42] impose a $u_{2,\infty}(x_1)$ profile at the top of the domain. The streamwise periodic framework of Chapter 2 imposed no such transpiration velocity, and yet the resultant global quantities of interest were as good as if not better than those of streamwise growing simulations. These surprisingly good results form the basis for the present study. Since no transpiration velocity was imposed, the resultant transpiration velocity within the periodic simulation can be used to as a quantification of error. Given how deeply tied the transpiration velocity is to boundary layer dynamics [58], it is necessary to 1) investigate and quantify the error in transpiration velocity and 2) modify the current method from Chapter 2 to capture the transpiration velocity.

First, we theorize how errors in the transpiration velocity might develop. Then, we investigate the multiscale nature of the boundary layer, from an *a priori* and *a posteriori* perspective. Finally,we provide an interrogation of the continuity equation via an error budget.

3.1 Wall-normal velocity profile

The governing equations in Eq. 2.16-2.22 rely only on a single scaling. Because q broadly rescales the entire boundary layer and since the majority of the boundary layer is covered by the outer layer, it can be assumed that q is an outer-scale. This was confirmed in Chapter 2 and q'/q was found to be approximated by θ'/θ. However, in the near-wall region ($x_2^+ < 10$), the relevant near-wall length-scale is $\delta_\nu = \nu/\sqrt{\tau_w/\rho}$. One might expect the relevant source term to be proportional to δ_ν'/δ_ν rather than q'/q. One can show that this may lead to a discrepancy in the transpiration velocity profiles of growing and periodic boundary layers.

Consider the ensemble averaged continuity equation and its wall-normal integrated form

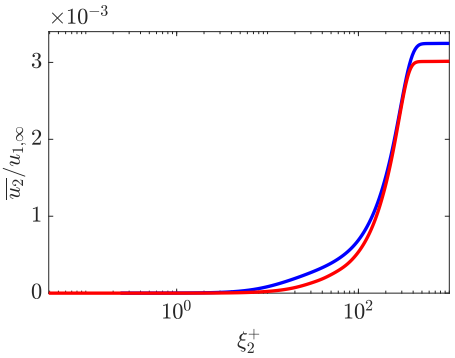

Figure 3.1: Profiles of normalized wall-normal velocity $\overline{u}_2/u_{1,\infty}$ and for $\mathrm{Re}_{\delta^*} = 1460$. Colors: (red) streamwise developing DNS [60], (black) Periodic DNS [59].

$$\frac{\partial \overline{u}_2}{\partial \xi_2} = \xi_2 \frac{q'}{q} \frac{\partial \overline{u}_1}{\partial \xi_2} \tag{3.1}$$

$$\overline{u}_2(\xi_2) = \int_0^{\xi_2} \frac{q'}{q} \xi_2^* \frac{\partial \overline{u}_1}{\partial \xi_2^*} d\xi_2^* \tag{3.2}$$

where $\bar{\cdot}$ defines ensemble-averaged quantities. Figure 3.1 compares the wall-normal velocity profiles between a streamwise growing [39] and periodic [59] boundary layer at $\mathrm{Re}_{\delta^*} = 1460$. The periodic profile overshoots the non-periodic profile in the inner layer and as a direct consequence, overshoots the final free-stream value by about 5%. This result is consistent with the fact that the inner layer grows much more slowly than the outer layer and so the broadband use of q'/q as a rescaling parameter throughout the boundary layer provides small inaccuracies in the transpiration velocity. A wall-normal varying value of q'/q may be necessary to capture appropriately the evolution of $u_{2,\infty}$. Obtaining a wall-normal varying metric source term of q'/q would require rescaling the wall-normal coordinate by $q^{ms}(x_1, x_2)$ instead of $q(x_1)$.

3.2 *A priori* multiscale analysis

The current section analyzes the multiscale nature of the boundary layer and investigates the impact of multiscale terms on the mean velocity profile.

3.2.1 *A priori* analytical multiscale behavior

The discussion in the previous section suggested that a rescaling by $q^{ms} = q^{ms}(x_1, x_2)$ might be necessary to better capture streamwise growth effects on the mean flow. For example, after applying a wall-normal rescaling by q^{ms} to $\partial \langle u_1 \rangle_{x_3,t}/\partial x_1$, one would expect the following relation:

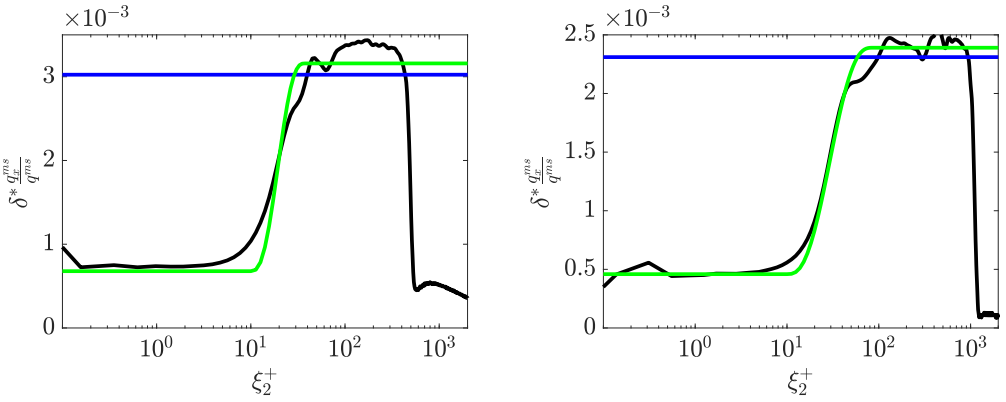

(a) $\mathrm{Re}_{\delta^*} = 1460$ (b) $\mathrm{Re}_{\delta^*} = 3550$

Figure 3.2: Normalized profiles of q_x^{ms}/q^{ms} extracted from Ref. [39] for $\mathrm{Re}_{\delta^*} = 1460$ (a), 3550 (b). Lines: (black) $\delta^* q'/q$ (Eq. 2.22); (black) Extracted $\delta^* q_x^{ms}/q^{ms}$ (Eq. 3.3); (red) Blending $\delta^* q_x^{ms}/q^{ms}$ (Eq. 3.18, 3.20).

$$\frac{\partial \langle u_1 \rangle_{x_3,t}}{\partial x_1} = -\xi_2 \frac{q_x^{ms}}{q^{ms}} \frac{\partial \langle u_1 \rangle_{\xi_3,t}}{\partial \xi_2} \approx -x_2 \frac{q_x^{ms}}{q^{ms}} \frac{\partial \langle u_1 \rangle_{x_3,t}}{\partial x_2} \tag{3.3}$$

Boundary layer data from spatially growing DNS [39] can be used to evaluate the LHS and RHS of Eq. 3.3 to extract a profile for q_x^{ms}/q^{ms}. Figure 3.2 compares the resulting extracted profiles against extracted values of q'/q using Eq. 2.22 for two different Re_{δ^*}. q_x^{ms}/q^{ms} varies throughout the buffer and mesolayer, up to $\xi_2^+ \approx 100$. In both the near wall region ($\xi_2^+ < 10$), and in the outer layer ($\xi_2/\delta_{99} \gtrsim 0.1$), q_x^{ms}/q^{ms} is approximately constant.

The near-wall plateau can be understood by invoking the law of the wall ($u_1^+ \approx \xi_2^+$ for $\xi_2^+ < 10$). The right hand side of Eq. 3.3 becomes

$$\frac{q_x^{ms}}{q^{ms}} \xi_2 \frac{\partial \langle u_1 \rangle_{\xi_3,t}}{\partial \xi_2} = \frac{q_x^{ms}}{q^{ms}} \xi_2^+ \frac{\partial \left(u_1^+ u_\tau \right)}{\partial \xi_2^+} \approx \frac{q_x^{ms}}{q^{ms}} u_\tau \xi_2^+ = \xi_2 \frac{q_x^{ms}}{q^{ms}} \frac{\tau_w}{\mu} \tag{3.4}$$

where inner-scale notation has been used: $u^+ = \langle u_1 \rangle_{\xi_3,t}/u_\tau$, $\xi_2^+ = \xi_2/\delta_\nu$, $u_\tau = \nu/\delta_\nu$. A Taylor expansion of the LHS of Eq. 3.3 around $\xi_2 = 0$ yields

$$-\frac{\partial \langle u_1 \rangle_{\xi_3,t}}{\partial x_1} \approx -\xi_2 \frac{\partial}{\partial x_1} \left(\frac{\partial \langle u_1 \rangle_{\xi_3,t}}{\partial \xi_2} |_{\xi_2=0} \right) = -\xi_2 \frac{\tau_w'}{\mu} \tag{3.5}$$

Finally, Eq. 3.3 simplifies to

$$\frac{q_x^{ms}}{q^{ms}}|_{inner} \approx -\frac{\tau_w'}{\tau_w} = -\frac{C_f'}{C_f} = 2\frac{\delta_\nu'}{\delta_\nu} \tag{3.6}$$

The outer plateau can be understood by using the law of the wake ($u^+ = u^+_{1,\infty} + f_o(\xi_2/\Delta)$, for some universal profile f_o, and the Clauser thickness $\Delta = \delta^* u^+_{1,\infty}$). The LHS of Eq. 3.3 gives

$$-\frac{\partial \langle u_1 \rangle_{\xi_3,t}}{\partial x_1} = -u_\tau' f_o + \frac{\Delta'}{\Delta}\frac{\xi_2}{\Delta} u_\tau f_o' \approx \frac{\Delta'}{\Delta}\frac{\xi_2}{\Delta} u_\tau f_o' \tag{3.7}$$

where $|u_\tau'/u_\tau| \ll |\Delta'/\Delta|$ has been used to simplify the equation. The RHS of Eq. 3.3 also gives

$$\xi_2 \frac{q_x^{ms}}{q^{ms}} \frac{\partial \langle u_1 \rangle_{\xi_3,t}}{\partial \xi_2} = \frac{q_x^{ms}}{q^{ms}} \frac{\xi_2}{\Delta} u_\tau f_o' \tag{3.8}$$

Finally, Eq. 3.3 simplifies to

$$\frac{q_x^{ms}}{q^{ms}}|_{outer} \approx \frac{\Delta'}{\Delta} \tag{3.9}$$

3.2.2 Budget analysis of multiscale behavior

The following analysis focuses on the effects of employing the wall-normal rescaling by $q^{ms}(x_1, x_2)$ on the u-momentum equation in contrast to the effects of employing a constant wall-normal rescaling by $q(x_1)$.

The full transformed equations are given by

$$\frac{\partial u_j}{\partial \xi_j} = \xi_2 \frac{q_x^{ms}}{q} \frac{\partial u_1}{\partial \xi_2} + H_c^{ms} \tag{3.10}$$

$$\frac{\partial u_i}{\partial t} = -u_j \frac{\partial u_i}{\partial \xi_j} - \frac{1}{\rho}\frac{\partial P}{\partial \xi_i} + \nu \frac{\partial^2 u_i}{\partial \xi_j^2} + \xi_2 \frac{q_x^{ms}}{q^{ms}} u_1 \frac{\partial u_i}{\partial \xi_2} + H_p^{ms}(u_i) + H_\nu^{ms}(u_i) \tag{3.11}$$

where

$$H_c^{ms} = \left(1 - \frac{q_0^{ms}}{q^{ms}} - x_2 \frac{\partial}{\partial x_2}\left[\frac{q_0^{ms}}{q^{ms}}\right]\right) \frac{\partial u_2}{\partial \xi_2} \tag{3.12}$$

$$H_p^{ms}(u_i) = \frac{1}{\rho}\delta_{1i}\xi_2\frac{q_x^{ms}}{q^{ms}}\frac{\partial P}{\partial \xi_2} + \left(1 - \frac{q_0^{ms}}{q^{ms}} - x_2\frac{\partial}{\partial x_2}\left[\frac{q_0^{ms}}{q^{ms}}\right]\right)\left(u_2\frac{\partial u_i}{\partial \xi_2} + \delta_{i2}\frac{1}{\rho}\frac{\partial P}{\partial x_i}\right) \tag{3.13}$$

$$\begin{aligned} H_\nu^{ms}(u_i) = \nu\Bigg[1 - \left(\frac{q_0^{ms}}{q^{ms}} + x_2\frac{\partial}{\partial x_2}\left[\frac{q_0^{ms}}{q^{ms}}\right]\right)^2 + \left(\xi_2\frac{q_x^{ms}}{q_0^{ms}}\right)^2\Bigg]\frac{\partial^2 u_i}{\partial \xi_2^2} \\ +\nu\left(\frac{\partial}{\partial x_2}\left[\frac{q_0^{ms}}{q^{ms}}\right] + x_2\frac{\partial^2}{\partial x_2^2}\left[\frac{q_0^{ms}}{q^{ms}}\right]\right)\frac{\partial u_i}{\partial \xi_2} \\ +\nu\left[2\left(\frac{q_x^{ms}}{q_0^{ms}}\right)^2 - \frac{q_{xx}^{ms}}{q_0^{ms}}\right]\xi_2\frac{\partial u_i}{\partial \xi_2} - 2\nu\xi_2\frac{q_x^{ms}}{q_0^{ms}}\frac{\partial^2 u_i}{\partial \xi_1 \partial \xi_2} \end{aligned} \tag{3.14}$$

Note that $q_0^{ms} = q^{ms}(x_0, x_2)$, and q^{ms} is assumed to be C^3. Thus, the evaluation of x_1 at x_0 can be commuted with differentiation by x_2. Post evaluation at $x_1 = x_0$, the terms H_c^{ms}, H_p^{ms}, and H_ν^{ms} are of the exact same form of H_c, H_p, and H_ν, respectively, with q_0'/q_0 replaced by q_x^{ms}/q_0^{ms}. In Section 3.2.1, it was shown that in the outer layer, q_x^{ms}/q_0^{ms} is of the same order as q_0'/q_0 or less. Consequently, H_c^{ms}, H_p^{ms} and H_ν^{ms} are of the same order as H_c, H_p, and H_ν. The following governing equations are obtained after applying the two assumptions of statistical homogeneity and a narrow streamwise domain, and after applying the same order-of-magnitude simplifications (see Chapter 2, Section 1).

$$\frac{\partial u_i}{\partial \xi_i} = \xi_2\frac{q_x^{ms}}{q^{ms}}\frac{\partial u_1}{\partial \xi_2} \tag{3.15}$$

$$\frac{\partial u_i}{\partial t} = -u_j\frac{\partial u_i}{\partial \xi_j} - \frac{1}{\rho}\frac{\partial P}{\partial \xi_i} + \nu\frac{\partial^2 u_i}{\partial \xi_j^2} + \xi_2\frac{q_x^{ms}}{q^{ms}}u_1\frac{\partial u_i}{\partial \xi_2} \tag{3.16}$$

An *a priori* analysis of the streamwise momentum equation is now conducted. To do so, spanwise and temporal averages are applied to Eq. 3.16 to obtain

$$\underbrace{\left\langle u_j\frac{\partial u_i}{\partial \xi_j}\right\rangle_{\xi_3,t}}_{\text{convective terms}} = \underbrace{\nu\frac{\partial^2\langle u_i\rangle_{\xi_3,t}}{\partial \xi_j^2}}_{\text{viscous terms}} + \underbrace{\xi_2\left\langle\frac{q_x^{ms}}{q^{ms}}u_1\frac{\partial u_i}{\partial \xi_2}\right\rangle_{\xi_3,t}}_{\text{source term}} \tag{3.17}$$

A wall-normal budget of the streamwise momentum equation is computed using DNS data [39] at $\mathrm{Re}_{\delta^*} = 5600$ and the results are shown in Fig. 3.3. On the

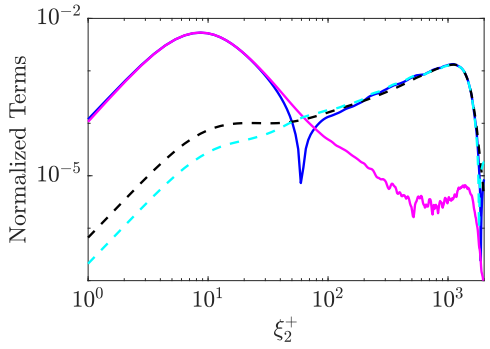

Figure 3.3: streamwise momentum magnitude budget from DNS data (Ref. [39]) at $\mathrm{Re}_{\delta^*} = 5600$. Lines: (solid black) Convective terms; (solid magenta) Viscous terms; (dashed black) $|\langle \frac{q'}{q} \xi_2 u_1 \frac{\partial u_1}{\partial \xi_2} \rangle_{\xi_3,t}|$; (dashed cyan) $|\langle \frac{q_x^{ms}}{q^{ms}} \xi_2 u_1 \frac{\partial u_1}{\partial \xi_2} \rangle_{\xi_3,t}|$.

same budget, the original source term $\langle \xi_2 (q'/q) u_1 \partial_{\xi_2}(u_1) \rangle_{\xi_3,t}$ is shown for direct comparison against the new source term from Eq. 3.17.

The original and new metric source terms balance the Reynolds shear stress in outer layer. As expected, they differ by a factor of ~ 4 in the inner layer. However, they both remain orders of magnitudes smaller than the convective and viscous terms. This observation is consistent with Klewicki *et al.* (2007) , who noted that in the near wall region, the viscous and shear stress terms balance nearly completely.

In the near-wall region, the contribution of the multiscale source term will always remain many orders of magnitude smaller than all other terms, regardless of Reynolds number. It can be shown that the viscous term scales like u_τ^2/δ_ν in the inner layer. The multiscale metric term scales like $u_\tau^2 q_x^{ms}/q^{ms}$. Hence, the ratio of the multiscale metric term to the viscous term scales like $\delta_\nu q_x^{ms}/q^{ms} \sim \delta'_\nu$, which is monotonically decreasing with Reynolds number. Similarly, the single-scale metric term scales like $u_\tau^2 q'/q$ and its ratio to the viscous term scales like $\delta_\nu q'/q \approx \delta_\nu \theta'/\theta \sim C_f/Re_\tau$. This ratio is also monotonically decreasing with Reynolds number. In both cases, neither metric source term is significant in the near wall region with respect to the viscous term.

In summary, from an *a priori* point of view, implementing a multiscale rescaling function q_x^{ms}/q^{ms} should not provide significant benefits on the mean profile of streamwise velocity. However, an *a posteriori* perspective is still needed to clarify impacts on other turbulent quantities.

3.3 *A posteriori* analysis of multiscale simulations

In this section, simulations are performed using the a model for q_x^{ms}/q^{ms}. The key purpose of this section is to conduct an *a posteriori* analysis of multiscale effects.

3.3.1 Fitted blending function

Conducting *a posteriori* analyses requires imposing a functional form for q_x^{ms}/q^{ms} similar to methods used in [36]. Section 3.2.1 has shown that near the wall $q_x^{ms}/q^{ms} \approx 2\delta_\nu'/\delta_\nu$, and far from the wall, $q_x^{ms}/q^{ms} \approx \Delta'/\Delta$. To transition smoothly between the two regions, a one-parameter smoothed step function is employed.

$$\begin{aligned}\frac{q_x^{ms}}{q^{ms}} &= \frac{\Delta'}{\Delta} g(\xi_2) + 2\frac{\delta_\nu'}{\delta_\nu}\left[1 - g(\xi_2)\right] \\ &= \frac{\Delta'}{\Delta}\left[g(\xi_2) + \frac{2(1-g(\xi_2))}{\kappa u_{1,\infty}^+ + 1}\right]\end{aligned} \tag{3.18}$$

where the log-law has been used to relate δ_ν'/δ_ν to Δ'/Δ, and $g(\xi_2)$ is a smooth step function defined by

$$g(\xi_2) = \begin{cases} 0 & \xi_2^+ \leq 10 \\ 6r^5 - 15r^4 + 10r^3 & \xi_2 \in [10\delta_\nu, 0.1\delta_{99}] \\ 1 & \xi_2 \geq 0.1\delta_{99} \end{cases} \tag{3.19}$$

where $r = \ln(\xi_2^+/10)/\ln(0.1\delta_{99}/\delta_\nu)$. Here, it has been assumed that the near-wall region extends up to $10\delta_\nu$, and the wake region extends down to 1θ. Thus, Eq. 3.18 provides a closure equation for q_x^{ms}/q^{ms} in terms of Δ'/Δ.

To complete the closure for Δ'/Δ, the u-momentum and continuity equations were integrated in the wall-normal direction and then averaged in the statistically homogeneous directions (ξ_1, ξ_3) to provide the following closure equation

$$\frac{\tau_w}{\rho}\frac{\Delta}{\Delta'} = \int_0^\infty \left[g(\xi_2) + \frac{2(1-g(\xi_2))}{\kappa u_{1,\infty}^+ + 1}\right] \xi_2 \frac{\partial}{\partial \xi_2}\left(\langle u^2\rangle_{\xi_1,\xi_3,t} - \langle u\rangle_{\xi_1,\xi_3,t} u_{1,\infty}\right) d\xi_2 \tag{3.20}$$

Overall, Eq 3.18-3.20 provide a fitted function to the actual q_x^{ms}/q^{ms} extracted via Eq. 3.3. A comparison between the fitted and extracted profiles of q_x^{ms}/q^{ms} is shown in Fig. 3.2 for $\mathrm{Re}_{\delta^*} = 1460$ and 3550. The fit agrees well with the extracted function in both the outer layer plateau all the way down to $\xi_2^+ = 10$. There is a 10% relative

Table 3.1: DNS parameters for the turbulent boundary layer simulation cases. * indicates simulations taken from Chapter 2.

Dataset	Re_{δ^*}	Governing Equations	Nx × Ny × Nz	Sample Time δ_{99}/u_τ
BL1460*	1460	Eq. 2.16-2.22	300 x 120 x 160	30
BL3550*	3550	Eq. 2.16-2.22	648 x 230 x 338	15
BL1460MS	1460	Eq. 3.15-3.16,3.20	300 x 120 x 160	15
BL3550MS	3550	Eq. 3.15-3.16,3.20	648 x 230 x 338	15

error in the outer layer plateau value for the lower Reynolds number comparison, but only a 3% relative error for the higher Reynolds number comparison. The inner layer plateau is also within 5%. This difference is primarily due to the use of the log-law for low Reynolds number flows and these differences are expected to decrease with increased Reynolds number.

It should be noted that Eq. 3.20 will be solved in real time for simulation purposes. Thus, the governing equations are completely closed.

3.3.2 Simulation parameters and numerical methods

The following cases were simulated and are summarized in Table 3.1. Cases BL1460MS and BL3550MS solve Eq. 3.15-3.16 with closure Eq. 3.20. All new cases (BL1460MS and BL3550MS) were simulated with the same domain size, resolutions and boundary conditions of the periodic simulations in Chapter 2 (BL1460, BL3550, etc.)

3.3.3 Simulation results

Figure 3.4 compares calculated skin-friction coefficients and shape factors from simulations BL1460MS and BL3550MS against those from single-scale simulations values [59], growing simulations [39], and empirical fits [10, 11]. The multiscale simulations have shape factors that are within 0.1% of the single-scale values and are within 0.4% of the streamwise growing DNS values. The multiscale skin-friction coefficients are within 0.6% of the single-scale values and are within 2% of the streamwise growing DNS values. The multiscale simulation shape factor and skin-friction coefficient both remain well within 0.5% and 2.2% of the corresponding empirical values, respectively. More importantly, the differences between the single-scale and multiscale simulation results are significantly less than between either and the growing simulation results

Figure 3.5 shows the inner-scaled mean streamwise velocity profiles of the different

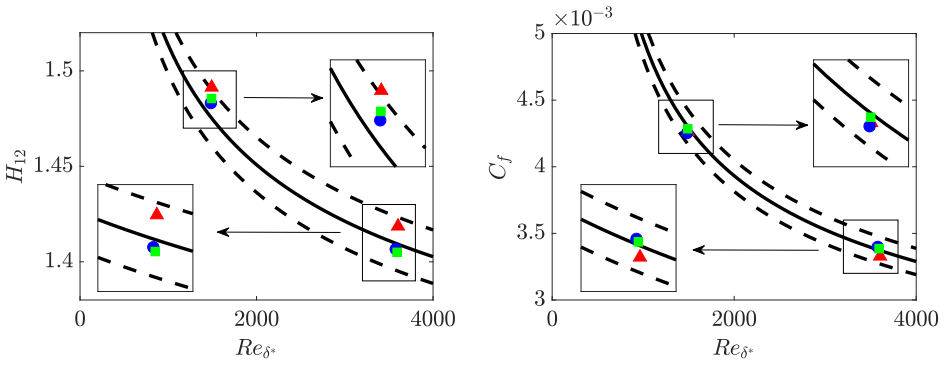

(a) Shape factor (b) skin-friction coefficient

Figure 3.4: (a) Shape factor H_{12} as a function of Reynolds number Re_{δ^*}. Solid line represents empirical fit by [10], and dashed lines indicate ±1%. (b) skin-friction as a function of Re_{δ^*}. Solid line represents the extended Coles-Fernholz relation with $\kappa = 0.384, C = 3.3, D_0 = 182, D_1 = -2466$ [11]. Dashed lines indicate ±3%. Symbols: △(red) DNS [39]; □ (green) Cases BL1460MS and BL3550MS (DNS) ; ○ (black) Cases BL1460 and BL3550 (DNS) [59].

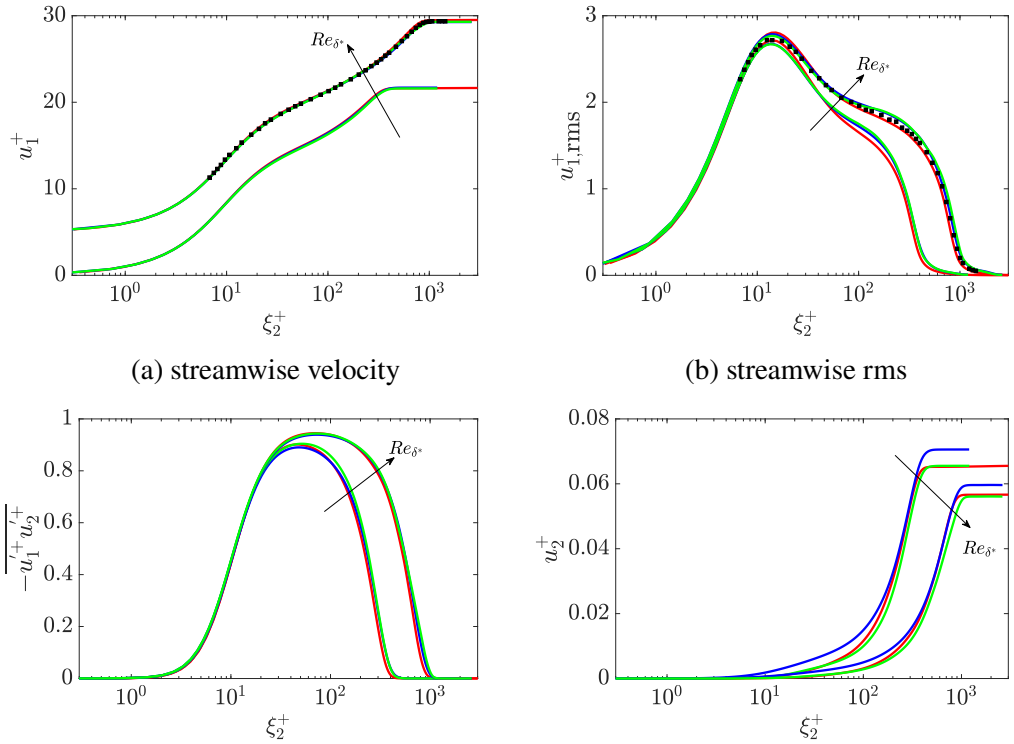

(a) streamwise velocity (b) streamwise rms

(c) Reynolds shear stress (d) Wall-normal velocity

Figure 3.5: (a) u_1^+ (b) $u_{1,\mathrm{rms}}^+$ (c) $-\overline{u_1'^+ u_2'^+}$ (d) u_2^+ vs. ξ_2^+ for $\mathrm{Re}_{\delta^*} = 1460, 3550$. Legend: (red) DNS [39]; (black) Single-scale cases BL1460, BL3550 [59]; (green) multiscale DNS cases BL1460MS and BL3550MS; □ (black) [39] experimental data.

Reynolds number simulation results in contrast with those of Ref. [39], which had a streamwise growing boundary layer, and the single-scale simulation results of Chapter 2. The shape factors and skin-friction coefficients being within 1 and 3%, respectively, of growing boundary layer simulation values directly implies the mean streamwise velocity profiles will be within 3% of growing boundary layer simulations for both $\mathrm{Re}_{\delta^*} = 1460$ and 3550. The normalized Reynolds stress and rms profiles are also plotted in Fig. 3.5. The agreement of the near wall-peak at $\xi_2^+ \approx 15$ with a relative difference 2% confirms that the multiscale rescaling effects are minimal on both the measured quantities of mean streamwise velocity and rms. These results are consistent with the *a priori* analyses conducted in Section 3.3.

Figure 3.5d shows the wall-normal velocity profiles. There is marked improvement in both the near-wall behavior and free-stream value. Specifically, $u_{2,\infty}^+$ varies by about 5% between the multiscale and single-scale cases, and the near wall behavior has a relative deviation of 3% between the multiscale and single-scale cases as well. The deviation between the single-scale simulation and multiscale simulation decreases with increasing Reynolds number.

3.4 Discussion of Reynolds number contribution

3.4.1 Reynolds number dependence

Classical descriptions of the boundary layer require two different scalings for the inner and outer layers [8]. To avoid the controversy of suggesting what velocity and length-scales are involved [7, 62], we will appeal to analysis via non-dimensional groups. For flat plate boundary layers, the ensemble-averaged mean streamwise velocity is given by

$$\frac{\overline{u}_1}{u_{1,\infty}} = f\left(\frac{x_2}{q}, \mathrm{Re}_q\right) \tag{3.21}$$

Consequently, the streamwise derivative is given by

$$\frac{\partial \overline{u}_1}{\partial x_1} = \underbrace{-x_2 \frac{q'}{q} \frac{\partial \overline{u}_1}{\partial x_2}}_{source\ term} + \underbrace{\frac{q'}{q} \mathrm{Re}_q \frac{\partial \overline{u}_1}{\partial \mathrm{Re}_q}}_{error\ term} \tag{3.22}$$

Note that the last term in Eq. 3.22 is omitted in Eq. 2.16 as a consequence of Assumption #1. Correspondingly, Eq. 2.16-2.22 lack any Reynolds number partial terms. Note that the neglecting of *explicit* Reynolds number partial derivative terms does not remove the Reynolds number dependence of the mean quantities, i.e., the

viscous terms still provide an *implicit* dependence on the Reynolds number. The evolution of the shape and skin-friction coefficient (see Fig. 3.4) are illustrative examples of this Reynolds number dependence. The good agreement in the global quantities implies that the exclusion of the Reynolds number partial terms has a negligible impact on the mean streamwise velocity for the current range of Reynolds numbers. However, it is unclear if this result persists for high Re_{δ^*}.

The current objective is to determine the magnitude of this "error" term over a large range of Reynolds numbers and compare its magnitude to that of the source term. First, we start by recognizing that the source term in the continuity equation and in Eq. 3.22 is nothing more than the log-indicator function $\Psi = x_2 \partial \overline{u}_1 / \partial x_2$ rescaled by q'/q. It can be computed easily from any DNS data. Figure 3.6a presents the re-scaled source term calculated from various DNS and experimental databases [14, 39, 59] for $Re_\theta = 4000$. All curves feature two peaks: one in the inner and one in the outer layer. Overall, there is good agreement between experimental and DNS profiles, with the experimental values featuring scatter near the wall due to resolution [39].

The "error" term can be extracted from streamwise growing boundary layers using Eq. 3.22. Unfortunately, experimental data for this particular quantity are not available. Similarly, the "error term" is also not accessible from single-scale periodic simulations. The resulting profiles are shown in Fig. 3.6b. Both profiles agree on a near-wall peak and its location, and show only small deviations on its magnitude. Further from the wall, the extracted profiles are close to zero and are noisy. From Eq. 3.22, the low magnitude of the "error" term in the outer layer indicates that the majority of the streamwise variation of $\overline{u}_1$ is captured by the source term. Since $q \approx \theta$ is an outer scale, and since the source term describes the growth of the boundary layer due to the growth of q, it is expected that the source term should capture most of the streamwise variation of the outer layer. In contrast, the large magnitude of the "error" term in the inner layer indicates that the majority of the streamwise variation of $\overline{u}_1$ in the inner layer is not captured by the source term. This is consistent with the results shown in Fig. 3.2. It was found that the metric term q'/q overshoots the actual value of $2\delta'_\nu/\delta_\nu$. Because the source term and "error" term have opposite signs in Eq. 3.22, it can be understood that in the inner layer, the source term overestimates the actual streamwise variation and the "error" term accounts for the overshoot. One could conclude that the effect of the "error" term is primarily concentrated in the inner layer.

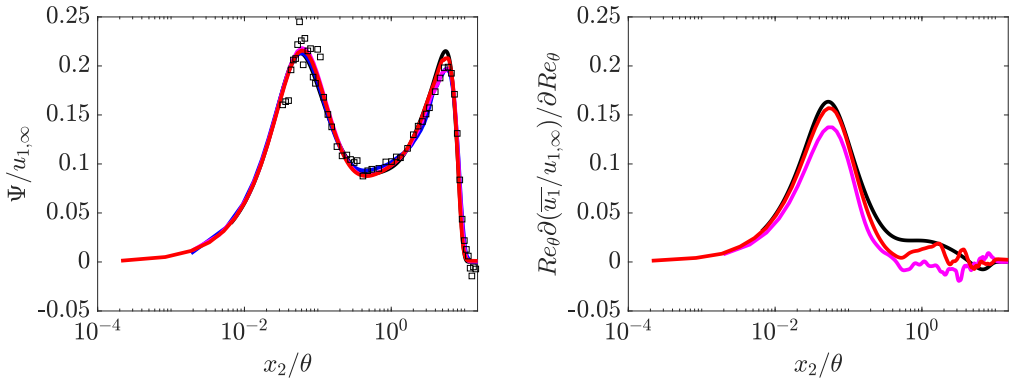

(a) Scaled source term (b) "Error" term

Figure 3.6: (a) Scaled source term $\Psi/U_\infty = x_2\partial(\overline{u}_1/u_{1,\infty})/\partial x_2$ (b) "error" term $\mathrm{Re}_\theta\partial(\overline{u}_1/u_{1,\infty})\partial\mathrm{Re}_\theta$ at $\mathrm{Re}_\theta \approx 4000$. Symbols indicate experiments. Colors: (black) Composite fit at $\mathrm{Re}_\theta \approx 4000$. [10]; (green) [14]; (black) [59]; (red) [39].

To extrapolate these results to higher Reynolds numbers, we turn to a composite fit [10]. The log indicator function is extracted from composite fit profiles and compared to the experimental and numerical profiles. The profiles are with in 1% in the inner layer. The composite fit overshoots the outer layer peak magnitude by ~10% , and this may be due to low-Reynolds number effects. Overall, the composite fit agrees with experimental and DNS results quite satisfactorily. Similarly, the composite fit is used to compute the "error" term and the resulting profile is shown in Fig. 3.6b. Once again, the profile agrees with the extracted DNS profiles on the location of the peak at $x_2/\theta \approx 0.1$. They only differ in the peak value by 16%.

The "error" term is plotted over a range of Reynolds numbers in Fig. 3.7b. The magnitude of the term decreases only slightly with increasing Reynolds number (a factor of 2 from $\mathrm{Re}_\theta = 10^3$ to $\mathrm{Re}_\theta = 10^8$) and the peak appears to be fixed within the inner layer. For comparison, the source term contribution is plotted in Fig. 3.7a for the same series of Reynolds numbers.

3.4.2 Global quantities

The previous Reynolds number dependence of the mean velocity profiles can be expressed by analyzing the differences between the solutions to the original Navier-Stokes equations and the solutions to Eq. 2.16-2.22. One can equivalently subtract the ensemble average of Eq. 2.16 from Eq. 3.22 and evaluate at $x_1 = x_0$ to obtain

$$x_2\frac{\partial\left(\overline{u}_1-\overline{u}_1^*\right)}{\partial x_2}-\frac{q}{q'}\frac{\partial\left(\overline{u}_2-\overline{u}_2^*\right)}{\partial x_2}=\frac{\partial\overline{u}_1}{\partial\mathrm{Re}_q}|_{x_0}\mathrm{Re}_q \tag{3.23}$$

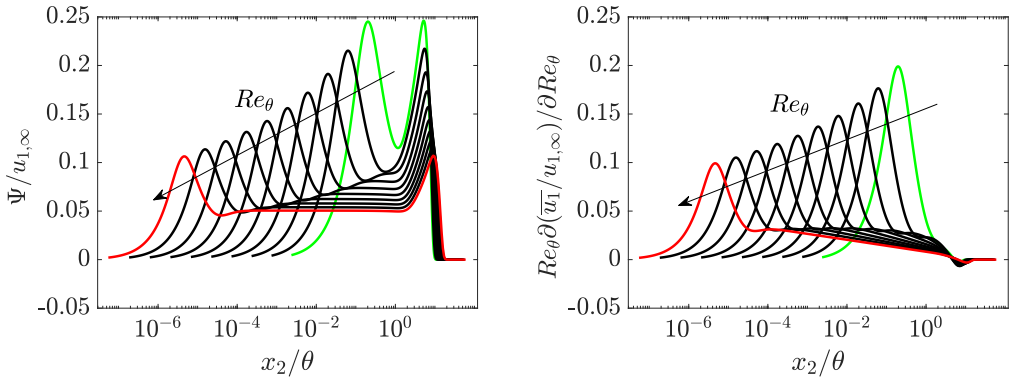

(a) Scaled source term

(b) "Error" term

Figure 3.7: (a) Scaled source term $\Psi/u_{1,\infty} = x_2\partial(\overline{u}_1/u_{1,\infty})/\partial x_2$ (b) "error" term $\mathrm{Re}_\theta\partial(\overline{u}_1/u_{1,\infty})\partial\mathrm{Re}_\theta$, predicted with the composite fit [10], for a range of $\mathrm{Re}_\theta = 10^3 - 10^8$.

where q'/q has been divided out and asterisks denote solutions to the transformed governing equations. Stated differently, the difference between the solutions to the Cartesian $(\overline{u}_1, \overline{u}_2)$ and transformed governing equations $(\overline{u}_1^*, \overline{u}_2^*)$ is given by the Reynolds number derivative of the mean velocity profile. Equation 3.23 can now be used to investigate the impact of this "error" term onto global quantities like the skin-friction coefficient and shape factor.

Integrating Eq. 3.23 in the wall-normal direction and dividing by θ gives

$$\underbrace{H_{12} - H_{12}^*}_{H_{12}\text{ Error}} - \frac{1}{q'u_{1,\infty}}(u_{2,\infty} - u_{2,\infty}^*) = \int_0^\infty \mathrm{Re}_\theta \frac{\partial \overline{u}_1/u_{1,\infty}}{\partial Re_\theta}|_{x_0} d\left(\frac{x_2}{\theta}\right) = \underbrace{-\mathrm{Re}_\theta \frac{\partial H_{12}}{\partial \mathrm{Re}_\theta}}_{\text{"Error" Term}} \tag{3.24}$$

To leading order of $\ln(\mathrm{Re}_\theta)$, the shape factor in the limit of large Reynolds number is approximated by $H_{12} - 1 \sim 7.11\kappa \ln(\mathrm{Re}_\theta)^{-1}$ [11]. The RHS of Eq. 3.24 can then be approximated as

$$-\mathrm{Re}_\theta \frac{\partial H_{12}}{\partial \mathrm{Re}_\theta} \sim 7.11\kappa \ln(\mathrm{Re}_\theta)^{-2} \tag{3.25}$$

For cases BL1460 and BL3550, this "error" term is nearly 6% of the shape factor value. Since the relative error in shape factors from the single-scale simulations [59] was less than 1%, one can conclude that the majority of the "error" term is instead balanced by the second term on the LHS of Eq. 3.24. This second term describes a difference in transpiration velocities. For cases BL1460 and BL3550, it can be seen

from Fig. 3.5d that the transpiration velocities of the single-scale simulations was greater than that of the growing simulation by at most 5%.

The error in the transpiration velocity to leading order of Re monotonically decays with log of Reynolds number. For larger Reynolds numbers, the agreement in shape factor is only expected to improve.

3.5 Conclusion

In this chapter, we investigated the transpiration velocity of single-scale periodic simulations. Unlike other simulations of turbulent boundary layers, the single-scale periodic boundary layer simulation does not impose a transpiration velocity. In this way, the transpiration velocity characterizes the numerical error in the streamwise periodic simulation. More specifically, after integrating continuity, the transpiration velocity error was primarily caused by a difference in inner and outer layer growth rates. A second streamwise periodic numerical framework was formulated to account for the differing layer growth rates. Doing so required generating a fit to smoothly transition from $2\delta_\nu'/\delta_\nu$ in the inner layer to Δ'/Δ in the outer layer. Under this framework, we verified that the transpiration velocity improved from at most 5% to 1% but the remaining mean and turbulent intensities were virtually unchanged. The streamwise periodic simulations appears insensitive to the transpiration velocity, and the "improved" numerical framework may be superfluous.

Finally, through an error budget of the mean continuity equation, the errors in mean continuity equation must manifest either as errors in the shape factor or as an errors the transpiration velocity. Based on low Reynolds number results, the former error is orders of magnitude smaller than the latter error. Furthermore, using a composite fit [10], it can be shown that this error vanishes with increasing Reynolds number. Thus, it can be concluded that for larger and more practical Reynolds numbers that the use of single-scale streamwise periodic simulations remains robust.

Chapter 4

TWO-POINT CORRELATIONS OF A HOMOGENIZED STREAMWISE PERIODIC BOUNDARY LAYER

The previous chapters investigated the accuracy of the one-point statistics (Chapter 2) and its behavior with respect to higher Reynolds numbers (Chapter 3). The results show consistently strong accuracy and are expected to improve even more at high Reynolds numbers. This behavior, combined with cheaper computation cost, gives optimism that the method can be used to capture turbulent boundary layer dynamics beyond mean velocity profiles. The bulk of the computational savings relies on a shortened streamwise domain ($7\delta_{99}$ vs $50\delta_{99}$). One might question whether these periodic simulations can contain the largest turbulent motions attributed to the boundary layer [16–20]. That is why the current chapter focuses on two-point statistics and investigates how different choices of domain sizes might affect the largest turbulent scales. Two-point correlations of the periodic boundary layer simulation for $Re_{\delta^*} = 5650$ will be directly compared to those of growing boundary layers [63] and simulations with larger domains.

4.1 Two-point statistics formulation and *a priori* analysis

In this section, the full cases are outlined, and the numerical method for computation of the two-point statistics is presented. This section also provides a validation of the one-point statistics for any additional cases.

4.1.1 Cases explored

The key motivating questions of interest are whether the simulations BL1460 and BL5650 from Chapter 2 have turbulent features that are 1) restricted by the computational domain and 2) similar to the growing boundary layer turbulent structures.

The first concern can be dealt with by conducting simulations with computational domains much longer in streamwise and spanwise extent. Following [21], we opt to run four additional simulations with extended domains for our lowest Reynolds number case, i.e. cases BL1460_x2, BL1460_xz2, BL1460_xz4. BL1460_x2 and BL1460_xz2 both have streamwise computational domains double that of BL1460, while BL1460_xz4 has a streamwise computational domain quadruple that of BL1460. BL1460_xz2 and BL1460_xz4 have spanwise computational domains

Case	Re_{δ^*}	$(L_x, L_y, L_z)/\delta_{99}$	$(\Delta x^+, \Delta y^+_{\text{min}}, \Delta z^+)$	Type	Legend
BL1460	1460	(7,3,2.5)	(9,0.3,6)	Periodic	- (black)
BL1460_x2	1460	(14,3,2.5)	(9,0.3,6)	Periodic	- (red)
BL1460_xz2	1460	(14,3,5)	(9,0.3,6)	Periodic	- (cyan)
BL1460_xz4	1460	(28,3,10)	(9,0.3,6)	Periodic	- (magenta)
BL5650	5650	(7,3,2.5)	(9,0.3,6)	Periodic	- (black)
Sill14	5650*	(78,4,12)	(7,0.2,4)	Growing	- (green)

Table 4.1: Parameters of numerical simulations performed. Consistent with Chapter 2, L_x, L_y, L_z are the streamwise, wall-normal, and spanwise domain lengths, $(\Delta x^+, \Delta y^+_{\text{min}}, \Delta z^+)$ are the respective resolutions. δ_{99} and δ_ν for Sill14 [63] are taken from theirs values at $Re_{\delta^*} = 5650$

double and quadruple that of BL1460, respectively.

The second concern can be dealt with by comparing the results of BL5650 with those of Sill14 (see Table 4.1). As the BL5650 is statistically homogeneous, the two-point correlations for the streamwise periodic boundary layer can be averaged them over the entire streamwise domain. Sillero *et al.* 2014 computed two-point correlations over streamwise boxes of length $\pm 10\delta_{99}$ and averaged over streamwise slabs of length $\pm 0.5\delta_{99}$. Over each slab, the boundary layer changes in Reynolds number by $\sim 0.5\%$ and over the entire correlation box, the Reynolds number changes by 10%. The specific Reynolds number ($Re_{\delta_*} = 5650$) chosen is at a streamwise location one-third of the way through the streamwise domain of Sill14.

All of the cases used in this chapter are summarized in Table 4.1. As mentioned in Chapter 2, the resolutions between the periodic and growing boundary layers are comparable, but the domain sizes are certainly different: case Sill14 uses over 420x more points than BL5650. The streamwise and spanwise domains of Sill14 are 15x and 5x larger than those of BL5650, respectively.

4.1.2 One-point statistics of extended domains

The streamwise mean and rms velocity profiles for the domain dimension simulations (BL1460_*) are provided in Fig. 4.1. The profiles are shown in inner scaling and there is good agreement for all domain sizes. The relative difference in the mean velocity profile is at most 0.5%, which is on the order of the statistical uncertainty computed for the mean from Chapter 2, Section 2.5. There are minute differences in $u^+_{1,\infty}$, but interestingly, the smallest domain features the "largest" value, and the largest domain featured the "smallest" value. As expected, the shape factor also features good agreement, with relative differences of at most 0.4%.

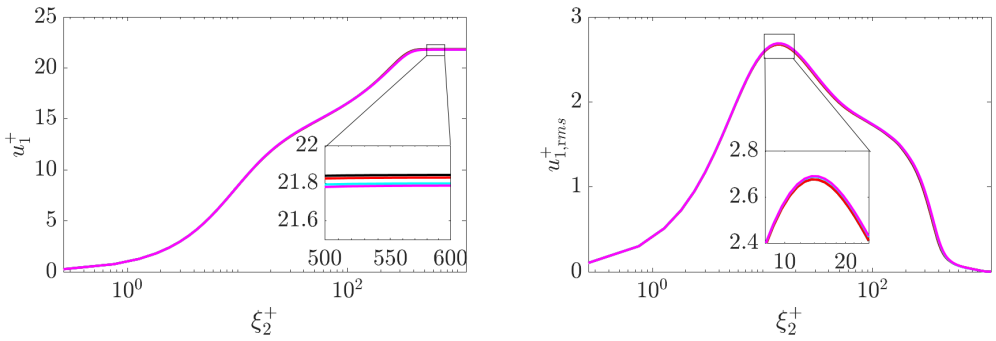

(a) Mean (b) rms

Figure 4.1: Streamwise (a) mean ($\overline{u}_1$) and (b) rms (u_1') profiles comparing the different cases in Table 4.1 for $Re_{\delta^*} = 1460$.

The rms profiles have relative differences being at most 2%, which is on the order of the statistical uncertainty computed for the rms from Chapter 2. Near the peak at $\xi_2^+ \approx 10$, the rms profiles of BL1460 and BL1460_x2 are nearly indistinguishable and are both distinct from BL1460_xz2 and BL1460_xz4. Increasing the spanwise domain has an effect on the rms profiles, if only slightly.

4.1.3 Computation of two-point statistics

Correlations are computed in physical space in the streamwise direction. The time-averaged autocorrelation in growing boundary layers is defined by

$$C^{\mathrm{g}}_{\phi\psi}(x_1, x_2, x_3, r_1, r_2, r_3) = \langle \phi(x_1, x_2, x_3), \psi(x_1 + r_1, x_2 + r_2, x_3 + r_3) \rangle_t / (\sigma_\phi \sigma_\psi) \tag{4.1}$$

where ψ, ϕ are arbitrary variables with zero mean, σ_ϕ is the standard deviation of ϕ at a specific location, and r_i are correlation distances. Consistent with notation described in Chapter 2, x_1, x_2, x_3 are the streamwise, wall-normal, and spanwise directions, respectively, and $\langle \cdot \rangle$ describes averaging.

It should be noted that the rescaling of the streamwise boundary layer produces the following relation between the homogenized correlation coefficient ($C^{\mathrm{h}}_{\psi\phi}$) and the growing correlation coefficient ($C^{\mathrm{g}}_{\psi\phi}$) for fixed $x_1, x_2, x_3, r_1, r_2, r_3$

$$C^{\mathrm{g}}_{\psi\phi} = \left\langle \phi\left(\xi_1, \xi_2 \frac{q(x_1)}{q_0}, \xi_3\right), \psi\left(\xi_1 + r_1, (\xi_2 + r_2)\frac{q(x_1 + r_1)}{q_0}, \xi_3 + r_3\right) \right\rangle_t / (\sigma_\phi \sigma_\psi) \tag{4.2}$$

After evaluating at $x_1 = x_0$ and Taylor expanding to first order, one gets the following relationship between the covariances of the streamwise growing ($C^{\mathrm{g}}_{\psi\phi}$) and the parallelized boundary layer ($C^{\mathrm{h}}_{\psi\phi}$)

$$C^{\mathrm{g}}_{\psi\phi} \approx C^{\mathrm{h}}_{\psi\phi} + \quad (4.3)$$

$$\left\langle \phi(\xi_1,\xi_2,\xi_3)(\xi_2+r_2)r_1\frac{q'}{q}\frac{\partial}{\partial\xi_2^*}\left[\psi(\xi_1+r_1,\xi_2^*,\xi_3+r_3)\right]|_{\xi_2^*=\xi_2+r_2}\right\rangle_t + \quad (4.4)$$

$$\left\langle \frac{\partial}{\partial\xi_2^*}\left(\phi(\xi_1,\xi_2^*,\xi_3)\right)|_{\xi_2^*=\xi_2}(\xi_2)r_1\frac{q'}{q}\frac{\partial}{\partial\xi_2^*}\left[\psi(\xi_1+r_1,\xi_2^*,\xi_3+r_3)\right]|_{\xi_2^*=\xi_2+r_2}\right\rangle_t \quad (4.5)$$

where a new correlation source term, $C^{\mathrm{src}}_{\psi\phi}$, has been produced. The superscripts differentiating the different autocorrelations will be dropped going forward and the coordinate system will be written in terms of (ξ_1,ξ_2,ξ_3).

4.2 Velocity correlations

In this section, two-dimensional autocorrelations and cross-correlations are presented, as well as analyses of the integral length-scale.

4.2.1 Single height 1D streamwise autocorrelations

Single height ($r_2 = 0$ and either $r_1 = 0$ or $r_3 = 0$) autocorrelation coefficients with respect to a single direction are often useful to verify that the simulation domain is large enough to contain fully decorrelated turbulence. These 1D correlations can be directly computed from 3D correlations via integration along the discarded direction. For example, the single-height streamwise autocorrelation of u_1 is given by

$$C_{uu,x}(\xi_1,r_1,\xi_2) = \int C_{uu}(\xi_1,\xi_2,\xi_3,r_1,r_2=0,r_3=0)d\xi_3 \quad (4.6)$$

Two-point correlations will be computed at three key locations $\xi_2 = 15\delta_\nu, \xi_2 = 0.1\delta_{99}, \xi_2 = 0.6\delta_{99}$ as representative of the inner layer, log layer, and outer layer, respectively.

The streamwise autocorrelation coefficient for the streamwise velocity component ($C_{uu,x}$) is shown in Fig. 4.2. The extended domain simulations (cases BL1460, BL1460_x2, BL1460_xz2, BL1460_xz4) produce results that agree well with each other for the near wall ($\xi_2 = 15\delta_\nu$) and lower log ($\xi_2 = 0.1\delta_{99}$) regions, specifically near the peak $r_1 = 0$. They feature relative differences of at most 2%. At ($\xi_2 = 0.1\delta_{99}$), BL1460 features a sharper drop-off in correlation with a maximum absolute

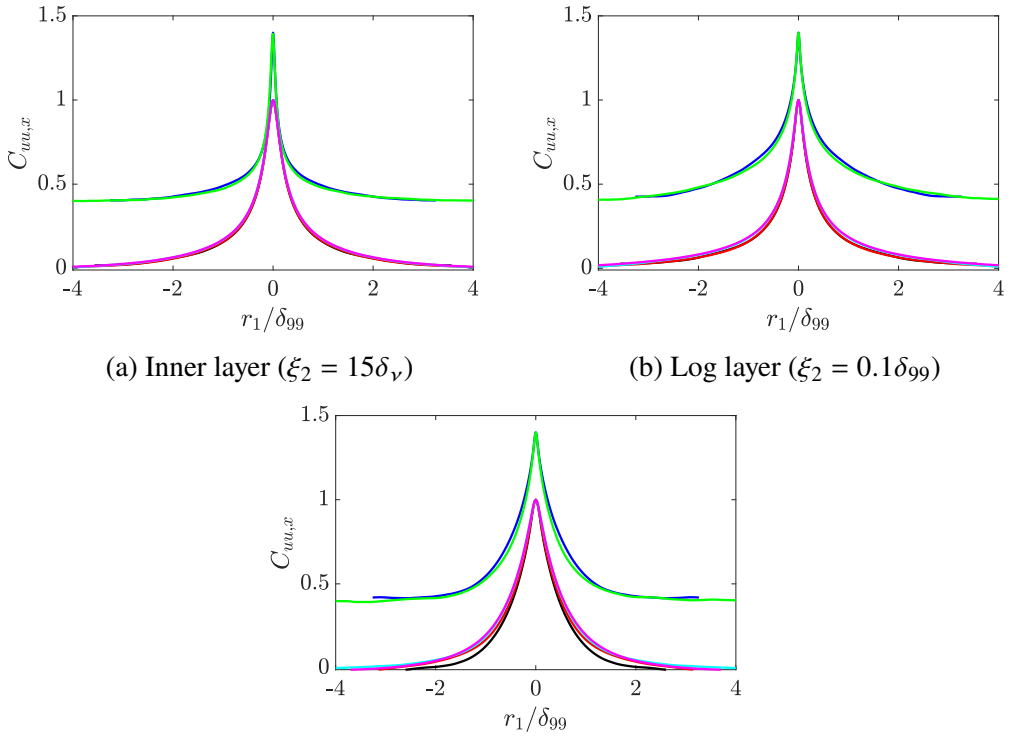

(a) Inner layer ($\xi_2 = 15\delta_\nu$)

(b) Log layer ($\xi_2 = 0.1\delta_{99}$)

(c) Outer layer ($\xi_2 = 0.6\delta_{99}$)

Figure 4.2: Single height streamwise autocorrelation function $C_{uu,x}$ (a) $\xi_2 = 15\delta_\nu$, (b) $\xi_2 = 0.1\delta_{99}$ and (c) $\xi_2 = 0.6\delta_{99}$. Simulations at $Re_{\delta^*} = 5650$ are offset by 0.4 for clarity. Legend is as given in Table 4.1.

error of 0.07. This indicates that in the wake region, the shortest domain has shorter streamwise structures, whereas all of the longer domains appear to overlap. Specifically, the BL1460_xz2 and BL1460_xz4 have wider lobes compared to the autocorrelations of BL1460_x2 and BL1460.

BL5650 and Sill14 show qualitative agreement. For all heights, the curves overlap for $r_1 < 0.25\delta_{99}$, and the maximum absolute difference between the autocorrelation function is 0.02. For all stations, the autocorrelation function of Sill14 appears to decrease faster than that of BL5650, which implies that the boundary layer of Sill14 is populated by slightly shorter purely streamwise structures. As will be shown in Section 5.3.2, the streamwise extents of C_{uu} are in fact greater for Sill14 due to the inclination angle of the autocorrelation function. The correlation coefficients at these locations eventually decay to less than 2% of the total value (Fig. 4.2), which is on the order of statistical uncertainty for the flow. Since the autocorrelations in the outer layer scale with the outer length-scale, streamwise domains between $7\delta_{99}$ and $14\delta_{99}$ for fully decorrelated turbulence.

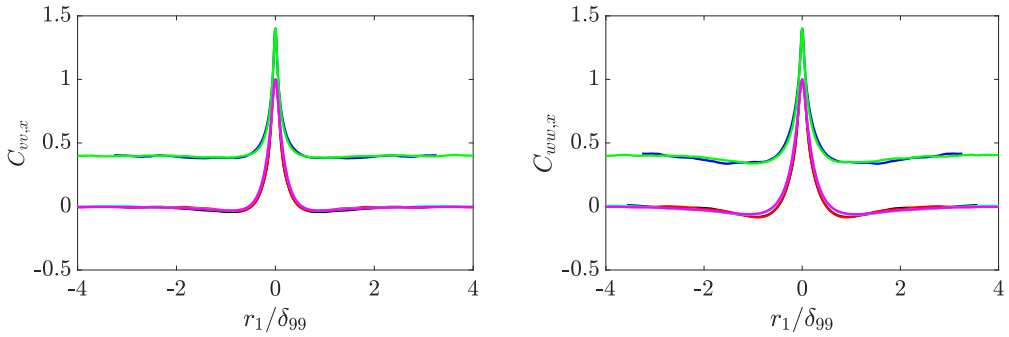

(a) Wall-normal velocity

(b) Spanwise velocity

Figure 4.3: Single height streamwise autocorrelation function for (a) wall-normal $C_{vv,x}$ and (b) spanwise $C_{ww,x}$ velocity components. Simulations at $Re_{\delta^*} = 5650$ are offset by 0.4 for clarity. Legend as provided in Table 4.1.

The streamwise autocorrelations for the spanwise ($C_{ww,x}$) and wall-normal velocities ($C_{vv,x}$) are shown (Fig. 4.3) at one location: $\xi_2 = 0.6\delta_{99}$. The autocorrelations at the inner and log layer locations behave similarly to $C_{uu,x}$ and are therefore omitted. Note that the streamwise extent of the autocorrelations for the spanwise and wall-normal velocity components is about $1\delta_{99}$ less than that of the streamwise velocity component, and they appear less affected by domain size changes.

The profiles for $C_{vv,x}$ are virtually indistinguishable for each set of Re_{δ^*}. $C_{ww,x}$ features differences at $r_1 = 1\delta_{99}$ for the $Re_{\delta^*} = 1460$ cases. Specifically, BL1460 and BL1460_x2 appear to overlap whereas BL1460_xz2 and BL1460_xz4 deviate slightly. Specifically, the outermost lobes of $C_{vv,x}$ for both BL1460 and BL1460_x2 appear to reach zero earlier than those of $C_{vv,x}$ for the extended domain cases (BL1460_xz2, BL1460_xz4), potentially indicating that the turbulent structures for even BL1460_x2 are shorter than those of BL1460_xz2.

4.2.2 Single height 1D spanwise autocorrelations

The single-height spanwise autocorrelation coefficient for the streamwise velocity component ($C_{uu,z}$) is shown in Fig. 4.4. The near wall ($\xi_2 = 15\delta_\nu$) autocorrelations are nearly indistinguishable. The sharp negative lobe is captured for both BL5650 and BL1460. BL5650 and Sill14 at $\xi_2 = 0.1\delta_{99}$ are within 5% of each other. The similar statements can be made for the domain extension cases BL1460, but BL1460 deviates near the negative lobe. It has been previously noted [63] that the spanwise widths of the autocorrelation functions (and consequently the turbulent structures) scale with wall-normal height. This is indeed the case for both the periodic and growing boundary layers.

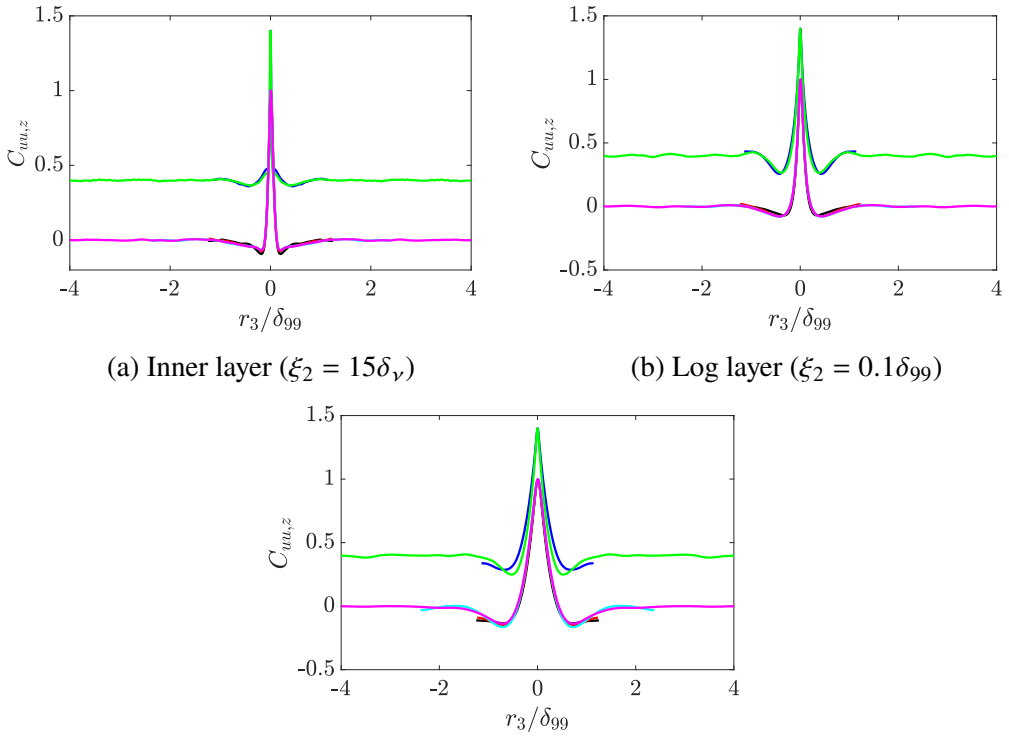

(a) Inner layer ($\xi_2 = 15\delta_\nu$)

(b) Log layer ($\xi_2 = 0.1\delta_{99}$)

(c) Outer Layer ($\xi_2 = 0.6\delta_{99}$)

Figure 4.4: Single height spanwise autocorrelation function $C_{uu,z}$ (a) $\xi_2 = 15\delta_\nu$, (b) $\xi_2 = 0.1\delta_{99}$ and (c) $\xi_2 = 0.6\delta_{99}$. Simulations at $Re_{\delta^*} = 5650$ are offset by 0.4 for clarity. Legend is as given in Table 4.1.

For $r < 0.5$, the autocorrelation function $C_{uu,z}$ at $\xi_2 = 0.6\delta_{99}$ for BL5650 and Sill14 are within 5% of each other. However, $C_{uu,z}$ for BL5650 does not entirely vanish at the end of the correlation and instead plateaus to approximately -0.07, whereas both BL1460_x2 and BL1460 plateau to -0.1. An increase in spanwise domain dimension resolves the issue as both BL1460_xz4 and BL1460_xz2 capture the full spanwise width of the autocorrelation. Since the autocorrelations in the outer layer scale with the outer length-scale, spanwise domains of $5\delta_{99}$ are sufficient to capture the full autocorrelation.

The spanwise and wall-normal autocorrelations ($C_{vv,z}, C_{ww,z}$) are shown for $\xi_2 = 0.6\delta_{99}$ in Fig. 4.5. The domain dimension has little effect on the outermost lobes of the autocorrelation function and the contours are within 5% of each other. $C_{ww,z}$ mirrors $C_{uu,z}$ in that the shorter spanwise domains do not acheive full decorrelation. BL5650 achieves a final value of -0.06 whereas BL1460 and BL1460_x2 achieve a final value of -0.08.

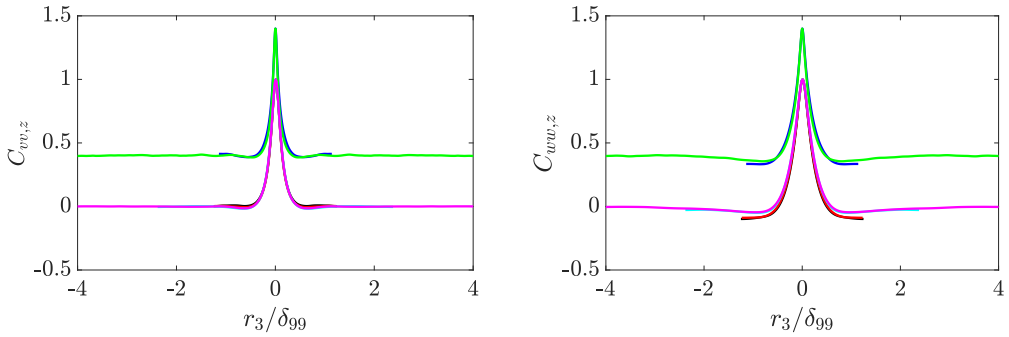

(a) Wall-normal velocity (b) Spanwise velocity

Figure 4.5: Single height spanwise autocorrelation function for (a) wall-normal $C_{vv,z}$ and (b) spanwise $C_{ww,z}$ velocity components. Simulations at $Re_{\delta^*} = 5650$ are offset by 0.4 for clarity. Legend as provided in Table 4.1.

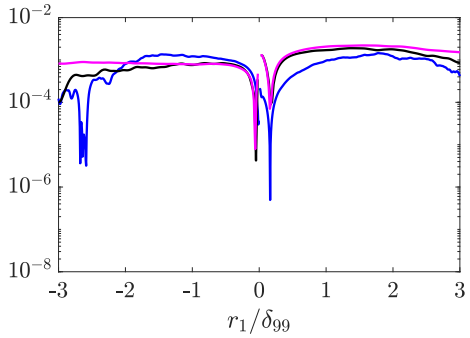

Figure 4.6: Magnitude of error term from Eq. 4.5 $C_{uu,x}$ for $\xi_2 = 0.6\delta_{99}$, for BL1460, BL1460_xz4 and BL5650. Legend is as provided in Table 4.1.

4.2.3 Error term & integral length-scale

The magnitude of the error term due to the rescaling (Eq.4.5) for the 1D streamwise autocorrelation function is shown in Fig. 4.6 for BL1460, BL1460_xz4 and BL5650 at $\xi_2 = 0.6\delta_{99}$. This wall-normal location was chosen as it is where $C_{uu,x}$ had the largest discrepancies between cases of the same Re_{δ^*}. As shown, magnitude of the error term is only 10^{-3} and is orders of magnitude smaller than the actual autocorrelation term. This result is not altogether unsurprising. The mean turbulent kinetic energy (TKE) is used to normalize the autocorrelation function, and so one might expect both the TKE and the autocorrelation function to share sensitivity (and insensitivity) to the same variables. Because the rescaling operation has been demonstrated to have little impact on the turbulent kinetic energy budget (Chapter 2), one might also have expected similar for the autocorrelation function as well.

The streamwise integral length-scale for the streamwise velocity component can be

Case	I_x^u	I_z^u
BL1460	0.90	0.33
BL1460_x2	1.01	0.35
BL1460_xz2	1.10	0.36
BL1460_xz4	1.08	0.36
BL5650	0.92	0.28
Sill14	0.85	0.26

Table 4.2: Integral length-scales computed using Eq. 4.7 at $\xi_2 = 0.6\delta_{99}$.

defined as

$$I_x^{u_1} = \int_0^{z_0} C_{uu,x} dr_i \tag{4.7}$$

where z_0 is the first zero crossing of the autocorrelation. Similar quantities can be defined for the other velocity components and for the spanwise integral length-scale.

The streamwise and spanwise integral length-scales for $\xi_2 = 0.6\delta_{99}$ are provided in Table 4.2. The streamwise integral length-scales for $\xi_2 = 0.6\delta_{99}$ are approximately $1\delta_{99}$. Consistent with the results shown in Section 4.2.1, a spanwise domain of at least $5\delta_{99}$ produces a converged streamwise integral length-scale.

The spanwise integral length-scale is deceptive, as the current definition Eq. 4.7 gives a value of $\sim 0.4\delta_{99}$, whereas the spanwise extent is much larger than just 0.4 δ_{99}. This spanwise extent is largely due to the negative lobes of autocorrelation. These lobes are small in magnitude but also have longer spanwise extent, and so their contribution to the integral length-scale is minimal.

Throughout this section, it has been shown that periodic boundary layers agree well with streamwise growing boundary layers with regards to 1D single-height autocorrelations. In particular, despite only having a streamwise domain of $\sim 7\delta_{99}$, BL5650 showed strong agreement for $r_3 < 0.8$. It furthermore appears that a streamwise domain size of $14\delta_{99}$ and a spanwise domain size of $5\delta_{99}$ are sufficient to capture the full 1D autocorrelations.

4.2.4 Two-dimensional autocorrelations

We now focus on two-dimensional slices of the correlation function, centering on two key locations: $\xi_2 = 0.1\delta_{99}$ in the lower logarithmic layer and $\xi_2 = 0.6\delta_{99}$ in the wake region.

Figure 4.7 presents the streamwise sections ($C_{uu,xy}$) for BL5650, Sill14, and the cases run at $Re_{\delta^*} = 1460$. For all cases, the streamwise correlations $C_{uu,xy}$ are

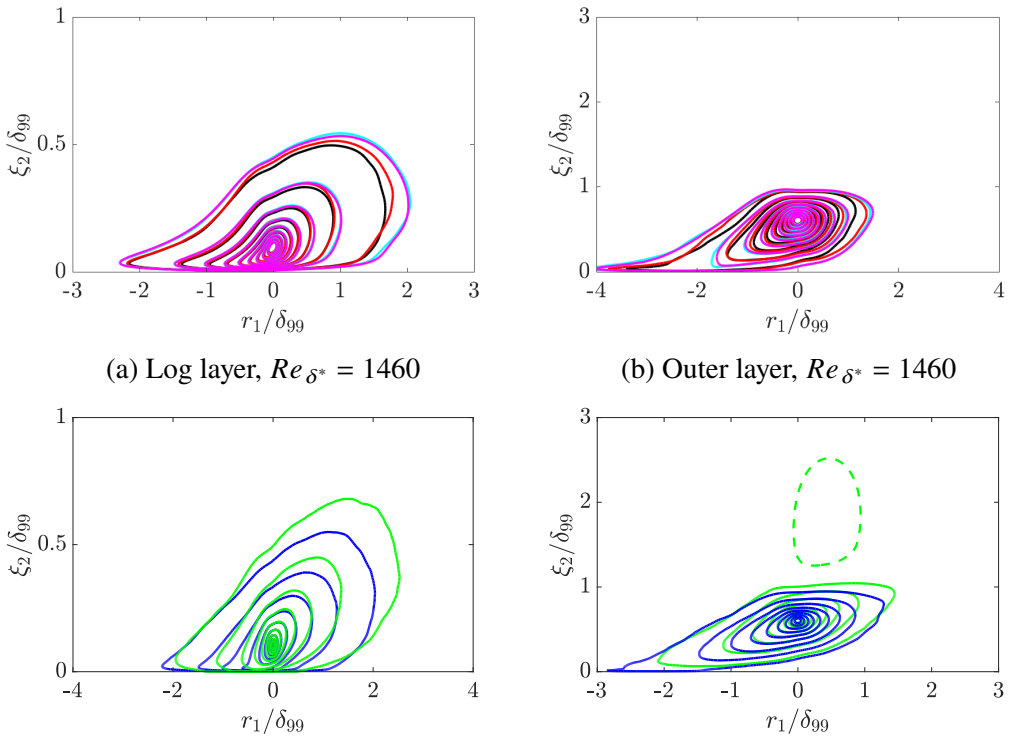

(a) Log layer, $Re_{\delta^*} = 1460$

(b) Outer layer, $Re_{\delta^*} = 1460$

(c) Log layer, $Re_{\delta^*} = 5650$

(d) Outer layer, $Re_{\delta^*} = 5650$

Figure 4.7: Streamwise sections ($C_{uu,xy}$) of the autocorrelation function for $Re_{\delta^*} = 1460$ at (a) $\xi_2 = 0.1\delta_{99}$, and (b) $\xi_2 = 0.6\delta_{99}$ and for $Re_{\delta^*} = 5650$ at (c) $\xi_2 = 0.1\delta_{99}$ and (d) $\xi_2 = 0.6\delta_{99}$. Legend is as given in Table 4.1. Positive contours are from [0.1:0.1:1.0]. Negative contours are from [-0.1:-0.1:-1] and are shown as dashed.

inclined with respect to the wall, and this inclination appears to increase with height. Consistent with the 1D results shown in the previous section, the 2D autocorrelations agree well for $r_1 < 0.8\delta_{99}$. Furthermore, both BL5650 and Sill14 appear to agree on an incline angle of approximately 15° for $\xi_2 = 0.1\delta_{99}$. The outermost contour of the autocorrelation, $C_{uu,xy} = 0.1$ of Fig. 4.7, corresponds to the largest turbulent structures and it decays faster for BL5650 than for Sill14. A similar behavior is observed in the BL1460 cases, where the BL1460 autocorrelation decays more quickly than that of BL1460_x2, BL1460_xz2, and BL1460_xz4. The sudden drop in autocorrelation is chiefly due to domain size. Furthermore, because there are differences between BL1460_x2 and BL1460_xz2 in autocorrelation extent, it is clear that the spanwise domain is critical to capturing an accurate autocorrelation coefficient.

Surprisingly, at $\xi_2 = 0.6\delta_{99}$, the correlation function for Sill14 appears to reach into the free-stream with lobes of negative correlation. This behavior isn't present in

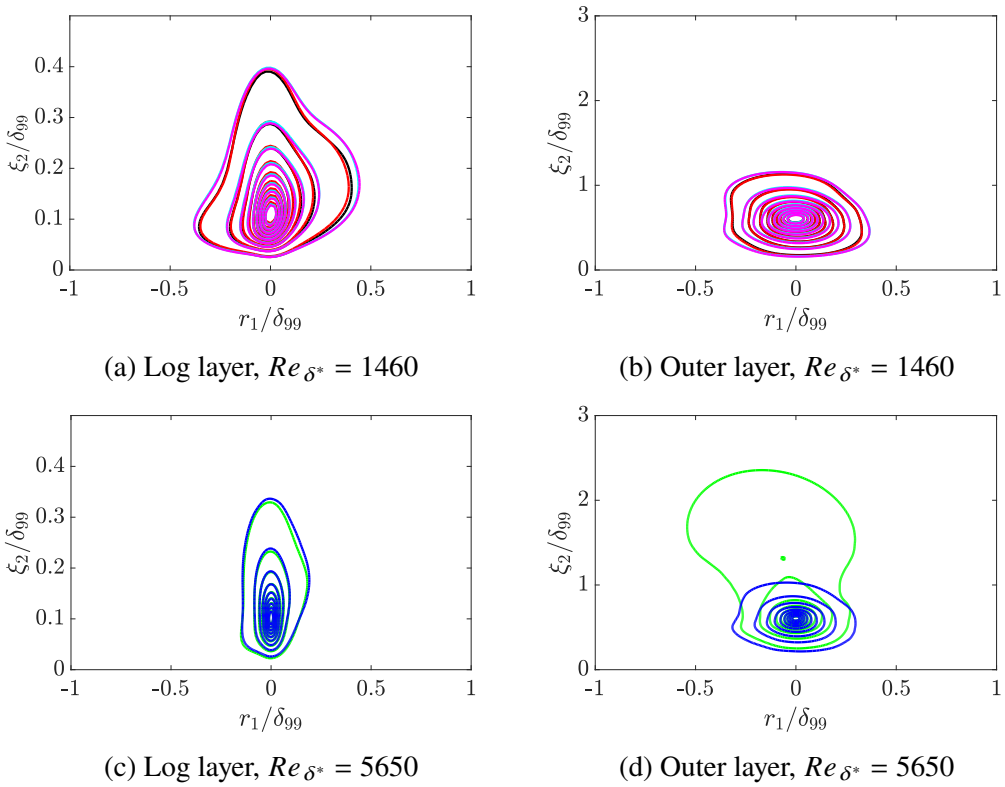

(a) Log layer, $Re_{\delta^*} = 1460$

(b) Outer layer, $Re_{\delta^*} = 1460$

(c) Log layer, $Re_{\delta^*} = 5650$

(d) Outer layer, $Re_{\delta^*} = 5650$

Figure 4.8: Streamwise sections (C_{vv,x,ξ_2}) of the autocorrelation function for $Re_{\delta^*} = 1460$ at (a) $\xi_2 = 0.1\delta_{99}$ and (b) $\xi_2 = 0.6\delta_{99}$, and for $Re_{\delta^*} = 5650$ at (c) $\xi_2 = 0.1\delta_{99}$ and (d) $\xi_2 = 0.6\delta_{99}$. Legend is as given in Table 4.1. Positive contours are from [0.1:0.1:1.0]. Negative contours are from [-0.1:-0.1:-1] and are shown as dashed.

either BL5650 or any of the BL1460 results, all of which remain within $1\delta_{99}$ of the wall. Similar free-stream correlations appear in the streamwise autocorrelation of the wall-normal ($C_{vv,xy}$) and spanwise ($C_{vv,xy}$) components (Figs. 4.8d and 4.9d). This behavior is further discussed in Section 4.2.6.

Besides these free-stream correlations, for both $C_{vv,xy}$ and $C_{ww,xy}$, BL5650 shares many of the same features with Sill14 (Fig. 4.8-4.9). Similar to $C_{uu,xy}$ there is an additional extension of the autocorrelation function upstream and towards the wall for BL5650.

The impact of domain extension is less dramatic for both $C_{vv,xy}$ and $C_{ww,xy}$, as the outermost contour is only extended by a maximum of 8%. The autocorrelation functions for BL1460 and BL1460_x2 nearly overlap for all locations and velocities. For u_2 and u_3, the autocorrelation functions appear to be more sensitive to spanwise extensions of the domain rather than streamwise extensions.

Figure 4.10 displays the spanwise autocorrelation of the streamwise velocity com-

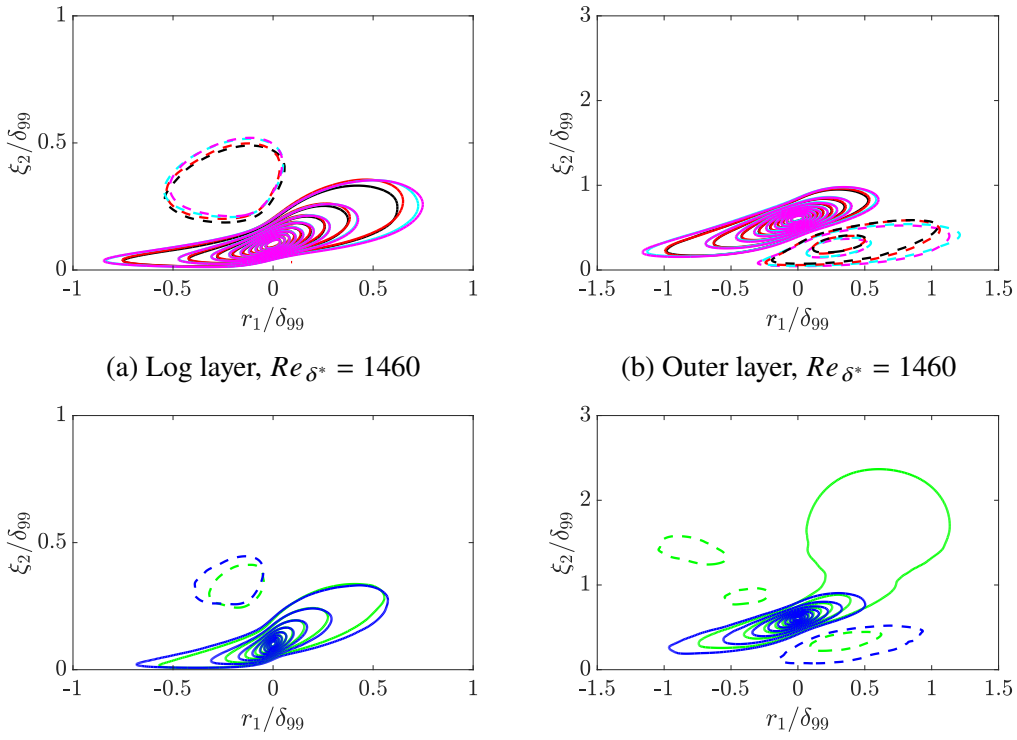

(a) Log layer, $Re_{\delta^*} = 1460$

(b) Outer layer, $Re_{\delta^*} = 1460$

(c) Log layer, $Re_{\delta^*} = 5650$

(d) Outer layer, $Re_{\delta^*} = 5650$

Figure 4.9: Streamwise sections ($C_{ww,xy}$) of the autocorrelation function for $Re_{\delta^*} = 1460$ at (a) $\xi_2 = 0.1\delta_{99}$ and (b) $\xi_2 = 0.6\delta_{99}$, and for $Re_{\delta^*} = 5650$ at (c) $\xi_2 = 0.1\delta_{99}$ and (d) $\xi_2 = 0.6\delta_{99}$. Legend is as given in Table 4.1. Positive contours are from [0.1:0.1:1.0]. Negative contours are from [-0.1:-0.1:-1] and are shown as dashed.

ponent ($C_{uu,zy}$). In all three cases, the spanwise extent of the correlations does not appear to surpass $2\delta_{99}$ and appears to grow with height. The effect of shortening the spanwise domain is visible in the negative lobes of $C_{uu,zy}$ at $\xi_2 = 0.6\delta_{99}$. With a larger streamwise domain, negative lobes to the left and right are recovered. As with $C_{vv,xy}$ and $C_{ww,xy}$, $C_{uu,zy}$ for Sill14 at $\xi_2 = 0.6\delta_{99}$ features correlations that reach deep into the free-stream.

Finally, only the spanwise sections ($C_{ww,zy}$) are shown (Fig. 4.11), as $C_{vv,zy}$ behaves similarly. Note that spanwise symmetry is expected as there is no mean flow in the spanwise direction. The autocorrelation function is surprisingly larger for BL5650 than for Sill14 in contrast to previous autocorrelations.

4.2.5 Discussion of turbulent structures

The streamwise extent of the autocorrelation function is approximately $O(4-5\delta_{99})$, which is consistent with experimentally observed autocorrelation lengths as well as

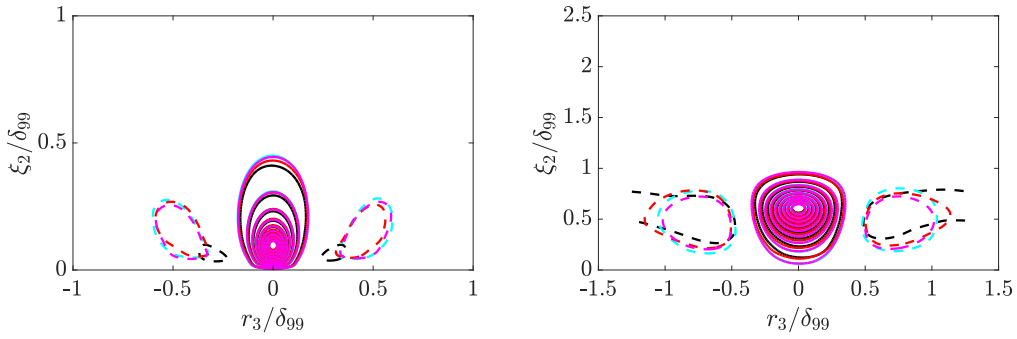

(a) Log layer, $Re_{\delta^*} = 1460$

(b) Outer layer, $Re_{\delta^*} = 1460$

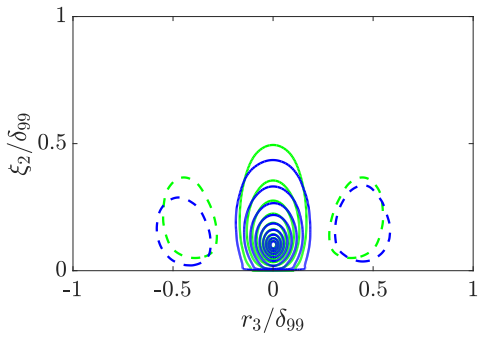

(c) Log layer, $Re_{\delta^*} = 5650$

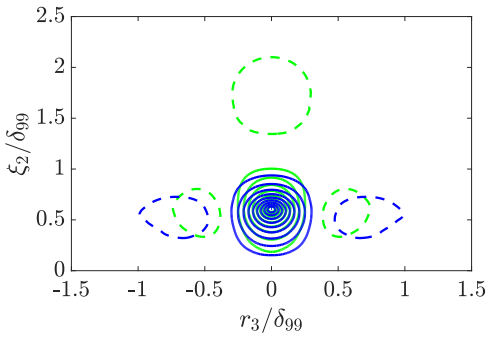

(d) Outer layer, $Re_{\delta^*} = 5650$

Figure 4.10: Spanwise sections ($C_{uu,zy}$) of the autocorrelation function for $Re_{\delta^*} = 1460$ at (a) $\xi_2 = 0.1\delta_{99}$ and (b) $\xi_2 = 0.6\delta_{99}$, and for $Re_{\delta^*} = 5650$ at (c) $\xi_2 = 0.1\delta_{99}$ and (d) $\xi_2 = 0.6\delta_{99}$. Legend is as given in Table 4.1. Positive contours are from [0.1:0.1:1.0]. Negative contours are from [-0.1:-0.1:-1] and are shown as dashed.

spectra [44]. Based on Fig. 4.7, even domain sizes of $O(7\delta_{99})$ are still not sufficient to capture the full range of the autocorrelation function. A similar observation has been noted in channel flows of shortened streamwise domain size [21, 22, 63, 64].

The streamwise extent of autocorrelation functions are not necessarily representative of the streamwise lengths of the longest turbulent structures within the flow ($O(20\delta_{99})$) [17]. Thus, to fully capture the longest structures, one might expect a streamwise domain requirement of at least $20\delta_{99}$. However, it has been argued by [21, 22, 63, 64], that these structures exist in the simulated flows with shorter domains, but are simply aliased onto structures of shorter length. Regardless of whether these claims are true or not, the two-point correlations of Section 4.2.4 show that these authors' claims can only be true provided the spanwise domain is sufficiently large (e.g. $L_z \approx 5\delta_{99}$). Due to the small aspect ratios of large scale motions in the wake, narrow spanwise domains may artificially limit the maximum length of wider structures within the computational domain.

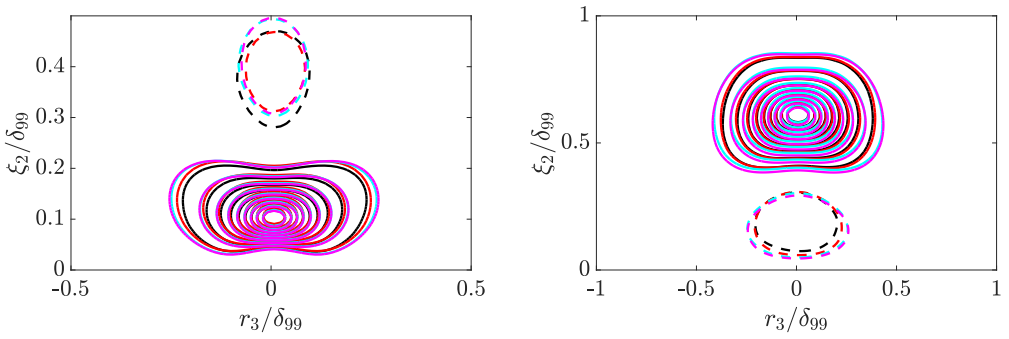

(a) Log layer, $Re_{\delta^*} = 1460$ (b) Outer layer, $Re_{\delta^*} = 1460$

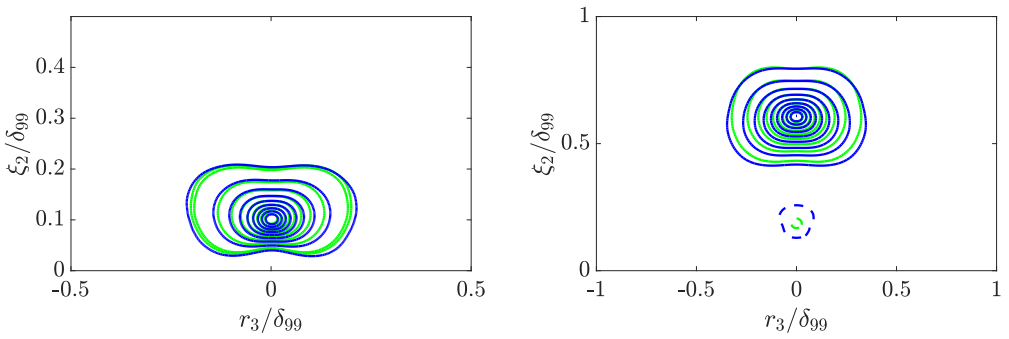

(c) Log layer, $Re_{\delta^*} = 5650$ (d) Outer layer, $Re_{\delta^*} = 5650$

Figure 4.11: Spanwise sections ($C_{ww,zy}$) of the autocorrelation function for $Re_{\delta^*} = 1460$ at (a) $\xi_2 = 0.1\delta_{99}$, and (b) $\xi_2 = 0.6\delta_{99}$ and for $Re_{\delta^*} = 5650$ at (c) $\xi_2 = 0.1\delta_{99}$ and (d) $\xi_2 = 0.6\delta_{99}$. Legend is as given in Table 4.1. Positive contours are from [0.1:0.1:1.0]. Negative contours are from [-0.1:-0.1:-1] and are shown as dashed.

4.2.6 Discussion of free-stream correlations

All of the streamwise sections ($C_{uu,xy}$,$C_{vv,xy}$, $C_{ww,xy}$) of Sill14 at $\xi_2 = 0.6\delta_{99}$ feature correlations that cross the boundary layer thickness ($\xi_2 > 1\delta_{99}$). No such behavior was found for any of the periodic boundary layer cases.

At first glance, it is possible that this effect is numerical. The code used for Sill14 was noted [16] to have free-stream fluctuations in the inlet plane. Specifically, the authors stated that "the residual free-stream fluctuations consist mostly of large-scale vorticity waves advected by the free-stream, and introduced at the inflow by the sloshing created by the interaction of the boundary layer with the exit. Such fluctuations are unavoidable. The streamwise derivatives $[\partial_{x_1} u_2]$ and $[\partial_{x_1} u_3]$ cannot be imposed at the inflow boundary, and there is no way of enforcing the strict irrotationality of the inflow. The incoming vorticity is fixed by the global pressure fluctuations, which are in turn created when the largest eddies leave the domain." It is possible that coherent structures in the wake region might form spurious correlations

with the noted artificial vortices of similar size in the free-stream.

In contrast, no such correlation exists in the periodic boundary layer. In a growing boundary layer, an arbitrary disturbance in the free-stream is advected vertically by the transpiration velocity $u_{2,\infty}$. Because the boundary layer displacement thickness grows at a rate of $u_{2,\infty}/u_{1,\infty}$, the disturbance's height, relative to δ^*, remains constant. However, since δ_{99} is known to grow faster than δ^*, the disturbance, relative to δ_{99}, will eventually enter the boundary layer. Given enough streamwise distance, any disturbance from the inlet will eventually be entrained into the boundary layer due to this effect. The periodic boundary layer shows this effect most directly through the linearized rescaled momentum equation. After neglecting the nonlinear terms, approximating $\overline{u}_i$ by $u_{i,\infty}$, zeroing out mean shear terms $\partial_{\xi_j}\overline{u}_i$, and assuming a negligible pressure gradient, one has that for a small perturbation u_1' initially residing in the free-stream:

$$\frac{\partial u_1'}{\partial t} + u_{1,\infty}\frac{\partial u_1'}{\partial \xi_1} + \left(u_{2,\infty} - \frac{q'}{q}\xi_2\overline{u}_1\right)\frac{\partial u_1'}{\partial \xi_2} = \nu\frac{\partial^2 u_1'}{\partial \xi_k^2} \tag{4.8}$$

The cross-boundary layer correlations shown in $C_{uu,xy}$, $C_{vv,xy}$, and $C_{ww,xy}$ all appear to be of streamwise extent $1\delta_{99}$. At this wavelength and Reynolds number, the impact of viscosity is small.

Given that $u_{2,\infty} > q'/q\delta^*$ and in the free-stream $\xi_2 > \delta_{99}$, the effective wall-normal velocity is negative and wall-normal advection will eventually draw the fluctuation into the periodic boundary layer. For example, normalized by the free-stream velocity, a disturbance initially at $2\delta_{99}$ will reach the boundary layer thickness $1\delta_{99}$ after approximately $2.2\delta_{99}/u_\tau$ or approximately 10-20% of most boundary layer simulations' [14, 16, 39, 65] convergence times. For periodic simulations, this analysis implies that with enough time, the free-stream will be free of initial disturbances.

4.2.7 Reynolds stress correlations

The Reynolds shear stress is an indicator of momentum transfer from the near wall region to the outer region [66, 67]. In particular, there is interest in its behavior in the near-wall cycle and in the outer regions. Figures 4.12 show the Reynolds shear stress correlations ($C_{uv,\xi_1\xi_2}$) at the heights of $\xi_2 = 15\delta_\nu$ ($\xi_2 \approx 0.04\delta_{99}$) and $\xi_2 = 0.6\delta_{99}$ for $Re_{\delta^*} = 5650$.

It should be noted that unlike the autocorrelations with are perfectly normalized, the cross-correlation is only nondimensionalized by the standard deviations of u_1 and u_2. Consequently, the magnitude of the peak of the cross-correlation is approximately -0.5 for $\xi_2 = 15\delta_v$ and $\xi_2 = 0.6\delta_{99}$. The peak location for the cross-correlation is also likewise changed to be offset at around $r_1^+ \approx 5$ and $r_2^+ \approx 5$. The correlations are also opposite in sign, matching the overall sign of the Reynolds shear stress.

Consistent with many of the previous contours, $C_{uv,\xi_1\xi_2}$ for BL5650 shares qualitative similarities with that of Sill14 near the wall, and far from the wall, they compare favorably. The outer location $\xi_2 = 0.6\delta_{99}$ does show an interesting agreement, as both BL5650 and Sill14 agree on both an area of positive correlation outside of the boundary layer as well as an area of negative correlation. The fact that both simulations agree on this connection indicates that the correlation is unlikely to be due to initial conditions or inflow effects.

Having both positively and negatively correlated u_2' is indicative of large-scale vorticity in the free-stream. On the other hand, the large area of negative correlation within the boundary layer indicates either ejection or sweeping style behaviors, both of which involve movement of a large scale structure towards or away from the boundary layer edge. This mechanism is likely the same one as noted by Kim *et al.* (2017), which allows large scale motions in the log and outer layers to wrinkle the turbulent/non-turbulent interface. Regardless of the cause of the correlations crossing the free-stream, the domain sizes for BL5650 appear adequate to capture the key features of the Reynolds shear stress cross-correlations.

4.3 Conclusion

Throughout this chapter, it has been shown that the domain size required for periodic boundary layer simulation is much larger than the expected requirement to capture the integral length-scales ($\sim 1\delta_{99}$) and the LSMs ($3 - 4\delta_{99}$). Furthermore, it was shown that the spanwise domain must be of a certain size to fully capture large scale motions in the streamwise direction. Overall, it is expected that with domain dimensions of $L_x \approx 14\delta_{99}$ and $L_z \approx 5\delta_{99}$, one has a sufficiently large domain to capture the full two-point correlation functions for the flow. The cost-savings from Chapter 2 still apply, albeit to a slightly subdued degree.

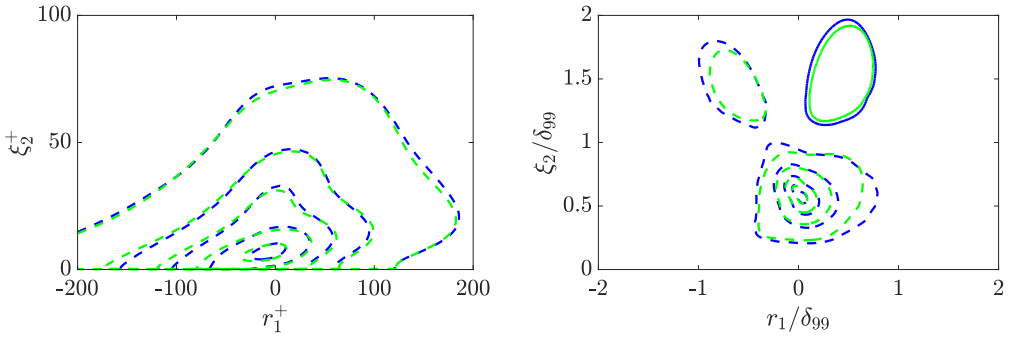

(a) Inner layer (b) Outer layer

Figure 4.12: Streamwise sections ($C_{uv,\xi_1\xi_2}$) of the cross-correlation function for $Re_{\delta^*} = 1460$ at (a) $\xi_2 = 0.1\delta_{99}$ and (b) $\xi_2 = 0.6\delta_{99}$, and for $Re_{\delta^*} = 5650$ at (c) $\xi_2 = 0.1\delta_{99}$ and (d) $\xi_2 = 0.6\delta_{99}$. Legend is as given in Table 4.1. Positive contours are from [0.1:0.1:1.0]. Negative contours are from [-0.1:-0.1:-1] and are shown as dashed.

Chapter 5

TURBULENT STRUCTURES AND THEIR PREDICTION

The previous chapters dealt with the various one-point and two-point statistics of the streamwise periodic boundary layer. In this section, we first compute the power spectral density of the boundary layer flow and discuss different locations of interest. The specific spatial and temporal frequencies motivate the proceeding sections: turbulent structure prediction and extraction. The key tool for this is the resolvent formalism [38], specifically that of the 1D resolvent, which is introduced in this chapter and is heavily dependent on the choice of frequency. We apply it to the periodic boundary layer and the corresponding rescaled governing equations. The resolvent operators for various frequencies are given and their singular spectra and response modes are examined. Finally, spectral proper orthogonal decomposition (SPOD) [25] is introduced and applied to data of BL1460. The extracted results are finally compared to predicted modes from the resolvent operator.

5.1 Spectra

In this section, the power spectral density (PSD) is computed for the boundary layer. Specific focus is placed on the computation of the PSD in time as the most energetic modes will be the focus of investigation for subsequent sections.

5.1.1 Spatial spectra

Energy spectra allow one to determine the general sizes of the most energetic flow features and associate peaks in kinetic energy spectra with specific observed mechanisms. For pipe and channel flows, streamwise spectra have proved useful in estimating the relative sizes of the most energetic motions[64, 68, 69].

In contrast, growing boundary layers are not by nature streamwise homogeneous and therefore, computing streamwise spectra cannot normally be done. To compensate for this, approximate spectra are computed by taking Fourier transforms of either windowed streamwise autocorrelation functions or symmetric components of the autocorrelation function:

$$C^{even}_{uu,x}(r_1) = \frac{1}{2}(C_{uu,x}(-r_1) + C_{uu,x}(r_1)) \tag{5.1}$$

Due to the boundary layer's quasi parallel growth, the odd components of the single-

height 2D autocorrelation have magnitude of less than 5% of the even components. In the case of the periodic boundary layer, direct Fourier Transforms can be taken.

For a streamwise and spanwise periodic stationary flow, like the periodic boundary layer, one has the following definition for power spectral density

$$E_{uu}(\kappa_1, \xi_2, \kappa_3, \omega) = \frac{1}{2} \iiint e^{-i\kappa_1 r_1 - i\kappa_3 r_3 + i\omega r_t}$$
$$\langle u_i(\xi_1, \xi_2, \xi_3, t) u_i(\xi_1 + r_1, \xi_2, \xi_3 + r_3, t + r_t) \rangle_{\xi_1, \xi_3, t} dr_1 dr_3 dr_t \tag{5.2}$$

where $(\kappa_1, \kappa_3, \omega)$ are the streamwise, spanwise, and temporal wavenumbers which are related to their respective "wavelengths" by $\lambda_1 = 2\pi/\kappa_1$, $\lambda_3 = 2\pi/\kappa_3$, $\lambda_t = 2\pi/\omega$.

One should also note that the streamwise spatial spectra in Cartesian coordinates are not quite the same as the streamwise spatial spectra in rescaled coordinates. The physical analogue is to compare waves at constant x_2 in the Cartesian case and waves at constant ξ_2 in the rescaled coordinate case. Notably, there is a difference associated with the rescaling: coordinate lines at constant ξ_2 are slightly inclined with respect to the wall.

This alignment error between Cartesian and rescaled grids for the spatial spectra has an autocorrelation analogue. In Chapter 4, it was estimated and was found to be orders of magnitude smaller than the autocorrelation function. Since the energy spectra is the Fourier transform of the autocorrelation function, the error associated with computing Fourier transforms at constant x_2 vs. ξ_2 is also negligible. Therefore, direct comparisons between spatial spectra are appropriate. Further discussion is provided in Section 5.2.6. It should be noted that the majority of experimental measurements for boundary layer streamwise spectra broadly rely on Taylor's hypothesis of frozen turbulence to convert temporal spectra (from hotwire probes) into spatial spectra [70–76]. The reader is referred to [77, 78] for more details regarding the applicability of Taylor's hypothesis to boundary layer flow. Full spatio-temporal spectra have been measured via particle image velocimetry [78–80], but often face challenges of grid resolution and optimal window size. For an in-depth analysis of spatio-temporal spectra of the boundary layer, the reader is referred to [81].

We first present a comparison of premultiplied spatial spectra, namely the PSD integrated over all ω, for Sill14, BL5650, and BL1460 at the inner layer location $\xi_2^+ = 15$ (Fig. 5.1). The premultiplication of spectra is meant so that each decade of wavenumbers contains the same total amount of turbulent kinetic energy; upon

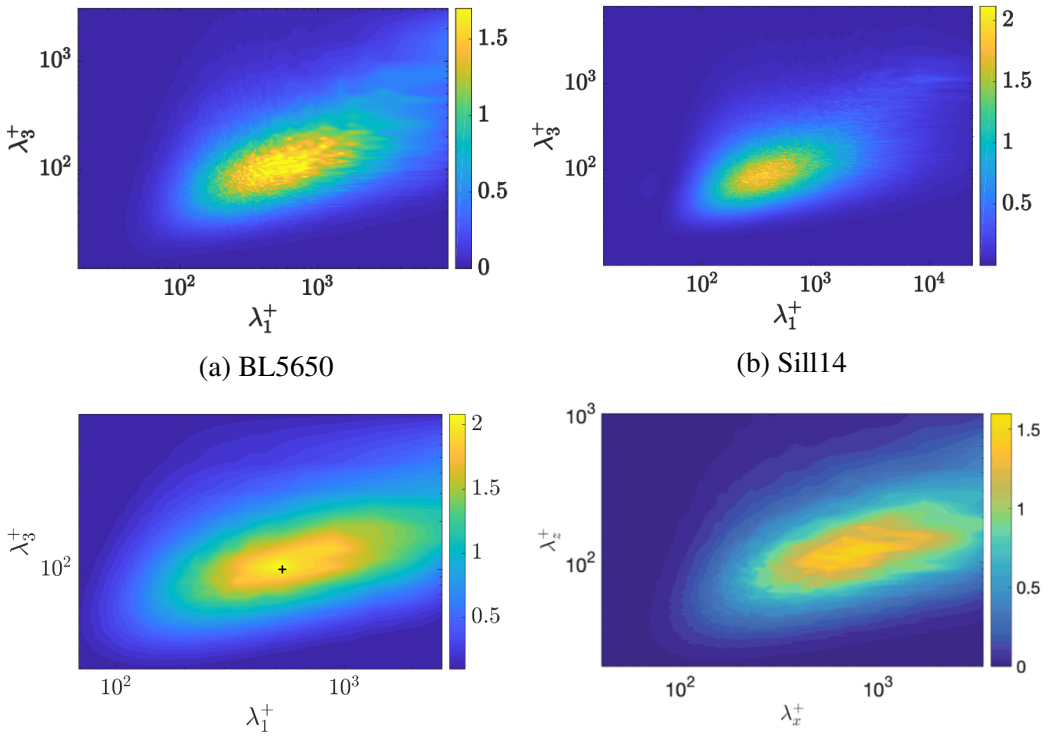

(a) BL5650

(b) Sill14

(c) BL1460

(d) Channel Flow [27].

Figure 5.1: Premultiplied energy spectra $\kappa_1^+\kappa_3^+E_{uu}^+$ at $\xi_2 = 15\delta_\nu$ for (a) BL5650, (b) Sill14, (c) BL1460, (d) Channel flow at an $Re_\tau = 550$ [27]. Reproduced with permission from author. Black cross represents wavelength pair of interest in Sections 5.2-5.5.

integration of contour map of the premultiplied spectra in log of wavelength(s), one obtains the total turbulent kinetic energy. All spectra qualitatively agree, and have a near-wall peak. The larger Reynolds number spectra ($Re_{\delta^*} = 5650$) have a peak at $(\lambda_1^+, \lambda_3^+) \approx (500, 100) \pm (100, 30)$. The streamwise spectra for the lower Reynolds number spectra have a peak approximately at $(\lambda_1^+, \lambda_3^+) \approx (550, 100) \pm (100, 30)$, which is near the peak shown for channel flow at $(\lambda_1^+, \lambda_3^+) \approx (1000, 100)$ [27]. This peak value is associated with key near-wall features, such as the near-wall cycle and the formation of streamwise rollers [64, 68, 69]. The spectra for both boundary layers appear similar to that of the channel flow despite large differences in Re_τ.

The premultiplied spectrum for BL1460 at $\xi_2 = 0.6\delta_{99}$ is shown in Fig. 5.2. The spectrum shows an outer peak at $(\lambda_1/\delta_{99}, \lambda_3/\delta_{99}) \approx (1.7, 1.2) \pm (0.25, 0.13)$. In inner units, this peak corresponds to $(\lambda_1^+, \lambda_3^+) \approx (650, 450) \pm (100, 50)$. For future comparisons with the "inner" wavelength pair, this wavelength pair will be described with inner scaling. It still corresponds to a wave in the outer layer. Note that the

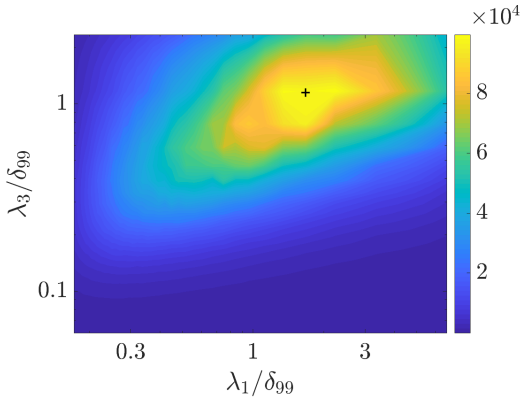

Figure 5.2: Outer-scaled premultiplied energy spectra $\kappa_1\delta_{99}\kappa_3\delta_{99}E^+_{uu}$ for $\xi_2 = 0.6\delta_{99}$ for BL1460. Black cross represents wavelength pair of interest in Sections 5.2-5.5.

change in aspect ratio (λ_1/λ_3) is indicative of changing aspect ratios of turbulent structures.

5.1.2 Temporal spectra

The spatial energy spectra were conducted in a time-averaged setting: independent snapshots of the flow were averaged to compute correlation functions. A similar method (following the method for spectral proper orthogonal decomposition [25, 82]) is also possible to compute temporal statistics, given that the flow is statistically stationary. One first takes a stream of data files and divides it into overlapping blocks (50%) of consecutive datafiles, similar to the procedure used in SPOD. Then, one can conduct Fourier transforms in time for each block to capture the power spectral density. As noted by Schmidt & Colonius (2020), conducting a discrete Fourier transform on the entire signal does not decrease the uncertainty in the energy, and thus this entire procedure is necessary to converge the statistics.

The amount of data necessary to converge these temporal frequencies ends up being much larger than those needed to converge spatial statistics in terms of both storage and simulation run-time. The following analysis is conducted only on BL1460 as it is the smallest Reynolds number case on hand. Due to storage limits, the data files were further down-sampled in the streamwise and spanwise directions by factors of 4 and 2, respectively. Thus, the shortest streamwise and spanwise wavelengths are increased from $(\Delta x^+, \Delta z^+) \approx (18, 12)$ to $(\Delta x^+, \Delta z^+) \approx (72, 24)$.

Following the observation from the spatial spectra (Section 5.1.1), we focus on two specific spatial wavelength pairs $(\lambda_1^+, \lambda_3^+) = (550, 100)$ for the "inner" wave and $(\lambda_1^+, \lambda_3^+) = (650, 450)$ for the "outer" wave and compute the temporal PSD for fixed

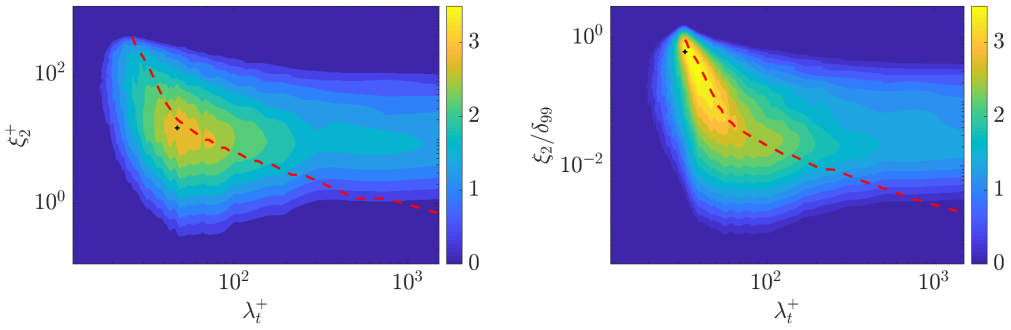

(a) Inner (b) Outer

Figure 5.3: Power spectral density $\log_{10}(E_{uu}^+)$ for $(\lambda_1^+, \lambda_3^+)$ = (a) (550,100) and (b) (650,450). The red dashed line identifies, for the respective c, the location where $u_1^+(\xi_2^+) = c$. The black cross specifies the temporal wavelength of interest in the proceeding sections.

spatial wavelength, shown in Fig. 5.3. Note that the PSD are not premultiplied, in contrast to the spatial spectra of Section 5.1.1. To show more details of the spectra structure, the log of the PSD is taken.

In comparison to the time averaged spatial spectra of Section 5.1.1, the temporal PSD is much more local. For example, the peaks shown in for the spatial spectra often spanned half a decade in inner-normalized streamwise wavelength. In contrast, both Fig. 5.3a and Fig. 5.3b are focused to less than a quarter of a decade in inner-normalized streamwise wavelength.

The PSD of the "inner" spatial wavelength pair $(\lambda_1^+, \lambda_3^+) = (550, 100)$ features a peak at $\lambda_t^+ = 40 - 60$ whereas the "outer" spatial wavelength pair $(\lambda_1^+, \lambda_3^+) = (650, 450)$ features a peak that spans across $\lambda_t^+ \approx 30 - 50$. The "inner" PSD also appears "horizontal" with increasing λ_t^+; for decreasing λ_t^+, there is an inclination towards higher ξ_2^+. This trait is exacerbated in the "outer" spatial frequency and can be understood as being due to the mean streamwise velocity profile. The waves carried by the mean flow travel at a wave speed $c^+ = \lambda_1^+/\lambda_t^+$ centered at the mean flow location. Hence, the energy, for different frequencies, is expected to be centered at $u^+(\xi_2^+) = c^+ = \lambda_1^+/\lambda_t^+$. A red dashed line is shown on each contour indicating the locations where $u^+(\xi_2^+) = c^+ = \lambda_1^+/\lambda_t^+$. For linear stability analysis, this location is known as the critical layer, and it will be investigated more thoroughly in Section 5.4. This concept is helpful for explaining the inclination and centering of the peak, but appears to weaken in agreement in the outer layer.

To specifically study wavelengths characteristic of "inner" and "outer" layer behavior,

in Section 5.2, we shall restrict ourselves to the study of the wavelength triplets $(\lambda_1^+, \lambda_3^+, \lambda_t^+) = (550, 100, 50)$ and $(\lambda_1^+, \lambda_3^+, \lambda_t^+) = (650, 450, 33)$.

5.2 Resolvent analysis

This section describes the different formulations of the resolvent operator in Cartesian and parallelized coordinates. First, a brief introduction and overview is provided for resolvent analysis. Then, the 1D resolvent is provided specifically for boundary layer flow.

5.2.1 Broad overview

The Navier-Stokes equation's chief difficulty remains in interpreting and understanding the effects of the nonlinear terms. However, it is apparent that several key turbulent mechanisms are driven by linear processes [26, 83–86], and the study of the linearized Navier-Stokes operator is crucial to fully understanding self-sustaining cycles within turbulence. The key tool for this study is fully codified in McKeon & Sharma (2010) and is known as resolvent analysis or input/output analysis. Similar ideas existed in [85], but were not fully generalized. This method has been widely applied to various flows, such as rough wall boundary layer flow [87], channel and pipe flows [88], and turbulent jets [89]. Resolvent analysis treats the nonlinear terms in the Navier-Stokes equations as external forcing terms and the remaining variables as response terms. Similar to the linear stability studies for transition, resolvent analysis is conducted in the frequency domain and finds forcings that correspond to the most amplified response modes. Consequently, a key requirement for the application of resolvent analysis is statistical stationarity.

Provided a state vector $\mathbf{g} = [u_1, u_2, u_3, p/\rho]^\intercal$, where $^\intercal$ denotes transpose, one can compute the Reynolds decomposition $\mathbf{g} = \overline{\mathbf{g}} + \mathbf{g}'$. Given statistical stationarity, one can then conduct a Fourier transform in time and any other homogeneous direction. Then, one can recast the Navier-Stokes equations as

$$\hat{\mathbf{g}}' = \underbrace{\mathbf{C}(i\omega\mathbf{I} - L(\overline{\mathbf{g}}))^{-1}\mathbf{B}}_{\mathbf{R}}\hat{\mathbf{f}} = \mathbf{R}\hat{\mathbf{f}} \tag{5.3}$$

where L is the Fourier transformed linearized Navier-Stokes operator based on the mean state vector $\overline{\mathbf{g}}$, $\hat{(\cdot)}$ denotes variables in the transformed domain, $i^2 = -1$, $\hat{\mathbf{g}}$ is the Fourier transform of $\mathbf{g}$, $\hat{\mathbf{f}} = [\hat{f_1}, \hat{f_2}, \hat{f_3}]$ is the Fourier transformed nonlinear terms, treated as external forcing, and $\mathbf{B}$ and $\mathbf{C}$ are operators that restrict the output and input quantities, e.g. enforcing that the forcing is only present in the momentum

equations and not the continuity equation. One should note that the linearized Navier-Stokes operator is dependent on an *a priori* mean profile, obtained through experiment, simulation, or empirical fits. Resolvent analysis then proceeds to study the linear properties of **R** numerically, via the singular value decomposition (SVD), described in Section 5.2.4.

The complexity in studying **R** is dramatically reduced with additional homogeneous directions. Each subsequent Fourier transform allows one to more specifically focus the study of R for turbulent motions of specific aspect ratios and sizes. The benefits extend numerically as well, since the numerical cost of conducting the SVD is greatly reduced.

5.2.2 1D Cartesian resolvent operator

We now restrict the resolvent analysis to the 1D case for boundary layers. Classical 1D resolvent analysis [87, 90] utilizes two key approximations to simplify the governing equations:

1. The flow is statistically stationary and is statistically homogeneous in the spanwise (x_3) and, more critically, the streamwise (x_1) directions.
2. The base flow is parallel in the streamwise direction and has negligible $\overline{u}_2$.

Specifically for the boundary layer, the state variable **g** can be decomposed using Fourier transforms in the two homogeneous directions and time

$$g(x_1, x_2, x_3, t) = \iiint \hat{\mathbf{g}}(x_2; \kappa_1, \kappa_3, \omega) e^{i(\kappa_1 x_1 + \kappa_3 x_3 - \omega t)} d\kappa_1 d\kappa_3 d\omega \tag{5.4}$$

where, κ_1 and κ_3 denote the streamwise and spanwise wavenumbers, and ω is the temporal wavenumber, respectively. In this way, the current equations are equivalent for both the (assumed parallel) boundary layer and channel flow.

Given the previous streamwise parallel approximation, the boundary layer base flow can be written as $\bar{\mathbf{g}} \approx [\overline{u}_1(x_2), 0, 0, \overline{p/\rho}(x_2)]^\intercal$. This base flow corresponds to $(\kappa_1, \kappa_3, \omega) = (0, 0, 0)$.

The governing equations can be rewritten for each $(\kappa_1, \kappa_3, \omega)$ as

$$i\kappa_1\hat{u}_1 + \frac{\partial \hat{u}_2}{\partial x_2} + i\kappa_3\hat{u}_3 = 0 \tag{5.5}$$

$$\left[-i\omega + L_c\right]\hat{u}_1 + \frac{d\overline{u}_1}{dx_2}\hat{u}_2 + i\kappa_1\hat{p}/\rho = \hat{f}_1 \tag{5.6}$$

$$\left[-i\omega + L_c\right]\hat{u}_2 + \frac{1}{\rho}\frac{\partial \hat{p}}{\partial x_2} = \hat{f}_2 \tag{5.7}$$

$$\left[-i\omega + L_c\right]\hat{u}_3 + i\kappa_3\hat{p}/\rho = \hat{f}_3 \tag{5.8}$$

where

$$L_c[\hat{u}] = \left[-i\omega + i\kappa_1\overline{u}_1 + \nu\left(\kappa_1^2 + \kappa_3^2 - \frac{\partial^2}{\partial x_2^2}\right)\right]\hat{u} \tag{5.9}$$

and $\hat{\mathbf{f}}$ contains the Fourier transformed non-linear terms. The Fourier transformed fluctuating component can be expressed by

$$\mathbf{g} = \mathbf{R}_c \begin{pmatrix} 0 \\ \hat{f}_1 \\ \hat{f}_2 \\ \hat{f}_3 \end{pmatrix} \tag{5.10}$$

where

$$\mathbf{R}_c{}^{-1} = \begin{pmatrix} i\kappa_1 & \partial_{x_2} & i\kappa_3 & 0 \\ L_c & \partial_{x_2}\overline{u}_1 & 0 & i\kappa_1/\rho \\ 0 & L_c & 0 & \frac{1}{\rho}\partial_{x_2} \\ 0 & 0 & L_c & i\kappa_3/\rho \end{pmatrix} \tag{5.11}$$

$\mathbf{R}_c = \mathbf{R}_c(x_2; \kappa_1, \kappa_3, \omega)$ is the 1D resolvent operator and exists provided the linearized Navier-Stokes equations are non-singular. For each chosen set of spatio-temporal frequencies $(\kappa_1, \kappa_3, \omega)$, a linear analysis of the resolvent operator describes the most amplified modes.

There are several limits to this analysis. The 1D boundary layer resolvent analysis broadly imposes streamwise periodicity on the flow while also assuming statistical stationarity. Although the flow is only weakly streamwise inhomogeneous, every DNS of a boundary layer with imposed streamwise periodic boundary conditions in the Cartesian coordinate system has always been non-stationary. Specifically, it has been noted that for temporally developing boundary layers, the boundary layer growth was enough to significantly reduce statistical convergence of many of the key profiles [35].

Additionally, the neglecting of the streamwise growth of the boundary layer in governing equations is equivalent to assuming that turbulent fluctuations throughout the boundary layer remain at approximately the same wall-normal height. However, the rms profiles of the boundary layer scale with δ_{99} in the wake and so, consequently, the current 1D resolvent analysis may not be suitable for prediction of turbulent structures located in the outer region.

Finally, the removal of the mean wall-normal velocity is consistent with streamwise periodicity. The existence of a mean-wall-normal velocity profile implies, via continuity, streamwise inhomogeneity of the mean streamwise velocity profile. However, this points out yet another limitation of 1D boundary layer resolvent analysis. Especially in the wake region where turbulent intensities are sufficiently weaker, transport by the mean wall-normal velocity might eventually dominate over both the Reynolds stresses and viscous terms in the wall-normal momentum equation. Neglecting the wall-normal profile might result in the loss of crucial information on the behavior of turbulent transport.

Throughout this chapter, the resolvent operator $\mathbf{R}_c$ associated with the previous analysis will be referred to as the Cartesian resolvent operator. Similarly, the resulting response and forcing modes will be referred to as the Cartesian response and forcing modes.

5.2.3 Resolvent analysis with wall-normal rescaling

The wall-normal rescaling introduced in Chapter 2 defines a new set of equations that are statistically homogeneous in the streamwise direction as well as statistically stationary. The agreement of the one-point and two-point statistics suggests that the previous 1D resolvent framework can be improved upon by adopting this wall-normal rescaling. Specifically, in the rescaled coordinate system, resolvent analysis can finally impose streamwise periodic boundary conditions more directly. Furthermore, the neglecting of the mean wall-normal velocity profile can be relaxed.

Applying a Fourier transform in time and in the streamwise and spanwise directions to the rescaled governing equations (Eq. 2.16-2.17), one obtains the following equations

$$i\kappa_1\hat{u}_1 + \frac{\partial \hat{u}_2}{\partial \xi_2} + i\kappa_3\hat{u}_3 - \frac{q'}{q}\xi_2\frac{\partial \hat{u}_1}{\partial \xi_2} = 0 \tag{5.12}$$

$$\left[-i\omega + L_p - \frac{q'}{q}\xi_2\frac{d\overline{u}_1}{d\xi_2}\right]\hat{u}_1 + \frac{d\overline{u}_1}{d\xi_2}\hat{u}_2 + i\kappa_1\hat{p}/\rho = \hat{f}_1 \tag{5.13}$$

$$-\frac{q'}{q}\xi_2\frac{d\overline{u}_2}{d\xi_2}\hat{u}_1 + \left[-i\omega + L_p + \frac{d\overline{u}_2}{d\xi_2}\right]\hat{u}_2 + \frac{1}{\rho}\frac{\partial \hat{p}}{\partial \xi_2} = \hat{f}_2 \tag{5.14}$$

$$\left[-i\omega + L_p\right]\hat{u}_3 + i\kappa_3\hat{p}/\rho = \hat{f}_3 \tag{5.15}$$

where

$$L_p[\hat{u}] = \left[-i\omega + i\kappa_1\overline{u}_1 + \nu\left(\kappa_1^2 + \kappa_3^2 - \frac{\partial^2}{\partial \xi_2^2}\right)\right]\hat{u} + \overline{u}_2\frac{\partial \hat{u}}{\partial \xi_2} - \frac{q'}{q}\xi\overline{u}_1\frac{\partial \hat{u}}{\partial \xi_2} \tag{5.16}$$

The governing equations can be recast into

$$\hat{\mathbf{g}}(\xi_2, \kappa_1, \kappa_3, \omega) = \mathbf{R}_p(\kappa_1, \kappa_3, \omega)\hat{\mathbf{f}}(\xi_2, \kappa_1, \kappa_3, \omega) \tag{5.17}$$

$$\mathbf{R}_p{}^{-1} = \begin{pmatrix} i\kappa_1 - \frac{q'}{q}\xi_2\partial_{\xi_2} & \partial_{\xi_2} & i\kappa_3 & 0 \\ L_p - \frac{q'}{q}\xi_2\partial_{\xi_2}(\overline{u}_1) & \partial_{\xi_2}\overline{u}_1 & 0 & i\kappa_1/\rho \\ -\frac{q'}{q}\xi_2\partial_{\xi_2}(\overline{u}_2) & L_p + \partial_{\xi_2}\overline{u}_2 & 0 & \frac{1}{\rho}\partial_{\xi_2} \\ 0 & 0 & L_p & i\kappa_3/\rho \end{pmatrix} \tag{5.18}$$

where $\mathbf{R}_p$ is now the resolvent operator pertaining to the parallelized boundary layer.

Throughout this chapter, the resolvent operator $\mathbf{R}_p$ associated with the rescaled governing equation will be referred to as the parallelized resolvent operator. Similarly, the resulting response and forcing modes will be referred to as the parallelized response and forcing modes.

The rescaled governing equations effectively provide new terms that capture the streamwise growth of the mean and fluctuations. In the Cartesian 1D resolvent analysis, this growth can also be understood as being bundled into the forcing term. In other words, a portion of the forcing term is being captured by the linearized rescaling terms added in R_p.

Alternative methods of modeling the forcing term also exist, specifically via the addition of an eddy-viscosity term. It has been proven to be successful for channel flows [31, 91, 92] and in jets [29, 93]. There are various difficulties associated

either with interpretation of the forcing, or even the specific eddy-viscosity model chosen. In the analysis by Pickering *et al.* (2021), the response modes obtained from using resolvent analysis using different eddy-viscosity models, either using a RANS model or an "SPOD-optimized" model, featured sharp differences. For a full discussion on the impact of eddy-viscosity on resolvent analysis, the reader is referred to [91, 93].

5.2.4 Singular value decomposition

Regardless of the choice of $\mathbf{R}_c$ or $\mathbf{R}_p$, the overall goal of resolvent analysis is to apply a Schmidt decomposition to the resolvent operator to find the most energetic modes. The selected norm is the constant kinetic energy norm, provided by

$$< \mathbf{g}, \mathbf{g} >= \int_0^\infty u_i^\dagger u_i dx_2 \tag{5.19}$$

We then proceed forward with the Schmidt decomposition

$$\mathbf{R} = \sum_{j=1}^{\infty} \psi_j \sigma_j \phi_j^\dagger \tag{5.20}$$

where † denotes conjugate transpose, and ψ_j and ϕ are the left and right singular vectors, respectively, and form an orthonormal basis. They are also known as the response and forcing modes and will be referred to as such hereafter. The choice of basis set is unique up to a unitary complex factor.

5.2.5 Numerical set-up

Resolvent analysis operates on discretized governing equations on a grid with both flow velocities and pressure evaluated at collocated points in the wall-normal direction. The overall code was adapted from [94] and executed in MATLAB.

To construct the resolvent operators, discrete numerical profiles were taken from Orlu *et al.* (2013) and from Chapter 2 for $Re_{\delta^*} = 1460$, where the boundary layer growth term is expected to be largest. An exhaustive study of all potential waves is not particularly meaningful if the waves are not energetic in the real flow. The analysis of the spatial and temporal spectra conducted in Sections 5.1.1-5.1.2 allows us to focus our study on energetic waves located in the inner and outer layers. Specifically, we will now focus on two waves corresponding to two specific sets of spatio-temporal wavelengths: $(\lambda_1^+, \lambda_3^+, \lambda_t^+) \approx (550, 100, 50)$ and $(\lambda_1^+, \lambda_3^+, \lambda_t^+) \approx (650, 450, 33)$, referred to as the "inner" and "outer" waves, respectively. The term

"waves" is chosen to specifically differentiate them from the modes of the resolvent operator or SPOD. The term is also accurate since each set of spatio-temporal wavelengths describes a traveling wave in the streamwise direction and a standing wave in the spanwise direction.

The corresponding wave speeds are approximately $c^+ \approx 10, 20$ or $c/u_{1,\infty} \approx 0.5, 0.95$ for the "inner" and "outer" waves, respectively. These "inner" and "outer" phase speeds approximately agree with previously studied phase speeds in Bae *et al.* (2020) ($c/u_{1,\infty} = 0.5, 0.98$). Bae *et al.* (2020) had identified that at these particular phase speeds, the respective inner and outer response modes had mode shapes and heights with inner and outer scalings, respectively.

In Section 5.1.2, it was noted that the peak location of the energy spectra approximately follows the curve $\xi_2 = \overline{u}_1^{-1}(\omega/\kappa_1)$. One should expect then that the peak in the response modes will align with the peaks of the energy spectra. This was noted to coincide with the classical definition of the critical layer [95]. In linear stability theory, the transitional critical layer is the wall-normal location where the inviscid parallel flow equations are singular with respect to a small perturbation. One can very classically determine from the governing equations exactly where the critical layer will occur. In this layer, viscosity is often restored and solutions are often found centering around these critical points.

The critical layer for resolvent analysis is typically described as the wall-normal location where the response mode is most amplified. It was shown in McKeon *et al.* (2010), that the turbulent critical layer of the response mode of the 1D Cartesian resolvent operator exactly coincides with the location of the classically defined critical layer, e.g. in Cartesian coordinates, $x_2 = \overline{u}_1^{-1}(\omega/\kappa_1)$. This result can be observed through inspection of L_c. If one assumes the viscous terms are largely negligible throughout the outer layer, then at $x_2 = \overline{u}_1^{-1}(\omega/\kappa_1)$, the magnitude of L_c vanishes. Consequently, R_c will have high resolvent norm.

The operator L_p is not nearly so tractable. The additional term $q_0'/q_0\xi_2\partial\hat{u}_i/\partial\xi_2$ is active away from the wall and the derivative term requires some prior knowledge of the shape of $\hat{u}_i$ to find where the magnitude of L_p is minimized. It is therefore difficult, from a purely mathematical standpoint, to explicitly predict where the critical layer lies for the new operator R_p. However, it will be shown in Section 5.4 that provided one has already computed the response mode of R_c, one can predict the peak location of the response mode of R_p.

5.2.6 Comparisons between coordinate systems

It was noted earlier in Sec. 5.1.1 that the Fourier transforms conducted in the 1D Cartesian coordinate system are different from those conducted in the 1D rescaled coordinate system. Specifically in the coordinate system of R_c, Fourier transforms of the velocity components and pressure are conducted at *constant* x_2. On the other hand, in the coordinate system of R_p, Fourier transforms are conducted at *constant* ξ_2. Consequently, the waves specified in the previous subsection are theoretically not the same waves in Cartesian and rescaled coordinates: in the Cartesian coordinates, these waves travel at a constant wall-normal height x_2, and in rescaled coordinates, these waves travel at constant $x_2 q_0/q$, or along coordinate lines that follow the growth of the boundary layer.

The goal of this section is to estimate the difference between the waves in the two different coordinate systems. Put differently, our goal is to investigate how Fourier transforms differ with respect to constant $\xi_2 = h$ from those with respect to constant $x_2 = h$.

From a geometric perspective, the inclination angle of the boundary layer can be estimated by $\tan^{-1}(q_0'/q_0 x_2)$. At the very edge of the boundary layer, the inclination angle is less than $1°$. In comparison, wall-attached turbulent structures have inclination angles of about $45°$ [70]. From this perspective, it is not expected that the spectra are influenced by conducting Fourier transforms at constant ξ_2 vs. constant x_2.

To illustrate this, we will consider Fourier transforms of the same arbitrary turbulent quantity s of a growing boundary layer with a streamwise domain of length L_x, centered around $x_0 = 0$, for either $x_2 = h$ or $\xi_2 = h$.

First, the “Cartesian" Fourier transform for constant $x_2 = h$ is given by

$$\hat{s}^c(\kappa_1, x_3, t) = \frac{1}{L_x}\int_{-L_x/2}^{L_x/2} s(x_1, x_2, x_3, t)|_{x_2=h} e^{-i\kappa_1 x_1} dx_1 \tag{5.21}$$

The corresponding “parallel" Fourier transform for constant $\xi_2 = h$ is given by

$$\hat{s}^p(\kappa_1, \xi_3, t)|_{\xi_2=h} = \frac{1}{L_x}\int_{-L_x/2}^{L_x/2} s(\xi_1, \xi_2, \xi_3, t)|_{\xi_2=h} e^{-i\kappa_1 \xi_1} d\xi_1 \tag{5.22}$$

The dependencies on spanwise and time coordinates will be dropped from this point onwards. Our goal is then to compute the difference $\hat{s}^c - \hat{s}^p$. To do so, we transform

the coordinates of Eq. 5.22 back to Cartesian coordinates to obtain

$$\hat{s}^r(\kappa_1) = \frac{1}{L_x}\int_{-L_x/2}^{L_x/2} s(x_1, x_2)|_{x_2=hq(x_1)/q_0} e^{-i\kappa_1 x_1} dx_1 \tag{5.23}$$

Conducting a first order Taylor expansion of $x_2 = hq(x_1)/q_0$ in x_1 centered at $x_1 = x_0$ gives that $s(x_1, x_2)|_{x_2=hq/q_0} \approx s(x_1, h + hx_1 q_0'/q_0)$. One can then conduct a first order Taylor expansion of $s(x_1, h + hq_0'/q_0)$ centered at (x_1, h). The combination of both Taylor expansions gives that

$$\begin{aligned} s(x_1, x_2)|_{x_2=hq(x_1)/q_0} &\approx s(x_1, x_2 = h + hx_1 q_0'/q_0) \approx \\ &s(x_1, h) + x_1 h \frac{q_0'}{q_0}\left(\frac{\partial s}{\partial x_2}\right)\Big|_{x_2=h} \end{aligned} \tag{5.24}$$

Thus, the difference between the Fourier transforms is approximated by

$$\hat{s}^p - \hat{s}^c \approx \frac{h}{L_x}\frac{q_0'}{q_0}\int_{-L_x/2}^{L_x/2} x_1 \frac{\partial s}{\partial x_2}\Big|_{x_2=h} e^{-i\kappa_1 x_1} dx_1 \tag{5.25}$$

The most convenient method to investigate the relative impact of this difference is to evaluate $\langle(\hat{s}^p - \hat{s}^c)\hat{s}^{c,\dagger}\rangle_{\kappa_1,\xi_3,t}$ and compare it with $\langle\hat{s}^c\hat{s}^{c,\dagger}\rangle_{\kappa_1,\xi_3,t}$ for fixed $x_2 = h$. From Parseval's theorem, this ratio is equivalent to the autocorrelation "error" term discussed in Chapter 4! In Chapter 4, the error term was found to be several orders of magnitude smaller than the autocorrelation function. The same conclusions from Chapter 4 also apply here: due to the very slow growth of the boundary layer, the difference between Fourier transforms is largely negligible.

For the remainder of this chapter, we will directly compare the waves from the Cartesian and rescaled coordinate systems, under the assumption that the differences between the two systems are minute. This assumption will also carry over to the physical interpretation of the modes: because the inclination angle is negligibly small, the discovered linear mechanisms ("lift-up" and "Orr", to be described in Section 5.5.3) in the rescaled coordinate system will be identified with their Cartesian analogue.

5.3 Resolvent analysis results

In this section, the singular spectra and mode shapes for $\mathbf{R}_c$ and $\mathbf{R}_p$ are compared. Special considerations are given to data origin and wall-normal velocity profile.

5.3.1 Impact of numerical source: $\overline{u}_1$ profile

As described in Section 5.2.3, the resolvent analysis requires a mean velocity profile $\overline{u}_1$. The singular value spectra of the parallelized resolvent operator ($\mathbf{R}_p$) for the

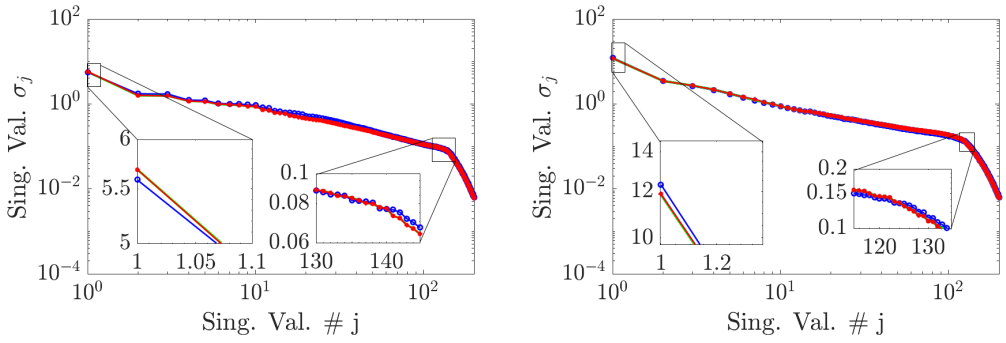

(a) Inner wave (b) Outer wave

Figure 5.4: Singular value spectra of R_p for (a) inner and (b) outer waves at $Re_{\delta^*} = 1460$. Colors: (black) [59], (green) [39] and (red) $\mathbf{R}_{p,fic}$

inner and outer waves are shown in Figs. 5.4a-5.4b, respectively, using the growing boundary layer dataset [39] and the periodic boundary layer dataset (Chapter 2). Several observations can be drawn. First, the singular spectra for different mean velocity profiles are virtually identical. Stated differently the choice of mean profile (either from [39] or BL1460 from Chapter 2), has negligible impact on the singular spectra. The difference in magnitude of the first mode is within 2% for the two mean profiles, and for higher modes, the difference in magnitude only marginally increases to 3%. This is expected since the shape factors between the two mean velocity profiles were within 3% to begin with. Because both profiles were interpolated onto the same grid, it is only expected that the spectra should be similar.

The different velocity components of the dominant resolvent modes of $\mathbf{R}_p$ are shown in Figs. 5.5-5.6 for the inner and outer waves, respectively. It is clear that for both the streamwise and spanwise components, the dominant resolvent modes are nearly indistinguishable. A discrepancy of $\sim 6\%$ appears in the wall-normal component, specifically near the peak. This is somewhat understandable since the mean velocity profiles featured differences in shape factors of up to 1%. It was also shown in Chapter 2 that the relative differences in $\overline{u}_2$ between growing and parallel datasets is at most 5%. The peak location and mode envelope shape appear geometrically similar. Furthermore, the streamwise component is approximately 5x in magnitude compared to the wall-normal component. Based on continuity, a $\sim 6\%$ relative difference in $\hat{u}_2$ results in at most a 1% relative difference in $\hat{u}_1$.

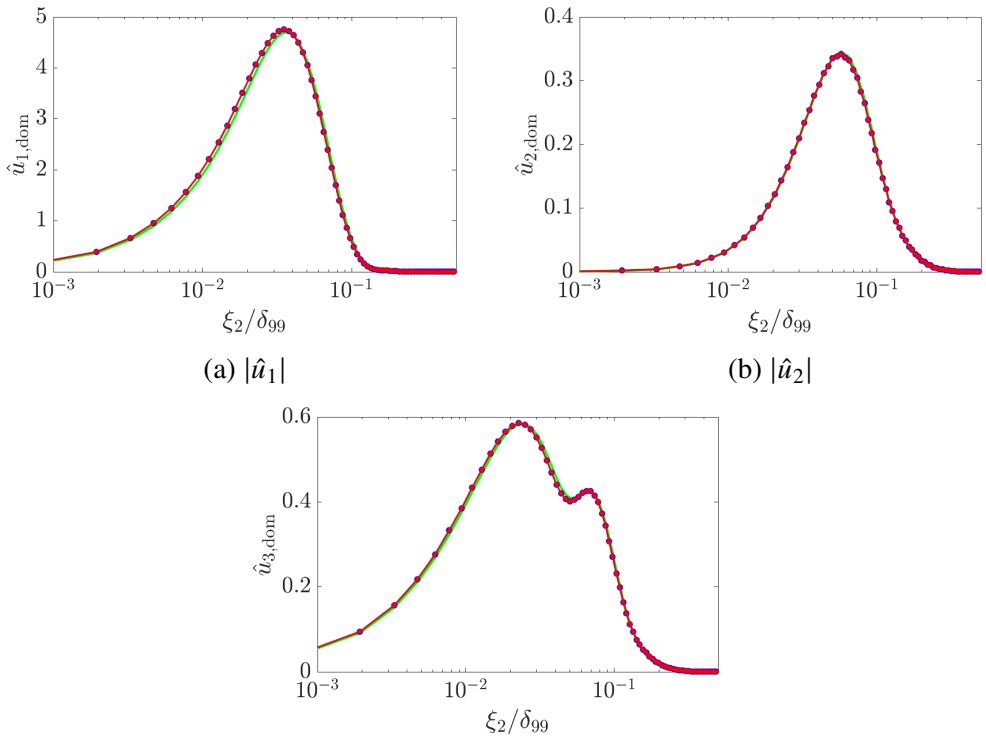

(a) $|\hat{u}_1|$ (b) $|\hat{u}_2|$

(c) $|\hat{u}_3|$

Figure 5.5: Dominant mode components (a) $|\hat{u}_1|$, (b) $|\hat{u}_2|$, and (c) $|\hat{u}_3|$ for the inner wave at $Re_{\delta^*} = 1460$. Colors: (black) [59], (green) [39] and (red) $\mathbf{R}_{p,fic}$.

5.3.2 Impact of numerical source: $\overline{u}_2$ profile

The resolvent analysis for the homogenized boundary layer also requires a mean wall-normal velocity profile ($\overline{u}_2$). Unfortunately, the mean profiles extracted from growing boundary layer dataset [39] do not satisfy the mean rescaled continuity reproduced in Eq. 5.26.

$$\frac{\partial \overline{u}_2}{\partial \xi_2} = \frac{q'}{q}\xi_2 \frac{\partial \overline{u}_1}{\partial \xi_2} \tag{5.26}$$

To investigate whether the source of the mean wall-normal velocity profile has any impact on the computation of singular spectra and dominant response modes of $\mathbf{R}_p$, one can construct a fictitious $\overline{u}_2^{fic}$ from the streamwise velocity profile via

$$\overline{u}_2^{fic} = \int_0^{\xi_2} \xi_2^* \frac{q'}{q} \frac{\partial \overline{u}_1}{\partial \xi_2^*} d\xi_2^* \tag{5.27}$$

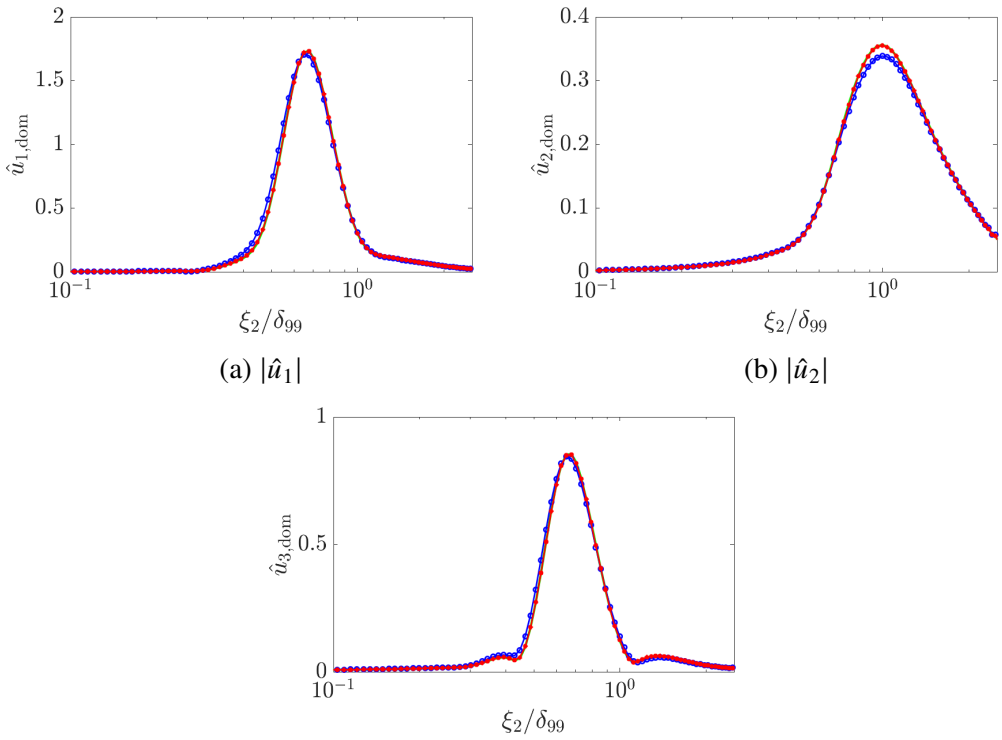

(a) $|\hat{u}_1|$ (b) $|\hat{u}_2|$

(c) $|\hat{u}_3|$

Figure 5.6: Dominant mode components (a) $|\hat{u}_1|$, (b) $|\hat{u}_2|$, and (c) $|\hat{u}_3|$ for the outer wave at $Re_{\delta^*} = 1460$. Colors: (black) [59], (green) [39] and (red) $\mathbf{R}_{p,fic}$.

One can replace the mean wall-normal velocity profile from [39] with this fictitious mean wall-normal velocity profile and investigate the impact these profiles have on $\mathbf{R}_p$. We denote the operator $\mathbf{R}_p$ with the fictitious $\overline{u}_2$ as $\mathbf{R}_{p,fic}$.

The singular spectra of $\mathbf{R}_{p,fic.}$ are shown in Fig. 5.4. The effects of changing $\overline{u}_2$ are minimal, with relative differences being at most 1% for the larger singular values. The dominant modes for outer and inner waves are shown in Fig. 5.6 and Fig. 5.5, respectively. Once again, there are virtually no differences for each component with exception of the wall-normal mode. In summary, the resolvent singular spectra and response modes are not sensitive to the original source of the wall-normal velocity profile.

5.3.3 Mode shapes

The envelope (magnitude) of the dominant mode for the inner wave (Fig. 5.5) has a distinctive shape. There is a peak in the magnitude near the wall, and the streamwise component is at least an order of magnitude larger than both the wall-normal and spanwise components. The peak location of the predicted dominant response mode

($\xi_2^+ \approx 15, \xi_2 \approx 0.04\delta_{99}$) is within 5% of the extracted peak location of the temporal PSD of Section 5.1 ($\xi_2^+ \approx 20, \xi_2 \approx 0.05\delta_{99}$).

Furthermore, as anticipated by [38, 90, 96], the inner wave mode features near-wall scaling. The $\hat{u}_1, \hat{u}_3$ components of the dominant mode have a linear envelope in the near wall region $y^+ < 5$. On the other hand, the envelope of the $\hat{u}_2$ component is parabolic near the wall. This mirrors the behavior of $\overline{u}_1$ and $\overline{u}_2$, where $\overline{u}_1$ is approximately linear near the wall and $\overline{u}_2$ is approximately parabolic. In fact, both sets of behaviors are caused by continuity.

The envelope for the outer wave (Fig. 5.6) is closer to a Gaussian, and as noted by [96], resolvent modes ten to feature an expected Gaussian envelope. As expected, the magnitude peak is in the outer layer. Again, the peak location of the predicted response mode ($\xi_2 \approx 0.6\delta_{99}$) is within 10% of the extracted peak location of the temporal PSD of Section 5.1 ($\xi_2 \approx 0.7\delta_{99}$).

5.3.4 $\mathbf{R}_c$ vs $\mathbf{R}_p$

The singular spectra of $\mathbf{R}_c$ and $\mathbf{R}_p$ are now compared in Fig. 5.7. It was shown in the previous subsection that the resolvent operator $\mathbf{R}_p$ had singular spectra with a larger, dominant singular value. The singular spectra for both inner and outer waves show that the magnitude of the dominant mode is larger than that of the other singular values by almost an order of magnitude. This trait is shared by both $\mathbf{R}_c$ and $\mathbf{R}_p$. Both resolvent operators are low-rank and the bulk of the predicted turbulent response to this particular spatio-temporal frequency will be dominated by the first mode.

The singular spectra for both inner and outer waves also feature several important differences. The singular value of the dominant mode for the outer wave spectra are of similar orders of magnitude, whereas for the inner wave spectra, the singular values overlap. Finally, for the highest singular response modes, the singular value drop-offs overlap. For both the inner and outer waves, this overlap occurs at mode number 130 which approximately corresponds to the number of grid points in the wall-normal direction.

The components of the dominant response mode of $\mathbf{R}_c$ and $\mathbf{R}_p$ are shown in Figs. 5.8 and 5.9. They are all virtually indistinguishable and share the same inner layer peak. For the inner wave, the additions in $\mathbf{R}_p$ (the wall-normal velocity profile and the source terms) are not large enough in magnitude to affect the dominant response mode. This is expected; it was shown in Chapter 2 that the source terms have

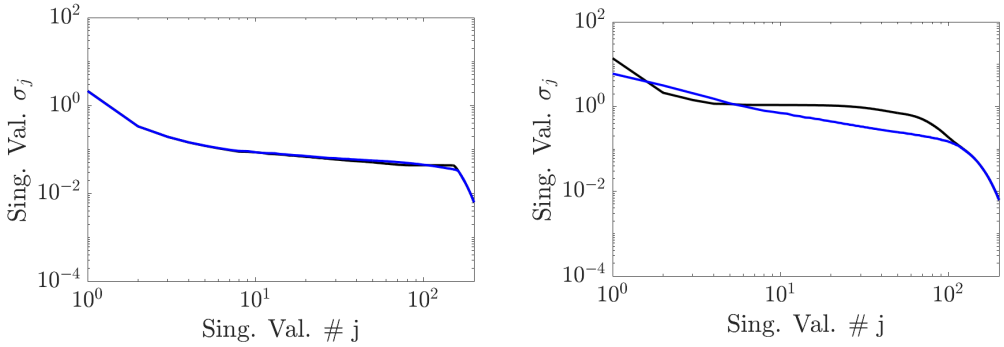

(a) Singular spectra for the inner wave

(b) Singular spectra for the outer wave

Figure 5.7: Singular value spectra of the resolvent operators for (a) inner and (b) outer frequencies at $Re_{\delta^*} = 1460$. Colors: (black) $\mathbf{R}_c$, (black) $\mathbf{R}_p$.

negligible impact on the mean velocity profiles in the near-wall region.

The source terms added in $\mathbf{R}_p$ have a non-negligible impact on the mode location and width. Again, this is consistent with the results shown in Chapter 2, which showed that in the outer layer, the source terms have significant impacts on the mean velocity profiles. The mode location has shifted from the Cartesian wall-normal peak location $\xi_2 = 0.91\delta_{99}$ to a new location $\xi_2 = 0.73\delta_{99}$.

This shift can be interpreted as "suction" due to the wall-normal rescaling. The additional source term in the rescaled momentum equations acts to counter wall-normal advection. In the mean streamwise momentum equation, the source term shares the same sign with the viscous terms and is also demonstrably non-negative. It consequently draws flow towards the wall, keeping the boundary layer statistically stationary.

5.3.5 Impact of $\overline{u}_2$

Given that the transpiration velocity is many orders of magnitude smaller than the free-stream velocity ($u_{2,\infty} \approx 10^{-3} u_{1,\infty}$), one might wonder if the transpiration velocity has any effect on the operators. To explore this, we denote the operators $\mathbf{R}_{c,+v}$ and $\mathbf{R}_{p,-v}$ as operators $\mathbf{R}_c$ and $\mathbf{R}_p$ with the wall-normal velocity included and excluded, respectively.

First, the singular spectra for the inner wave are shown in Fig. 5.10a. The inclusion/exclusion of the wall-normal velocity profile does not affect the singular spectra of $\mathbf{R}_c$ and $\mathbf{R}_p$. The differences, especially in the dominant mode, are smaller than the differences caused by different datasets. Figure 5.10b shows the singular spectra for the outer wave. The relative differences in the first mode energy value are within

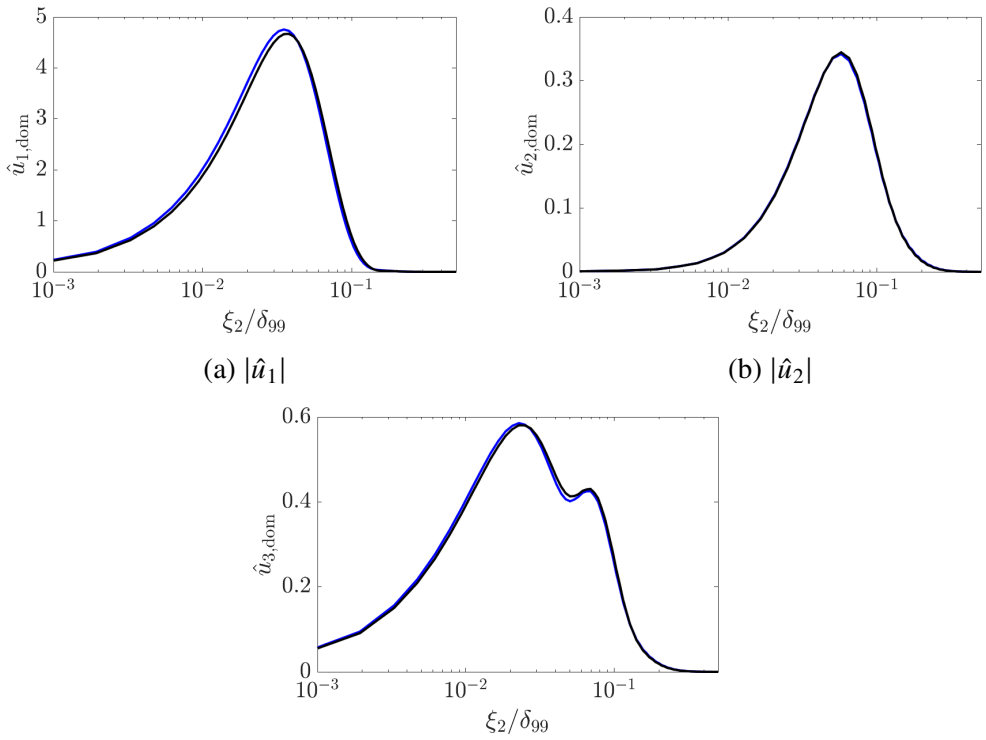

(a) $|\hat{u}_1|$ (b) $|\hat{u}_2|$

(c) $|\hat{u}_3|$

Figure 5.8: Dominant mode components (a) $|\hat{u}_1|$, (b) $|\hat{u}_2|$, and (c) $|\hat{u}_3|$ for the inner wave at $Re_{\delta^*} = 1460$. Colors: (black) $\mathbf{R}_c$, (black) $\mathbf{R}_p$.

1%. Across the spectrum, $\mathbf{R}_p$ and $\mathbf{R}_{p,-v}$ have singular values within 5% of each other. The Cartesian operators ($\mathbf{R}_c$ and $\mathbf{R}_{c,+v}$) only have relative differences of at most 1% in the first mode.

We now investigate the outer wave dominant mode behavior. The components of the dominant response modes are shown in Fig. 5.11. All modes maintain a Gaussian-like envelope. The impact of the mean wall-normal velocity term is much more visible. The peak location for the streamwise component has shifted for both $\mathbf{R}_{p,-v}$ and $\mathbf{R}_{c,+v}$ and there is even a difference in shape for $\mathbf{R}_{c,+v}$. Consistent with the singular spectra, the differences between $\mathbf{R}_p$ and $\mathbf{R}_{p,-v}$ are much smaller than those between $\mathbf{R}_c$ and $\mathbf{R}_{c,+v}$. The addition of $\overline{u}_2$ is correlated with shifting the peak towards the free-stream, and conversely, removing $\overline{u}_2$ is correlated with shifting the peak location closer to the wall. Finally, the free-stream behavior of $\mathbf{R}_{c,+v}$ mimics that of $\mathbf{R}_p$. On the other hand, the wall-normal component apparently drops in magnitude by at least 10%, but does not feature a shift in peak location.

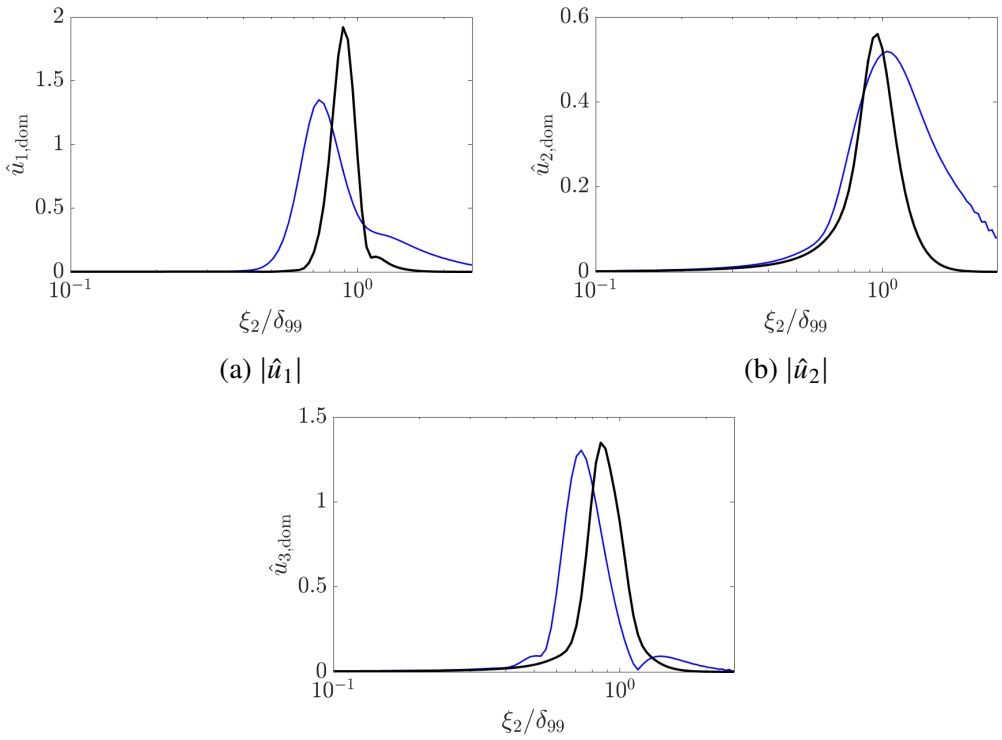

(a) $|\hat{u}_1|$ (b) $|\hat{u}_2|$

(c) $|\hat{u}_3|$

Figure 5.9: Dominant mode components (a) $|\hat{u}_1|$, (b) $|\hat{u}_2|$, and (c) $|\hat{u}_3|$ for the outer wave at $Re_{\delta^*} = 1460$. Colors: (black) $\mathbf{R}_c$, (black) $\mathbf{R}_p$.

5.4 Displacement of the peak location

The streamwise components of the dominant modes of $\mathbf{R}_c$ and $\mathbf{R}_p$ for the outer wave feature different peak locations and widths, but they have similar shapes. As the streamwise component is responsible for over 80% of the energy in the overall mode, we focus our attention on this component only. More precisely, for a narrow region around the peak, we make the assumption that there exists η_2 such that

$$\hat{u}_{1,cart}\left(\frac{y_p}{y_c}x_2\right) = S\hat{u}_{1,par}(\eta_2) \tag{5.28}$$

for $|x_2 - y_c| < \frac{y_p}{y_c}\epsilon$, where the $(cart)$, and (par) subscripts denote the dominant modes respectively of the Cartesian and parallelized resolvent operator, S denotes a scaling factor, and y_p and y_c denote the peak locations of the optimal response modes for the parallel and Cartesian operators. Because the dominant modes are defined up to a complex constant with magnitude 1, without any loss of generality, we impose that at y_c, $\hat{u}_{1,cart}$ is purely real with positive coefficient. We also make the assumption that at y_c, $\Re[\partial_{x_2}\hat{u}_{1,cart}] \approx 0$.

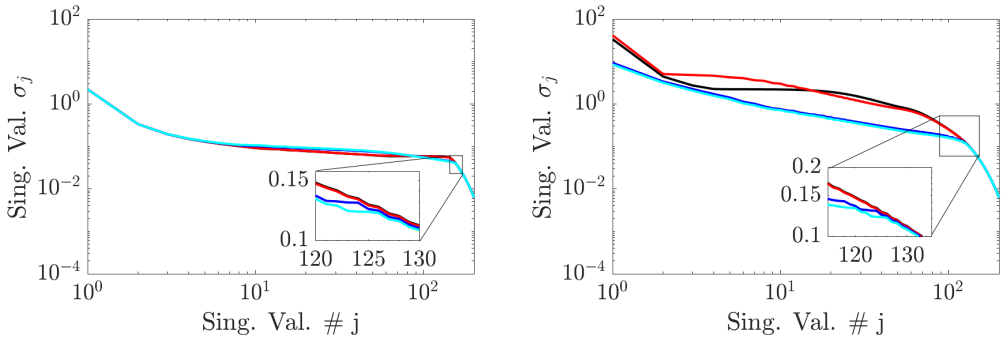

(a) Inner wave (b) Outer wave

Figure 5.10: Singular value spectra of the resolvent operators for the (a) inner and (b) outer waves at $Re_{\delta^*} = 1460$. Colors: (black) $\mathbf{R}_c$, (black) $\mathbf{R}_p$, (red) $\mathbf{R}_{c,+v}$, (cyan) $\mathbf{R}_{p,-v}$.

Following the simplifications of [96] (dropping the forcing and the pressure terms), the streamwise momentum equation for the Cartesian resolvent operator near $x_2 \approx y_c$ yields

$$[L_c]\,\hat{u}_{1,cart} + \frac{d\overline{u}_{1,cart}}{dx_2}\hat{u}_{2,cart} \approx 0 \tag{5.29}$$

Similarly, following similar simplifications, the rescaled streamwise momentum equation near $\eta_2 \approx y_p$ gives

$$\left[L_p\right]\hat{u}_{1,par} + \frac{d\overline{u}_{1,par}}{d\eta_2}\hat{u}_{2,par} \approx 0 \tag{5.30}$$

where the term $q'/q\eta_2\partial_d\overline{u}_{1,par}\hat{u}_{1,par}$ will be neglected as its magnitude much smaller than that of the streamwise advection term $i\kappa_1\overline{u}_1$ in the outer layer. In the Cartesian streamwise momentum equation, the balance near the peak is only a balance between the streamwise convective and temporal terms $i\kappa_1\overline{u}_1\hat{u}_1 - i\omega\hat{u}_1$. The wall-normal location where this is satisfied is the location of the peak of the dominant singular mode (i.e. $\overline{u}_1(y_c) = \omega/\kappa_1$). However, since the rescaled peak location has shifted, the streamwise momentum is no longer just a balance of the streamwise convective and unsteady terms. The additional source term $q'/q\xi_2\partial_{\xi_2}\hat{u}_1$ and $\overline{u}_2$ term must be retained.

Closures for $\hat{u}_{2,cart}$ and $\hat{u}_{2,par}$ can be provided by an approximation of continuity:

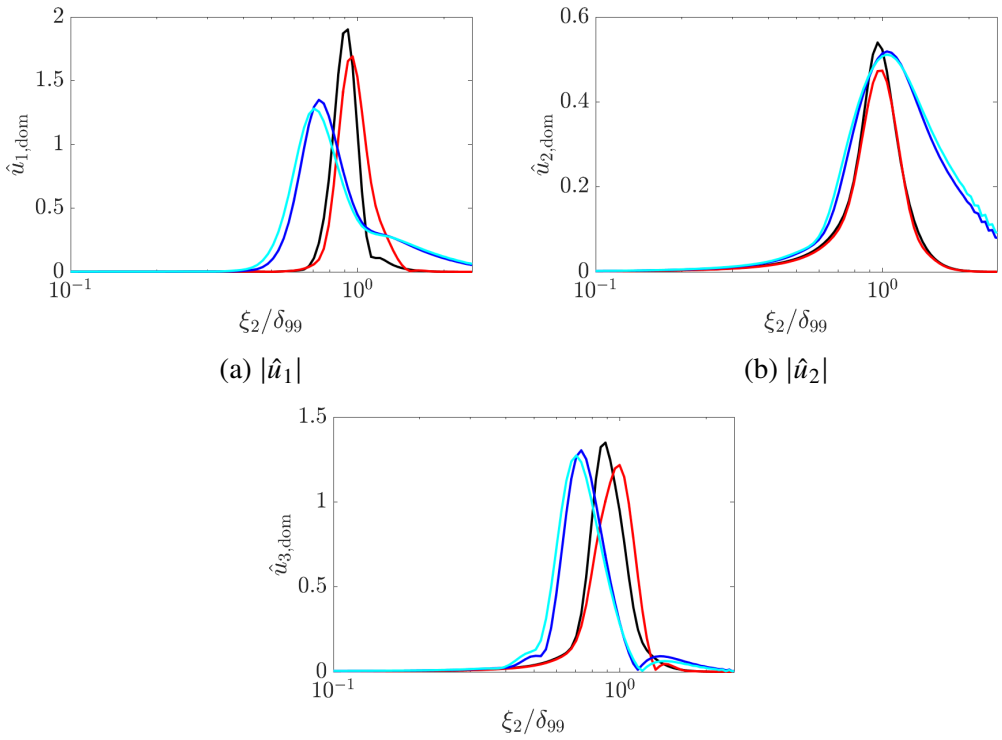

(a) $|\hat{u}_1|$ (b) $|\hat{u}_2|$

(c) $|\hat{u}_3|$

Figure 5.11: Dominant mode components (a) $|\hat{u}_1|$, (b) $|\hat{u}_2|$, and (c) $|\hat{u}_3|$ for outer wave at $Re_{\delta^*} = 1460$. Colors: (black) $\mathbf{R}_c$, (black) $\mathbf{R}_p$, (red) $\mathbf{R}_{c,+v}$, (cyan) $\mathbf{R}_{p,-v}$.

$$\hat{u}_{2,par}(\eta_2) \approx \frac{y_c}{y_p} S\hat{u}_{2,cart}\left(\frac{y_p}{y_c}x_2\right) \tag{5.31}$$

The similarity assumption (Eq. 5.28), reduced momentum equations (Eq. 5.29-5.30), and reduced continuity equation (Eq. 5.31) provide the following expression after Taylor expansion around $x_2 = y_c$ and neglecting of the viscous terms

$$\left(\frac{y_p}{y_c} - 1\right)\left[\kappa_1\left(\frac{d\overline{u}_1}{dx_2}\right) y_c Re[\hat{u}_{1,cart}] + \frac{d\overline{u}_1}{dx_2} Im[\hat{u}_{2,cart}]\right] + \left(\overline{u}_2(y_p) - \frac{q'}{q}y_p\right)\frac{y_c}{y_p} Im\left[\frac{d\hat{u}_{1,cart}}{dx_2}\right] = 0 \tag{5.32}$$

where, unless otherwise specified, terms are evaluated at $x_2 = y_c$. To first order in y_p/y_c, we obtain the following approximation

$$\frac{y_p}{y_c} \approx 1 - \frac{\left(\overline{u}_2(y_p) - \frac{q'}{q}y_p\right) Im\left[\frac{d\hat{u}_{1,cart}}{dx_2}\right]}{\kappa_1 y_c \frac{d\overline{u}_1}{dx_2} Re[\hat{u}_{1,cart}] + \frac{d\overline{u}_1}{dx_2} Im[\hat{u}_{2,cart}]} \tag{5.33}$$

Note that due to the linearity of Eq. 5.30 in $\hat{u}_{1,par}, \hat{u}_{2,par}$, the scaling parameter S does not play a direct role in the final expression for the shift in peak location.

For $\mathbf{R}_p$, the actual peak of the dominant mode is located at $\xi_2/\delta_{99} = 0.73$ whereas the similarity prediction expects $\xi_2/\delta_{99} = 0.74$. In the case of $\mathbf{R}_{c,+v}$ the actual peak is located at $y/\delta_{99} = 0.95$ and the predicted peak is located at 0.96. In both cases, the prediction is within 95% of the actual value.

Equation 5.33 can be interpreted as the translation of the flow due to vertical advection. The numerator of Eq. 5.33 contains metric terms due to vertical advection from boundary layer growth and the denominator contains terms related to horizontal advection and production of turbulent fluctuations. The ratio of the two provides a relative context for how quickly a fluctuation might be pulled towards/away from the wall with respect to advection by the mean flow. It is also clear that the effect of the mean wall-normal velocity profile will always be opposite that of the rescaling terms. Finally, in the limit of infinite Reynolds number, the metric term q'/q and the wall-normal velocity both approach zero. In this limit, the Cartesian and parallelized resolvent operators would produce the same modes.

5.5 Spectral proper orthogonal decomposition

The current section gives a brief overview of SPOD. Then SPOD is applied to a boundary layer dataset and modes are extracted for comparison against the predicted resolvent modes.

5.5.1 Method overview

The present analysis utilizes SPOD and follows the procedure of Towne *et al.* (2018). The method consists of organizing a long time stream of data files of the state vector $\mathbf{g}'$ into overlapping blocks (via the snapshot method) and then conducting Fourier transforms in time and in the homogeneous directions of each block. Specifically for the periodic boundary layer, the Fourier transforms are conducted in the streamwise, spanwise, and temporal directions. One then specifies a set of wavenumbers $\kappa = (\kappa_1, \kappa_3, \omega)$ and extracts data in the form of an array $\tilde{\mathbf{Q}}$ of size $4N_y \times N_{\text{blks}}$, where N_{blks} is the number of blocks and $4N_y$ is the length of the incompressible state vector.

The two-point cross-spectral density tensor $\mathbf{S}$ is then estimated by $\mathbf{S} = \tilde{\mathbf{Q}}\tilde{\mathbf{Q}}^{\dagger}/N_{\text{blks}}$. An eigenvector decomposition is finally applied to the cross-spectral density tensor to obtain eigenfunctions $\hat{\psi}$ such that

$$\int \mathbf{S}(\xi_2, \xi_2', \kappa)\psi(\xi_2', \kappa)d\xi_2' = \lambda(\kappa)\psi\xi_2, \kappa \tag{5.34}$$

Because **S** is Hermitian, the eigenfunctions are orthogonal and the eigenvalues are positive and real and can be sorted from largest to smallest. The eigenfunction associated with the largest eigenvalue can be loosely interpreted as representations of turbulent structures that appear most prominently in each flow snapshot for the specific set of wavenumbers κ.

Comparisons between resolvent analysis and SPOD have been numerous [25, 27, 82]. One can relate the modes predicted by resolvent analysis with the modes extracted by SPOD, provided the resolvent operator is suitably low-rank. In this situation, cross spectral density may be dominated by the optimal resolvent response mode [25, 97, 98].

5.5.2 Numerics

To reduce memory and storage costs, each snapshot was down-sampled by a factor of four in the streamwise direction and two in the spanwise direction, corresponding to filtering out waves of streamwise length $\lambda_1^+ < 72$ and spanwise length $\lambda_3^+ < 24$. The down-sampling was conducted in Fourier space with a sharp wavenumber cutoff to prevent aliasing. Since the flow is simulated with streamwise and spanwise periodic boundary conditions, and SPOD is conducted fully in Fourier space for the same directions, the down-sampling does not affect results.

A total of 6250 snapshots were used with time increment $\Delta t U_\infty/\delta_{99} \approx 0.3$, $\Delta t^+ \approx 6.5$. Each block was formed with 256 snapshots for a total temporal wavelength of $\Delta T^+ \approx 1600$, $\Delta T U_\infty/\delta_{99} \approx 84$, $\Delta T u_\tau/\delta_{99} \approx 4$ so as to fully capture the longest temporal wavelength of interest ($\lambda_t^+ \approx 100$). For the bulk of the results used in this chapter, each block had an overlap of 50%, for a total of 47 blocks. A study of the convergence of the modes is provided in Appendix A.4.

5.5.3 Resolvent and SPOD comparisons

It was shown in Section 5.3 that for both modes, the resolvent operator was approximately low-rank. Analogous results are shown in Fig. 5.12 for the eigenvalue spectra of each wave. The outer wave shows low-rank behavior, with the first mode having an eigenvalue nearly twice that of the subdominant mode. The inner wave shows much stronger low-rank behavior as the dominant mode has an eigenvalue nearly five times that of the subdominant mode. Similar to the singular spectra of

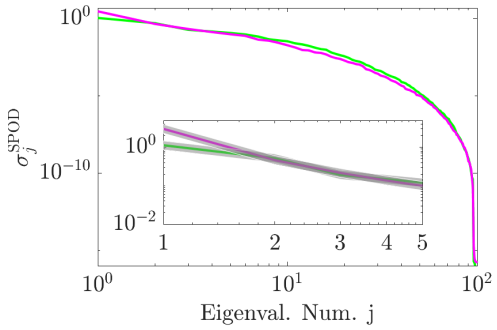

Figure 5.12: Eigenspectra for SPOD modes associated with (green) outer wave $(\lambda_1^+, \lambda_3^+, \lambda_t^+) = (650, 450, 33)$ and (magenta) inner wave $(\lambda_1^+, \lambda_3^+, \lambda_t^+) = (550, 100, 100)$. Gray shading indicates 95% confidence interval.

the resolvent operators, there is a sharp drop in eigenvalue energy at around mode number 100, which is on the order of the number of points used in the wall-normal direction.

Following Section 5.3, we show the magnitude of the streamwise component of the dominant SPOD and optimal resolvent modes for the inner and outer waves . Figure (5.13a) shows the magnitude of the inner wave SPOD and resolvent modes. The streamwise component is consistently larger in magnitude compared to the other two components. The location of the peak in the inner layer is within 5%, and the three velocity component (not shown) shapes all share similar features. The wall-normal and spanwise components of the SPOD mode have magnitudes are much smaller in magnitude compared to the streamwise component, which is consistent with the dominant resolvent mode. The streamwise component for the SPOD mode is slightly smaller than predicted by the resolvent modes and consequently, the wall-normal and spanwise components of the SPOD modes are slightly larger than the predicted modes by resolvent analysis. Finally, the wall-normal extent is larger than predicted.

Figure 5.13b shows the magnitude of the outer wave SPOD and resolvent modes. The peak location and relative magnitude of the SPOD mode is captured by the optimal resolvent mode R_p within 5%. The R_p optimal mode is tilted towards the wall, but overall, appears to capture the SPOD mode amplitude shape and location well. In comparison, the R_c optimal mode does not predict the location or mode width well. It does appear that the free-stream extent of the SPOD mode is more subdued than that predicted by R_p and the SPOD mode also has a much longer near-wall extent.

Figure 5.14 shows the reconstructed dominant SPOD modes compared with the

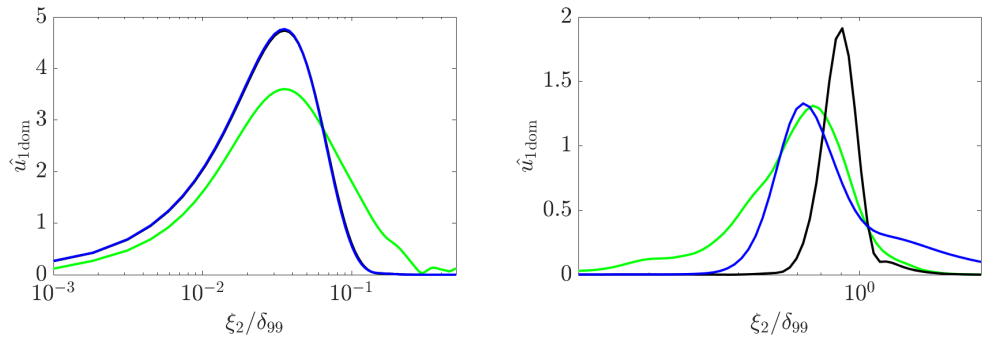

(a) Inner wave (b) Outer wave

Figure 5.13: Envelopes for streamwise component of dominant resolvent and SPOD modes for (b) Inner $(\lambda_1^+, \lambda_3^+, \lambda_t^+) = (550, 100, 100)$ and (b) Outer waves $(\lambda_1^+, \lambda_3^+, \lambda_t^+) = (650, 450, 33)$. Colors: (black) Predicted mode from $\mathbf{R}_c$, (black) Predicted mode from $\mathbf{R}_p$, (green) SPOD mode.

reconstructed optimal resolvent response modes for BL1460. In red and black are positive and negative contours, respectively, of streamwise u_1' velocity whereas the arrows indicate the wall-normal velocity u_2'. The inner wave modes between R_c and R_p are indistinguishable. Noticeably, for the SPOD and resolvent inner wave modes, the positive lobes of u_1' are correlated with negative values of u_2' specifically near the peak amplitude of the fluctuations. This is indicative of the lift-up mechanism in the resolvent formalism.

To differentiate the resolvent lift-up mechanism from the classical lift-up mechanism, we follow the explanation given by [28]. In classical linear instability analysis, the lift-up mechanism corresponds to a linear instability mechanism where wall-normal velocity fluctuations cause an algebraic increase in streamwise velocity fluctuations [99]. For example, if one considers streamwise and wall-normal fluctuations u_1' and u_2', respectively, in inviscid, parallel flow with mean velocity $\overline{u}_1$, one finds from the streamwise momentum equation

$$\frac{\partial u_1'}{\partial t} = -u_2' \frac{\partial \overline{u}_1}{\partial x_2} \tag{5.35}$$

where it can be seen that the perturbation u_1' is amplified in the presence of -u_2'. The term $u_2' \partial \overline{u}_1 / \partial x_2$ is responsible for the classical lift-up mechanism. Lift-up tends to force slow-moving fluid away from the wall and vice-versa, which aids the formation of streamwise streaks. [100]. Thus, the classical lift-up mechanism specifically concerns instabilities that grow linearly with time.

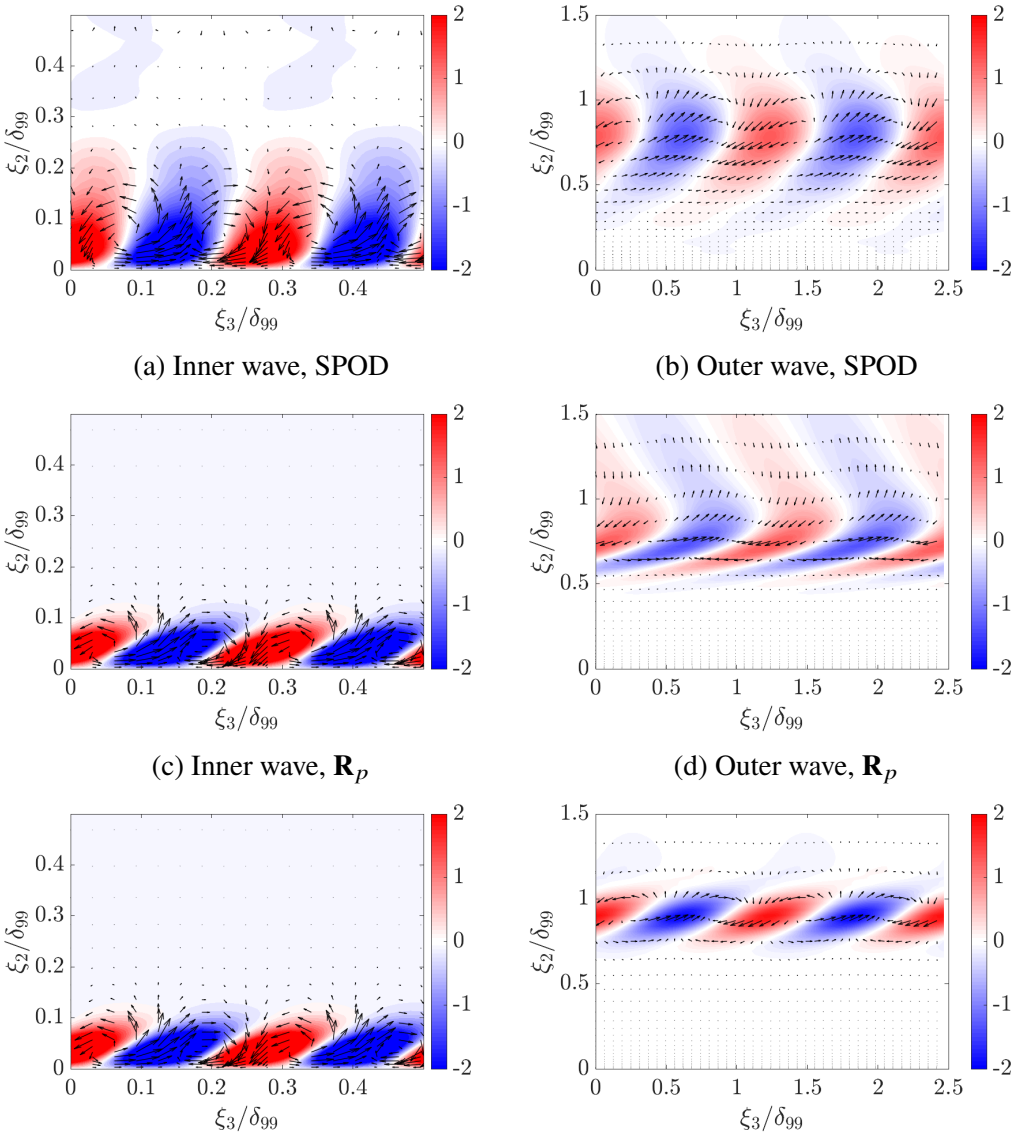

(a) Inner wave, SPOD

(b) Outer wave, SPOD

(c) Inner wave, $\mathbf{R}_p$

(d) Outer wave, $\mathbf{R}_p$

(e) Inner wave, $\mathbf{R}_c$

(f) Outer wave, $\mathbf{R}_c$

Figure 5.14: Velocity fields in cross-stream (zy) view for dominant modes of SPOD (a,b), $\mathbf{R}_c$ (c,d) and $\mathbf{R}_p$ (e,f) for (a,c,e) outer wave $(\lambda_1^+, \lambda_3^+, \lambda_t^+) = (650, 450, 33)$ and (b,d,f) inner wave $(\lambda_1^+, \lambda_3^+, \lambda_t^+) = (550, 100, 100)$. Colored contours represent $Re[\hat{u}'_1]$ and quiver arrows represent $Re[\hat{u}'_2 - \hat{u}'_3]$.

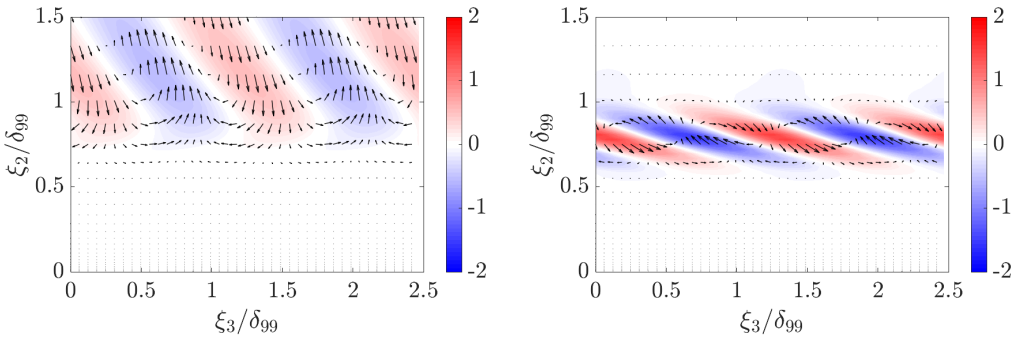

(a) $\mathbf{R}_p$ (b) $\mathbf{R}_c$

Figure 5.15: Optimal forcings in cross-stream (zy) view for outer wave for (a) $\mathbf{R}_p$ and (b)$\mathbf{R}_c$. Colored contours represent $Re[\hat{f}_1']$ and quiver arrows represent $Re[\hat{f}_2' - \hat{f}_3']$.

In the resolvent formalism, the streamwise vortices (fluctuations in u_2' and u_3') are energized by forcing components f_2 and f_3. Once energized, these fluctuations in u_2' can then amplify fluctuations in u_1'. And so, unlike the classical lift-up mechanism, the resolvent lift-up mechanism has nonlinear terms exciting streamwise vortices. These streamwise vortices eventually amplify streaks which, eventually break down due. This is a broad description of the near-wall cycle, and for more details, the reader is referred to [99, 101]. In the resolvent case, the lift-up mechanism can be characterized by the presence of negative wall-normal momentum associated with positive streamwise momentum, specifically in the vicinity of the location where the fluctuations have peak amplitude [99]. From this description, it is clear that the inner wave SPOD and resolvent modes feature lift-up.

For the outer wave, all three modes also feature lift-up (near the peak, u_1' is negatively correlated with u_2'), and all peak in the outer layer. The optimal R_p response mode shows agreement in free-stream behavior with the SPOD extracted mode. where both modes change inclination angle. This is in contrast to the optimal R_c response mode, which maintains a steady inclination angle in the free-stream.

Differences in optimal response modes are generally indicative of differences in optimal forcing modes as well. The forcing modes for both R_c and R_p are shown in Fig. 5.15. Both R_c and R_p feature forcing modes tilted upstream, which is indicative of the resolvent Orr mechanism [83, 84]. The classic Orr mechanism is derived from linear stability analysis of inviscid, parallel shear flows, and there describes the linear phenomenon where vorticity perturbations oscillate between being aligned with and against the mean shear. The energy of these perturbations grows algebraically in time.

The resolvent Orr mechanism is characterized by nonlinear forcings that are tilted against the shear, which amplify a response that is tilted with the shear. The optimal forcing mode of R_c has a smaller angle of inclination, indicating that R_p predicts a much weaker Orr mechanism than R_c. Given the good agreement between the SPOD modes and the resolvent modes, it is likely that the Orr mechanism is weaker in the outer layer than previously predicted by the 1D Cartesian resolvent operator.

5.6 Conclusion

The present chapter extended the analysis of the rescaled governing equations via resolvent analysis and SPOD. First, the energy spectra were computed both spatially and temporally to discover the most energetic modes for specific sets of wavenumbers that would be representative of turbulent motions in the outer and inner layers. Once these modes were identified, 1D resolvent analysis was conducted for both of the specified wavenumber triplets. It was found that the rescaled governing equations predict a shift in optimal mode peak location. Through an investigation of the left singular vectors of the rescaled and Cartesian resolvent operators, it was shown that both the rescaling metric term and the mean wall-normal velocity profile leave impacts on the peak mode location, especially for modes in the outer layer. Furthermore, it was shown through a Taylor series expansion of the resolvent analysis equations near the peak mode location, that the displacement in peak mode location can be directly interpreted in terms of a ratio between vertical advection and horizontal advection. The rescaling operation moved the mode peak closer to the wall, whereas vertical transpiration moved the mode peak further from the wall. SPOD was then conducted on case BL1460, and the dominant modes were extracted. The rescaled resolvent predicted the peak location of extracted mode within 5%, and shared mode features like inclination angle in the free-stream. It was concluded that the Orr mechanism in the outer layer is far weaker than predicted by the 1D resolvent operator.

Chapter 6

CONCLUSIONS & FUTURE WORK

A novel method of simulating incompressible flat plate boundary layers in a streamwise periodic domain was developed. The method was validated, and investigations were conducted into the behavior of the equations with increased Reynolds number as well as the numerical requirements to fully capture the largest turbulent features in the flow. Finally, the method was applied to resolvent analysis and SPOD was conducted on resulting periodic simulation data.

6.1 Development and validation of the periodic boundary layer

Based on the boundary layer rescaling methods pioneered by Spalart (1987), a new wall-normal rescaling (by a single length-scale q) was applied to the Navier-Stokes equations to obtain the Homogenized Navier-Stokes equations. The new governing equations shared a similar form to the original Navier-Stokes equations but with additional source terms. Each of these source terms were proportional to a factor of q'/q, and it was shown that in order for the Homogenized Navier-Stokes equations to be stationary, the rescaling metric q'/q is approximately $\frac{1}{2}C_f/\theta$. Consequently, it was also shown that the length-scale q scales like θ and that one could understand this rescaling as a rescaling by the momentum thickness.

Several *a priori* tests were conducted to investigate the role of the source terms. First, it was shown that the momentum source terms were most active in the outer layer. More specifically, in the streamwise momentum equation, the additional source terms directly balance the effect of the Reynolds shear stress. The *a priori* tests also revealed that several of the additional source terms (specifically viscous and pressure rescaling terms) in the rescaled governing equations were negligible and were thus neglected in the governing equations.

Several non-periodic simulations were then conducted using the rescaled governing equations. It was found that the neglected terms did not leave significant impacts on the streamwise mean or rms profiles. It was also shown that given fixed values of q'/q, the governing equations allowed for a statistically streamwise homogeneous flow. It was concluded that streamwise periodic boundary conditions could be appropriately applied without artificially enforcing streamwise statistical homogeneity.

Four key periodic boundary layer simulations were conducted at $Re_{\delta^*} = 1460, 2830, 3550$, and 5650. The shape factor and skin friction coefficient were found to be within 1% and 3% of empirical values and showed excellent agreement with growing simulation results. Notably, the rms profiles were within 5% of experimental values for $Re_{\delta^*} = 3550, 5650$.

There was significant computational cost reduction due to a reduction in streamwise domain length. For example, for a $Re_{\delta^*} = 5650$, the streamwise domain of the periodic simulation was $\sim 7\delta_{99}$. In comparison, the streamwise domain of growing simulations required $\sim$ 55-60δ_{99} to reach the same Reynolds number for both [39] and [14]. Based solely on streamwise domain length, the expected cost reduction is about an order of magnitude. This cost reduction is only expected to improve with increasing Reynolds number as inflow relaxation lengths for growing boundary layer simulations often scale with Reynolds number [14]. It was concluded that the periodic boundary layer was both highly cost-efficient and accurate.

An investigation was then conducted into whether there were any near-wall effects missing from the current Homogenized Navier-Stokes equations. The most clear evidence of near-wall impact is in the mean wall-normal velocity profile. It was shown that there were at most 5% relative differences in the transpiration velocity $u_{2,\infty}$ between the growing and periodic boundary layer simulations. These differences were shown to be caused by an overestimation of q'/q in the inner region. Consequently, it was shown that by modifying the expression for q to vary in the wall-normal direction, one could obtain mean transpiration velocities within 1-2% of the growing boundary layer simulation values. It was finally shown, however, that such changes are much more significant with lower Reynolds number, and such differences decay logarithmically with Reynolds number.

The numerical domain size was then investigated to understand what domain sizes were necessary so that a periodic simulation could obtain accurate two-point correlations. It was found that spanwise domain lengths of $O(5\delta_{99})$ are sufficient to capture the longest streamwise structures in the domain. Furthermore, it was concluded that shorter spanwise domains in fact reduce the longest possible streamwise structures in the computational domain. It was concluded that for adequately large domain size ($14\delta_{99}$ in length, $5\delta_{99}$ in width), the two-point statistics of the growing boundary layer are accurately captured by the periodic boundary layer and consequently, the turbulent structures of such size are also accurately captured.

Spatial and temporal PSD were then computed to find the wavelengths corresponding

to the most energetic waves in the boundary layer. For $Re_{\delta^*} = 1460$, these were found to be at $(\lambda_1^+, \lambda_3^+, \lambda_t^+) = (550, 100, 50), (650, 450, 33)$ for the inner and outer waves, respectively. A study was then conducted on how the 1D resolvent operator changes if one uses the Homogenized Navier-Stokes equations instead of the Cartesian Navier-Stokes equations. The optimal modes were extracted for each wave. No differences between the 1D operators were found for the inner wave, but the outer wave featured a shift in the peak location as well as different free-stream behavior. It was shown that this shift in peak location could be approximately explained by a ratio of advection terms. Furthermore, it was shown that the rescaling terms displaced the peak towards the wall, whilst the mean wall-normal velocity pushed the peak towards the free-stream. Finally, to verify that these behaviors were in fact found in periodic boundary layers, SPOD was conducted on a case at $Re_{\delta^*} = 1460$ and the dominant modes were extracted for the inner and outer waves. The peak location of the outer wave SPOD mode was predicted within 5% by the rescaled resolvent operator mode.

6.2 Conditions for application

Throughout each chapter, the rescaling method has been successful due to one condition: the streamwise growth of the boundary layer must be slow, or that $q_0'/q_0\delta^* \ll 1$. In other words, the flow must be quasi-homogeneous in the streamwise direction.

In Chapter 2, it was noted that the source term was orders of magnitude smaller than the dominant terms in the near-wall region, and so, despite the near wall region featuring an altogether different wall-normal rescaling, the effect on the mean streamwise velocity profile was minimal. This argument is only possible because the growth rate $q_0'/q_0\delta^*$ is small. Even so, the effect still manifested itself through the form of a transpiration velocity error (Chapter 3). It was found that the mean and rms velocity profiles are largely insensitive to differences in transpiration velocity. The same conclusion could not be made if the transpiration velocity was several orders of magnitude larger. Note that $u_{2,\infty}/u_{1,\infty} \approx q_0'/q_0\delta^*$, and so, yet again, the insensitivity of the boundary layer to errors in $u_{2,\infty}$ is fundamentally related to the small value of $q_0'/q_0\delta^*$.

In Chapter 4, the two-point correlation functions were compared between growing and homogeneous boundary layers. The inclination angle for the two-point correlations were similar, which is yet another natural consequence of $q_0'/q_0\delta^*$ being small. If the growth were even an order of magnitude larger, the inclination angles would

differ significantly. Furthermore, the alignment error caused by the differences in coordinate systems was computed and found to be negligible. This small alignment error would play a crucial role in Chapter 5. Direct comparisons between Fourier transforms in Cartesian and rescaled coordinates would not be possible if the two coordinate systems were heavily misaligned.

In each of the chapters, the same requirement backing each of the successes is that the growth rate $q_0'/q_0\delta^* \ll 1$. For fully turbulent flows, a slow streamwise growth rate allows for relative streamwise homogeneity.

For boundary layer flows with large pressure gradients, the growth and/or change of the boundary layer may become significant enough that $u_{2,\infty}/u_{1,\infty}$, or equivalently, $q_0'/q_0\delta^*$ is large. In these situations, the rescaling technique cannot be applied. Consequently, this requirement excludes several types of flows.

6.3 Extensions

It was noted in the introduction that boundary layers cover a wide range of complex geometries and are sensitive to at least three different conditions: (1) heat transfer effects, (2) roughness, and (3) pressure gradients. Extensions for each of these will be considered in the following subsections.

6.3.0.1 Thermal boundary layers

Just like momentum boundary layers, thermal boundary layers develop over surfaces. In this case, the thermal boundary thickness growth rate is dependent not only on the Reynolds number but the Péclet number. Provided slow variation in the thermal boundary layer thickness, one can envision a second wall-normal coordinate rescaling for the temperature equation. The wall-normal rescaling will specifically be with respect to the thermal boundary layer thickness q_T. One will obtain source terms in the temperature equation related to q_T'/q_T. The resulting simulation will inherently be conducted at a user-imposed Péclet and Reynolds number. This is equivalent to specifying a constant ratio of the momentum boundary layer thickness to the thermal boundary layer thickness for constant Reynolds number and Prandtl number.

6.3.0.2 Roughness

The mean velocity profiles for rough wall boundary layers feature self-similarity with respect to the wall-normal coordinate in the outer layer, away from the rough-

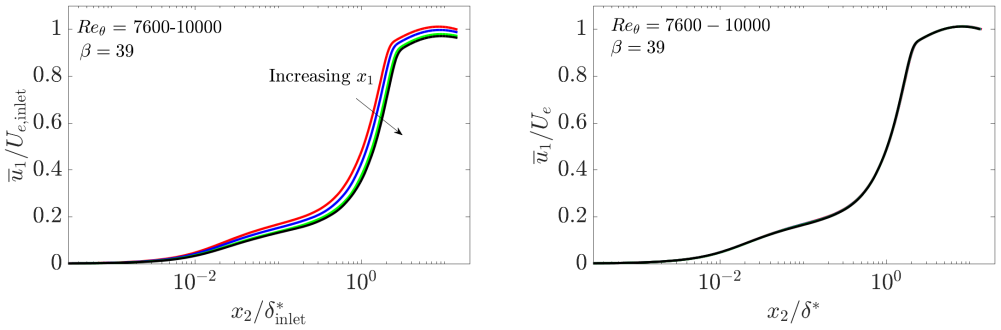

(a) Unscaled (b) Scaled

Figure 6.1: Profiles of streamwise velocity (a) unscaled mean and (b) scaled mean in outer units U_e and δ^* of an adverse pressure gradient with $\beta = \partial P/\partial x_1/\tau_w\delta^* = 39$. Colors: (red) profiles from $Re_\theta = 7600 - 1000$. Data from Kitsios *et al.* 2017.

ness sublayer. Here, the flow is primarily dependent on the momentum thickness Reynolds number, the roughness Reynolds number and rescaled wall-normal coordinate. If one has any *a priori* estimates of the viscous stresses in the roughness sublayer, one can estimate whether the rescaling source terms are negligible in the roughness sublayer. In this case, assuming that the roughness elements are also approximately streamwise homogeneous in the rescaled coordinate system, one can apply the rescaling methodology to a rough wall boundary layer flow after prescribing both Reynolds numbers.

6.3.0.3 Pressure gradient flow

Supposing one has a boundary layer under a pressure gradient such that its relative change in boundary layer thickness is small, then it would be possible to extend the current rescaling methodology to the pressure gradient boundary layer.

It is known that there exist self-similar boundary layers $\overline{u}_1 = U_e\overline{u}^*_1(x_2/\delta_{99})$ even under pressure gradient (see Fig. 6.1), where $U_e(x_1)$ is the boundary edge velocity and $P_e(x_1, x_2)$ is the edge pressure, computed via RANS simulation or otherwise. One can then solve for the following homogenized variables u^*_1, u^*_2, u^*_3, and P^*, which are defined as follows

$$u_1 = u^*_1\frac{U_e(x_1)}{u_{1,\infty}} \qquad u_2 = V_e + u^*_2 \qquad u^*_3 = u_3 \qquad P = P^* + P_e \tag{6.1}$$

where $V_e = -x_2U'_e$, and $u_{1,\infty} = U_e(x_0)$, which is the value that u^*_1 approaches at the boundary layer edge. U_e, V_e, and P_e, by construction, satisfy the free-stream

equations outside of the boundary layer (potential flow or otherwise), but have limited validity near the wall. The form of V_e completes the solution at the boundary layer edge. As with Chapter 2, we focus on a particular streamwise location x_0. In these equations, u_1^*, u_2^*, and u_3^* are assumed to have Dirichlet conditions at the wall and Neumann conditions at the free-stream.

The rescaled continuity equation is given by

$$\frac{\partial u_j^*}{\partial \xi_j} = \xi_2 \frac{q'}{q} \frac{\partial u_1^*}{\partial \xi_2} + \frac{U_e'}{u_{1,\infty}} \left(u_{1,\infty} - u_1^* \right) + H_c^p \tag{6.2}$$

with

$$H_c^p = \left(1 - \frac{U_e}{u_{1,\infty}} \right) \frac{\partial u_1^*}{\partial \xi_1} + \left(1 - \frac{q_0}{q} \right) \frac{\partial u_2^*}{\partial \xi_2} \tag{6.3}$$

Similarly, the momentum equations are given by

$$\frac{\partial u_i^*}{\partial t} + u_j^* \frac{\partial u_i^*}{\partial \xi_j} + \frac{1}{\rho} \frac{\partial P}{\partial \xi_i} - \nu \frac{\partial^2 u_i^*}{\partial \xi_k^2} = -\delta_{1i} \frac{U_e'}{u_{1,\infty}} u_1^{*,2} - V_e \frac{\partial u_i^*}{\partial \xi_2} - \frac{1}{\rho} \frac{\partial P_e}{\partial \xi_i} + \xi_2 \frac{q'}{q} u_1 \frac{\partial u_i^*}{\partial \xi_1} + H_p^p(u_i) + H_\nu^p(u_i) \tag{6.4}$$

where

$$H_p^p(u_i) = \delta_{1i} \xi_2 \frac{q'}{q} \frac{1}{\rho} \frac{\partial P_e + P^*}{\partial \xi_2} + \left(1 - \frac{q_0}{q} \right) \left((u_2^* + V_e) \frac{\partial u_1^*}{\partial \xi_2} + \delta_{2i} \frac{1}{\rho} \frac{\partial P^*}{\partial \xi_2} \right) + \left(1 - \frac{U_e}{u_{1,\infty}} \right) \left(\delta_{1i} \frac{U_e'}{U_e} u_1^{*,2} + u_1^* \frac{\partial u_i^*}{\partial x_1} \left(1 - \delta_{1i} + \delta_{1i} \frac{U_e}{u_{1,\infty}} \right) \right) \tag{6.5}$$

$$H_\nu^p(u_i) = \nu \delta_{1i} \left(\frac{U_e''}{u_{1,\infty}} u_1^* + 2 \frac{U_e'}{u_{1,\infty}} \left[\frac{\partial u_1^*}{\partial \xi_1} - \xi_2 \frac{q'}{q} \frac{\partial u_1^*}{\partial \xi_2} \right] \right) + \left(1 - \delta_{1i} + \delta_{1i} \frac{U_e}{u_{1,\infty}} \right) \times \left[\nu \left[1 - \left(\frac{q_0}{q} \right)^2 + \left(\xi_2 \frac{q'}{q} \right)^2 \right] \frac{\partial^2 u_i^*}{\partial \xi_2^2} + \nu \left[2 \left(\frac{q'}{q} \right)^2 - \frac{q''}{q} \right] \xi_2 \frac{\partial u_i^*}{\partial \xi_2} - 2\nu \xi_2 \frac{q'}{q} \frac{\partial^2 u_i^*}{\partial \xi_1 \partial \xi_2} \right] \tag{6.6}$$

After evaluation at $\xi_1 = x_0$, a few important terms remain: U_e', P_e and U_e''. For flows with slow streamwise development, the impact of U_e'' is likely to be small. The remaining inputs can be directly related via the streamwise momentum equation in the free-stream, and thus, the only input required will be the edge pressure, or equivalently, its gradient.

Appendix A

ORDER OF ACCURACY

Periodic flows are typically computed using spectral codes. The main results of this manuscript use 4th order finite difference operators. To verify that these spatial operators are adequate, case BL1460 was rerun with 2nd and 6th order finite difference operators. The results are shown in Fig. A.1

The skin friction coefficients vary by less than 0.2%. In terms of mean profiles, the deviation between all three methods was less than 1%. Consequently, the shape factors are within 0.5% of each other. There is a slight discrepancy in the mean profile at the overlap region $\xi_2^+ \approx 500$ between the 2nd order and higher order profiles.

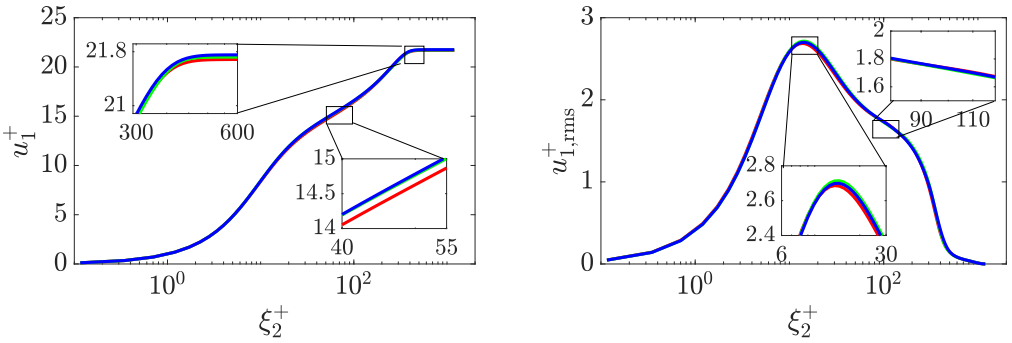

(a) streamwise mean

(b) streamwise rms

Figure A.1: Streamwise mean (a) velocity and (b) rms profiles for $Re_{\delta^*} = 1460$ for different order spatial operators. Colors: (red) 2nd Order, (black) 4th Order, (green) 6th Order.

Appendix B

RE-LAMINARIZATION

The current method can obtain a statistically stationary turbulent field from an initially laminar boundary layer superimposed with white noise. The converse is also possible: a laminar profile can be re-obtained from a fully turbulent profile. A simulation was initialized with a turbulent field at $Re_{\delta^*} = 1460$ and then run with a high viscosity (corresponding to $Re_{\delta^*} = 100$). Instantaneous mean velocity and rms profiles are computed through averaging in the streamwise and spanwise directions and are shown in Fig. B.1.

The turbulent fluctuations quickly decay near the wall and more slowly far from the wall. The mean profile initially reduces its gradient near the wall and later steepens in the wake region. Eventually, the Blasius solution is obtained with zero residual turbulent fluctuations.

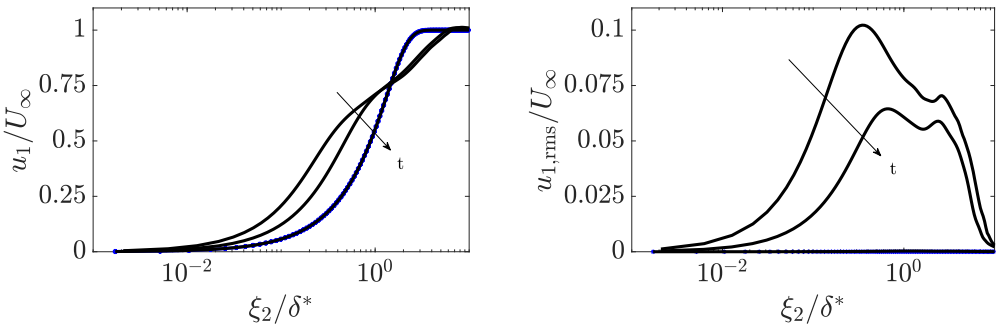

(a) Instantaneous mean

(b) Instantaneous rms

Figure B.1: Instantaneous (a) mean and (b) rms profiles for a laminarization of an initially turbulent boundary layer. Colors: (black ∘) Blasius solution, (black) Instantaneous profiles.

Appendix C

TURBULENT KINETIC ENERGY

The turbulent kinetic energy equation post evaluation at $x = x_0$ is given by

$$\frac{\partial k}{\partial t} + \underbrace{\overline{u_2}\frac{\partial k}{\partial \xi_2}}_{Turb.Advec.} = \underbrace{-\frac{1}{\rho}\frac{\partial \overline{u_2' p'}}{\partial \xi_2}}_{Pres.Diff.} \underbrace{-\frac{1}{2}\frac{\partial \overline{u_j' u_j' u_2'}}{\partial \xi_2}}_{Turb.Diff.} + \underbrace{\nu\frac{\partial^2 k}{\partial \xi_2^2}}_{Visc.Diff.} \underbrace{-\overline{u_i' u_2'}\frac{\partial \overline{u_i}}{\partial \xi_2}}_{Production} \underbrace{-\nu\overline{\frac{\partial u_i'}{\partial \xi_j}\frac{\partial u_i'}{\partial \xi_j}}}_{Dissipation} + Src\ Cont. + H_\nu\ Cont. + H_p\ Cont. \tag{C.1}$$

where $k = 1/2\overline{u_i' u_i'}$ and the Src, H_p and H_ν contributions are given by

$$Src\ Cont. = \frac{q'}{q}\xi_2\left(\overline{u}_1\frac{\partial k}{\partial \xi_2} + \frac{1}{2}\frac{\partial \overline{u_j' u_j' u_1'}}{\partial \xi_2} + \overline{u_i' u_1'}\frac{\partial \overline{u_i}}{\partial \xi_2}\right) \tag{C.2}$$

$$H_p\ Cont. = \frac{q'}{q}\xi_2\frac{\partial \overline{u_1' p'}}{\partial \xi_2} \tag{C.3}$$

$$H_\nu\ Cont. = \nu\left(\xi_2\frac{q'}{q}\right)^2\frac{\partial^2 k}{\partial \xi_2^2} + \nu\left[2\left(\frac{q'}{q}\right)^2 - \frac{q''}{q}\right]\xi_2\frac{\partial k}{\partial \xi_2} + -\nu\left(\xi_2\frac{q'}{q}\right)^2\overline{\left(\frac{\partial u_i'}{\partial \xi_2}\frac{\partial u_i'}{\partial \xi_2}\right)} + \nu\xi_2\frac{q'}{q}\overline{\left(\frac{\partial u_i'}{\partial \xi_1}\frac{\partial u_i'}{\partial \xi_2}\right)} \tag{C.4}$$

Appendix D

CONVERGENCE OF SPOD MODES

SPOD mode convergence depends on block sizes, block overlap and the number of total data files. To verify the convergence of the dominant SPOD modes, we follow [27] and conduct a miniature cross-validation convergence analysis. This test involves splitting the total dataset into two roughly equal portions that each contain 75% of the original dataset and then applying SPOD to each subset. The extracted SPOD modes for each subset will then be compared to the SPOD modes of using the entire dataset. The comparison takes the form of a projection metric γ_k. If Ψ_k is the k^{th} eigenvector computed via SPOD,then γ_k is defined by

$$\gamma_k = \frac{|\langle \Psi_k^{\text{full}}, \Psi_k^{l} \rangle|}{||\Psi_k^{\text{full}}||||\Psi_k^{l}||} \tag{D.1}$$

where the inner product is the constant kinetic energy norm introduced in Chapter 5, the superscript l denotes that the eigenvector is from a different data configuration, and the "full" superscript denotes the mode computed using the entire dataset. We can use the same projection coefficient to compute differences when using 75% overlap and 25% overlap (with 256 snapshots/block) as well as computing with blocks of 128 files and 512 files (with 50% overlap) for the entire dataset. The

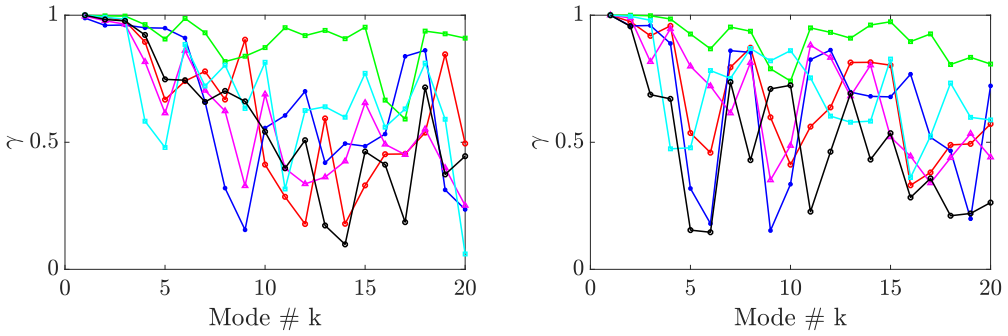

(a) Inner wave (b) Outer wave

Figure D.1: Convergence metric γ of the SPOD modes for (a) inner and (b) outer waves. Colors: (black) Ψ_k computed from the first subset using 75% of the dataset, (red) Ψ_k computed from the second subset using 75% of the entire dataset, (green) Ψ_k computed with 75% overlap, (magenta) Ψ_k using 25% overlap, (cyan) 128 snapshots/block, and (black) 512 snapshots/block.

hope is that, for all cases, the dominant mode is reasonably converged. Figure D.1 shows the comparison metrics for inner and outer waves, with red and black curves corresponding to convergence metrics using subsets of the entire dataset, magenta and green corresponding to the convergence metric for overlaps of 75% and 25%, respectively, and black and cyan corresponding to the same metric for blocks using 512 snapshots/block and 128 snapshots/block, respectively. The dominant and subdominant modes extracted from 75% of the entire dataset have $\gamma \geq 0.95$. For higher modes, the agreement drops sharply, dropping to $\gamma \approx 0.6$ by the 5th mode. It has been noted by Schmidt & Colonius (2020) that $\geq$ 50% overlap between SPOD blocks does not give much improvement to the SPOD modes due to the decreasing independence of each block. This is verified in Fig. D.1, as for both spatio-temporal frequencies, γ associated with 75% overlap (green) does not decrease past 0.7 for any of the modes shown. In contrast, 25% overlap (magenta) shows sharp differences by the 5th mode. For blocks using 512 and 128 snapshots/block, the first two modes are fully converged for both inner and outer waves. This implies that the block sizes are appropriately chosen for these waves. Overall, the extracted dominant SPOD modes for both inner and outer waves are fully converged.

BIBLIOGRAPHY

[1] Environmental and Energy Study Institute. *The growth in greenhouse gas emissions from commercial aviation*. https://www.eesi.org/papers/view/fact-sheet-the-growth-in-greenhouse-gas-emissions-from-commercial-aviation. 2019.

[2] U.S. Department of Transportation. *What the cost of airline fuel means to you*. https://www.transportation.gov/administrations/assistant-secretary-research-and-technology/what-cost-airline-fuel-means-you. 2019.

[3] R. Garcıéa-Mayoral and J. Jiménez. "Drag reduction by riblets". In: *Philosophical Transactions of the Royal Society A: Mathematical, Physical and Engineering Sciences* 369.1940 (Apr. 2011), pp. 1412–1427. DOI: 10.1098/rsta.2010.0359.

[4] J. Kim. "Physics and control of wall turbulence for drag reduction". In: *Philosophical Transactions of the Royal Society A: Mathematical, Physical and Engineering Sciences* 369.1940 (Apr. 2011), pp. 1396–1411. DOI: 10.1098/rsta.2010.0360.

[5] S. Mäkiharju, M. Perlin, and S. Ceccio. "On the energy economics of air lubrication drag reduction". In: *International Journal of Naval Architecture and Ocean Engineering* 4.4 (Dec. 2012), pp. 412–422. DOI: 10.2478/ijnaoe-2013-0107.

[6] B. McKeon. "The engine behind (wall) turbulence: perspectives on scale interactions". In: *Journal of Fluid Mechanics* 817 (Mar. 2017). DOI: 10.1017/jfm.2017.115.

[7] W. George. "Is there a universal log law for turbulent wall-bounded flows?" In: *Philosophical Transactions of the Royal Society A: Mathematical, Physical and Engineering Sciences* 365.1852 (Jan. 2007), pp. 789–806. DOI: 10.1098/rsta.2006.1941.

[8] D. Coles. "The law of the wake in the turbulent boundary layer". In: *Journal of Fluid Mechanics* 1.2 (July 1956), pp. 191–226. DOI: 10.1017/s0022112056000135.

[9] I. Marusic, R. Mathis, and N. Hutchins. "High Reynolds number effects in wall turbulence". In: *International Journal of Heat and Fluid Flow* 31.3 (June 2010), pp. 418–428. DOI: 10.1016/j.ijheatfluidflow.2010.01.005.

[10] P. Monkewitz, K. Chauhan, and H. Nagib. "Self-consistent high-Reynolds-number asymptotics for zero-pressure-gradient turbulent boundary layers". In: *Physics of Fluids* 19.11 (Nov. 2007), p. 115101. DOI: 10.1063/1.2780196.

[11] K. Chauhan, P. Monkewitz, and H. Nagib. "Criteria for assessing experiments in zero pressure gradient boundary layers". In: *Fluid Dynamics Research* 41.2 (Mar. 2009), p. 021404. DOI: 10.1088/0169-5983/41/2/021404.

[12] X. Wu. "Inflow turbulence generation methods". In: *Annual Review of Fluid Mechanics* 49.1 (Jan. 2017), pp. 23–49. DOI: 10.1146/annurev-fluid-010816-060322.

[13] T. Lund, X. Wu, and K. Squires. "Generation of turbulent inflow data for spatially-developing boundary layer simulations". In: *Journal of Computational Physics* 140.2 (Mar. 1998), pp. 233–258. DOI: 10.1006/jcph.1998.5882.

[14] J. Sillero, J. Jiménez, and R. Moser. "One-point statistics for turbulent wall-bounded flows at Reynolds numbers up to 2000". In: *Physics of Fluids* 25.10 (Oct. 2013), p. 105102. DOI: 10.1063/1.4823831.

[15] N. Nikitin. "Spatial periodicity of spatially evolving turbulent flow caused by inflow boundary condition". In: *Physics of Fluids* 19.9 (Sept. 2007), p. 091703. DOI: 10.1063/1.2781596.

[16] M. Simens, J. Jiménez, S. Hoyas, and Y. Mizuno. "A high-resolution code for turbulent boundary layers". In: *Journal of Computational Physics* 228.11 (June 2009), pp. 4218–4231. DOI: 10.1016/j.jcp.2009.02.031.

[17] N. Hutchins and I. Marusic. "Evidence of very long meandering features in the logarithmic region of turbulent boundary layers". In: *Journal of Fluid Mechanics* 579 (May 2007), p. 1. DOI: 10.1017/s0022112006003946.

[18] J. Lee and H. Sung. "Very-large-scale motions in a turbulent boundary layer". In: *Journal of Fluid Mechanics* 673 (Feb. 2011), pp. 80–120. DOI: 10.1017/s002211201000621x.

[19] J. Lee and H. Sung. "Comparison of very-large-scale motions of turbulent pipe and boundary layer simulations". In: *Physics of Fluids* 25.4 (Apr. 2013), p. 045103. DOI: 10.1063/1.4802048.

[20] G. Wang, X. Zheng, and J. Tao. "Very large scale motions and PM10 concentration in a high-Re boundary layer". In: *Physics of Fluids* 29.6 (June 2017), p. 061701. DOI: 10.1063/1.4990087.

[21] A. Lozano-Durán and J. Jiménez. "Effect of the computational domain on direct simulations of turbulent channels up to $Re_\tau = 4200$". In: *Physics of Fluids* 26.1 (Jan. 2014), p. 011702. DOI: 10.1063/1.4862918.

[22] O. Flores and J. Jiménez. "Hierarchy of minimal flow units in the logarithmic layer". In: *Physics of Fluids* 22.7 (July 2010), p. 071704. DOI: 10.1063/1.3464157.

[23] S. Pirozzoli and M. Bernardini. “Probing high-Reynolds-number effects in numerical boundary layers”. In: *Physics of Fluids* 25.2 (Feb. 2013), p. 021704. DOI: 10.1063/1.4792164.

[24] X. Wu, P. Moin, J. Wallace, J. Skarda, A. Lozano-Durán, and J. Hickey. “Transitional–turbulent spots and turbulent–turbulent spots in boundary layers”. In: *Proceedings of the National Academy of Sciences* 114.27 (June 2017), E5292–E5299. DOI: 10.1073/pnas.1704671114.

[25] A. Towne, O. Schmidt, and T. Colonius. “Spectral proper orthogonal decomposition and its relationship to dynamic mode decomposition and resolvent analysis”. In: *Journal of Fluid Mechanics* 847 (May 2018), pp. 821–867. DOI: 10.1017/jfm.2018.283.

[26] P. Schmid. “Dynamic mode decomposition of numerical and experimental data”. In: *Journal of Fluid Mechanics* 656 (July 2010), pp. 5–28. DOI: 10.1017/s0022112010001217.

[27] L. Abreu, A. Cavalieri, P. Schlatter, R. Vinuesa, and D. Henningson. “Resolvent modelling of near-wall coherent structures in turbulent channel flow”. In: *International Journal of Heat and Fluid Flow* 85 (Oct. 2020), p. 108662. DOI: 10.1016/j.ijheatfluidflow.2020.108662.

[28] L. Abreu, A. Cavalieri, P. Schlatter, R. Vinuesa, and D. Henningson. “Spectral proper orthogonal decomposition and resolvent analysis of near-wall coherent structures in turbulent pipe flows”. In: *Journal of Fluid Mechanics* 900 (Aug. 2020). DOI: 10.1017/jfm.2020.445.

[29] G. Rigas, E. Pickering, O. Schmidt, P. Nogueira, A. Cavalieri, G. Brès, and T. Colonius. “Streaks and coherent structures in jets from round and serrated nozzles”. In: *25th AIAA/CEAS Aeroacoustics Conference*. American Institute of Aeronautics and Astronautics, May 2019. DOI: 10.2514/6.2019-2597.

[30] S. Nakashima, K. Fukagata, and M. Luhar. “Assessment of suboptimal control for turbulent skin friction reduction via resolvent analysis”. In: *Journal of Fluid Mechanics* 828 (Sept. 2017), pp. 496–526. DOI: 10.1017/jfm.2017.519.

[31] P. Morra, K. Sasaki, A. Hanifi, A. Cavalieri, and D. Henningson. “A realizable data-driven approach to delay bypass transition with control theory”. In: *Journal of Fluid Mechanics* 883 (Nov. 2019). DOI: 10.1017/jfm.2019.793.

[32] E. Martini, A. Cavalieri, A. Towne P. Jordan, and L. Lesshafft. “Resolvent-based optimal estimation of transitional and turbulent flows”. In: *Journal of Fluid Mechanics* 900 (July 2020). DOI: 10.1017/jfm.2020.435.

[33] T. Maeder, N. Adams, and L. Kleiser. “Direct simulation of turbulent supersonic boundary layers by an extended temporal approach”. In: *Journal of Fluid Mechanics* 429 (Feb. 2001), pp. 187–216. DOI: 10.1017/s0022112000002718.

[34] Y. Guo, L. Kleiser, and N. Adams. “A comparison study of an improved temporal DNS and spatial DNS of compressible boundary layer transition”. In: *Fluid Dynamics Conference*. American Institute of Aeronautics and Astronautics, June 1994. DOI: 10.2514/6.1994-2371.

[35] M. Kozul, D. Chung, and J. Monty. “Direct numerical simulation of the incompressible temporally developing turbulent boundary layer”. In: *Journal of Fluid Mechanics* 796 (May 2016), pp. 437–472. DOI: 10.1017/jfm.2016.207.

[36] P. Spalart, and A. Leonard. “Direct numerical simulation of equilibrium turbulent boundary layers”. In: *Turbulent Shear Flows 5*. Berlin, Heidelberg: Springer Berlin Heidelberg, 1987, pp. 234–252.

[37] P. Spalart. “Direct simulation of a turbulent boundary layer up to Re_θ = 1410”. In: *Journal of Fluid Mechanics* 187.-1 (Feb. 1988), p. 61. DOI: 10.1017/s0022112088000345.

[38] B. McKeon and A. Sharma. “A critical-layer framework for turbulent pipe flow”. In: *Journal of Fluid Mechanics* 658 (July 2010), pp. 336–382. DOI: 10.1017/s002211201000176x.

[39] R. Örlü and P. Schlatter. “Comparison of experiments and simulations for zero pressure gradient turbulent boundary layers at moderate Reynolds numbers”. In: *Experiments in Fluids* 54.6 (June 2013). DOI: 10.1007/s00348-013-1547-x.

[40] P. Spalart, M. Strelets, and A. Travin. “Direct numerical simulation of large-eddy-break-up devices in a boundary layer”. In: *International Journal of Heat and Fluid Flow* 27.5 (Oct. 2006), pp. 902–910. DOI: 10.1016/j.ijheatfluidflow.2006.03.014.

[41] O. Desjardins, G. Blanquart, G. Balarac, and H. Pitsch. “High order conservative finite difference scheme for variable density low Mach number turbulent flows”. In: *Journal of Computational Physics* 227.15 (July 2008), pp. 7125–7159. DOI: 10.1016/j.jcp.2008.03.027.

[42] P. Schlatter, R. Örlü, Q. Li, G. Brethouwer, J. H. M. Fransson, A. V. Johansson, P. H. Alfredsson, and D. S. Henningson. “Turbulent boundary layers up to Re_θ =2500 studied through simulation and experiment”. In: *Physics of Fluids* 21.5 (May 2009), p. 051702. DOI: 10.1063/1.3139294.

[43] C. Sanmiguel Vila, R. Vinuesa, S. Discetti, A. Ianiro, P. Schlatter, and R. Örlü. “On the identification of well-behaved turbulent boundary layers”. In: *Journal of Fluid Mechanics* 822 (May 2017), pp. 109–138. DOI: 10.1017/jfm.2017.258.

[44] C. Tomkins and R. Adrian. "Spanwise structure and scale growth in turbulent boundary layers". In: *Journal of Fluid Mechanics* 490 (Sept. 2003), pp. 37–74. DOI: 10.1017/s0022112003005251.

[45] V. Priymak and T. Miyazaki. "Long-wave motions in turbulent shear flows". In: *Physics of Fluids* 6.10 (Oct. 1994), pp. 3454–3464. DOI: 10.1063/1.868402.

[46] K. Kim and R. Adrian. "Very large-scale motion in the outer layer". In: *Physics of Fluids* 11.2 (Feb. 1999), pp. 417–422. DOI: 10.1063/1.869889.

[47] J. del Alamo, J. Jiminez, P. Zandonade, and R. Moser. "Scaling of the energy spectra of turbulent channels". In: *Journal of Fluid Mechanics* 500 (Jan. 2004), pp. 135–144. DOI: 10.1017/s002211200300733x.

[48] M. Guala, S. Hommena, and R. Adrian. "Large-scale and very-large-scale motions in turbulent pipe flow". In: *Journal of Fluid Mechanics* 554.-1 (Apr. 2006), p. 521. DOI: 10.1017/s0022112006008871.

[49] B. Balakumar and R. Adrian. "Large- and very-large-scale motions in channel and boundary-layer flows". In: *Philosophical Transactions of the Royal Society A: Mathematical, Physical and Engineering Sciences* 365.1852 (Mar. 2007), pp. 665–681. DOI: 10.1098/rsta.2006.1940.

[50] A. Ferrante and S.E. Elghobashi. "A robust method for generating inflow conditions for direct simulations of spatially-developing turbulent boundary layers". In: *Journal of Computational Physics* 198.1 (July 2004), pp. 372–387. DOI: 10.1016/j.jcp.2004.01.016.

[51] K. Liu and R. Pletcher. "Inflow conditions for the large eddy simulation of turbulent boundary layers: A dynamic recycling procedure". In: *Journal of Computational Physics* 219.1 (Nov. 2006), pp. 1–6. DOI: 10.1016/j.jcp.2006.04.004.

[52] L. Mack. *Boundary-Layer Linear Stability Theory*. Tech. rep. Jet Propulsion Laboratory, 1984.

[53] H. Nagib, K. Chauhan, and P. Monkewitz. "Approach to an asymptotic state for zero pressure gradient turbulent boundary layers". In: *Philosophical Transactions of the Royal Society A: Mathematical, Physical and Engineering Sciences* 365.1852 (Mar. 2007), pp. 755–770. DOI: 10.1098/rsta.2006.1948.

[54] K. Rah and G. Blanquart. "A numerical forcing scheme to generate passive scalar mixing on the centerline of turbulent round jets in a triply periodic box". In: *Physical Review of Fluids* 4.12 (Dec. 2019). DOI: 10.1103/physrevfluids.4.124504.

[55] T. Oliver, N. Malaya, R. Ulerich, and R. Moser. "Estimating uncertainties in statistics computed from direct numerical simulation". In: *Physics of Fluids* 26.3 (Mar. 2014), p. 035101. DOI: 10.1063/1.4866813.

[56] B. McKeon and J. Morrison. "Asymptotic scaling in turbulent pipe flow". In: *Philosophical Transactions of the Royal Society A: Mathematical, Physical and Engineering Sciences* 365.1852 (Jan. 2007), pp. 771–787. DOI: 10.1098/rsta.2006.1945. URL: https://doi.org/10.1098/rsta.2006.1945.

[57] J. Ruan and G. Blanquart. "Error estimation of one-point statistics of a homogenized streamwise periodic boundary bayer". In: *Physical Review Fluids* (Under Review).

[58] T. Wei and J. Klewicki. "Scaling properties of the mean wall-normal velocity in zero-pressure-gradient boundary layers". In: *Physical Review Fluids* 1.8 (Dec. 2016). DOI: 10.1103/physrevfluids.1.082401.

[59] J. Ruan and G. Blanquart. "Direct numerical simulations of a statistically stationary streamwise periodic boundary layer via the homogenized Navier-Stokes equations". In: *Physical Review Fluids* 6.2 (Feb. 2021). DOI: 10.1103/physrevfluids.6.024602.

[60] R. Orlu and P. Schlatter. "Inflow length and tripping effects in turbulent boundary layers". In: *Journal of Physics: Conference Series* 318.2 (Dec. 2011). DOI: 10.1088/1742-6596/318/2/022018.

[61] J. Klewicki, P. Fife, T. Wei, and P. McMurtry. "A physical model of the turbulent boundary layer consonant with mean momentum balance structure". In: *Philosophical Transactions of the Royal Society A: Mathematical, Physical and Engineering Sciences* 365.1852 (Jan. 2007), pp. 823–840. DOI: 10.1098/rsta.2006.1944.

[62] M. Jones, T. Nickels, and M. Marusic. "On the asymptotic similarity of the zero-pressure-gradient turbulent boundary layer". In: *Journal of Fluid Mechanics* 616 (Dec. 2008), pp. 195–203. DOI: 10.1017/s0022112008004205.

[63] J. Sillero, J. Jimenez, and R. Moser. "Two-point statistics for turbulent boundary layers and channels at Reynolds numbers up to 2000". In: *Physics of Fluids* 26.10 (Oct. 2014), p. 105109. DOI: 10.1063/1.4899259.

[64] S. Hoyas and J. Jiménez. "Scaling of the velocity fluctuations in turbulent channels up to Re_τ=2003". In: *Physics of Fluids* 18.1 (Jan. 2006), p. 011702. DOI: 10.1063/1.2162185.

[65] M. Lee and R. Moser. "Direct numerical simulation of turbulent channel flow up to Re_τ=5000". In: *Journal of Fluid Mechanics* 774 (June 2015), pp. 395–415. DOI: 10.1017/jfm.2015.268.

[66] Z. Liu, R. Adrian, and T. Hanratty. "Large-scale modes of turbulent channel flow: transport and structure". In: *Journal of Fluid Mechanics* 448 (Nov. 2001), pp. 53–80. DOI: 10.1017/s0022112001005808.

[67] M. Tanahashi, S.-J. Kang, T. Miyamoto, S. Shiokawa, and T. Miyauchi. "Scaling law of fine scale eddies in turbulent channel flows up to Re_τ=800". In: *International Journal of Heat and Fluid Flow* 25.3 (June 2004), pp. 331–340. DOI: 10.1016/j.ijheatfluidflow.2004.02.016.

[68] J. Monty, N. Hutchins, H. NG, I. Marusic, and M. S. Chong. "A comparison of turbulent pipe, channel and boundary layer flows". In: *Journal of Fluid Mechanics* 632 (July 2009), pp. 431–442. DOI: 10.1017/s0022112009007423.

[69] A. Smits, B. McKeon, and I. Marusic. "High–Reynolds number wall turbulence". In: *Annual Review of Fluid Mechanics* 43.1 (Jan. 2011), pp. 353–375. DOI: 10.1146/annurev-fluid-122109-160753.

[70] R. Deshpande, J. Monty, and I. Marusic. "Streamwise inclination angle of large wall-attached structures in turbulent boundary layers". In: *Journal of Fluid Mechanics* 877 (Sept. 2019). DOI: 10.1017/jfm.2019.663. URL: https://doi.org/10.1017/jfm.2019.663.

[71] C. Higgins, M. Froidevaux, V. Simeonov, N. Vercauteren, C. Barry, and M. B. Parlange. "The effect of scale on the applicability of Taylor's frozen turbulence hypothesis in the atmospheric boundary layer". In: *Boundary-Layer Meteorology* 143.2 (Feb. 2012), pp. 379–391. DOI: 10.1007/s10546-012-9701-1. URL: https://doi.org/10.1007/s10546-012-9701-1.

[72] W. J. Baars, N. Hutchins, and I. Marusic. "Reynolds number trend of hierarchies and scale interactions in turbulent boundary layers". In: *Philosophical Transactions of the Royal Society A: Mathematical, Physical and Engineering Sciences* 375.2089 (Feb. 2017), p. 20160077. DOI: 10.1098/rsta.2016.0077.

[73] M. de Silva , N. Hutchins, and I. Marusic. "Uniform momentum zones in turbulent boundary layers". In: *Journal of Fluid Mechanics* 786 (Dec. 2015), pp. 309–331. DOI: 10.1017/jfm.2015.672.

[74] T. Nickels, I. Marusic, S. Hafez, and M. Chong. "Evidence of the k_1^{-1} law in a high-Reynolds-number turbulent boundary layer". In: *Physical Review Letters* 95.7 (Aug. 2005). DOI: 10.1103/physrevlett.95.074501. URL: https://doi.org/10.1103/physrevlett.95.074501.

[75] B. Ganapathisubramani, N. Hutchins, W. T. Hambleton, E. K. Longmire, and I. Marusic. "Investigation of large-scale coherence in a turbulent boundary layer using two-point correlations". In: *Journal of Fluid Mechanics* 524 (Feb. 2005), pp. 57–80. DOI: 10.1017/s0022112004002277. URL: https://doi.org/10.1017/s0022112004002277.

[76] D. Chandran, R. Baidya, J. Monty, and I. Marusic. "Two-dimensional energy spectra in high-Reynolds-number turbulent boundary layers". In: *Journal of Fluid Mechanics* 826 (Aug. 2017). DOI: 10.1017/jfm.2017.359. URL: https://doi.org/10.1017/jfm.2017.359.

[77] D. Squire, N. Hutchins, C. Morrill-Winter, M. Schultz, J. Klewicki, and I. Marusic. "Applicability of Taylor's hypothesis in rough- and smooth-wall boundary layers". In: *Journal of Fluid Mechanics* 812 (Dec. 2016), pp. 398–417. DOI: 10.1017/jfm.2016.832. URL: https://doi.org/10.1017/jfm.2016.832.

[78] D. Dennis and T. Nickels. "On the limitations of Taylor's hypothesis in constructing long structures in a turbulent boundary layer". In: *Journal of Fluid Mechanics* 614 (Oct. 2008), pp. 197–206. DOI: 10.1017/s0022112008003352. URL: https://doi.org/10.1017/s0022112008003352.

[79] W. Morrison and R.Kronauer. "Structural similarity for fully developed turbulence in smooth tubes". In: *Journal of Fluid Mechanics* 39.1 (Oct. 1969), pp. 117–141. DOI: 10.1017/s0022112069002072. URL: https://doi.org/10.1017/s0022112069002072.

[80] J. LeHew, M. Guala, and B. McKeon. "A study of the three-dimensional spectral energy distribution in a zero pressure gradient turbulent boundary layer". In: *Experiments in Fluids* 51.4 (May 2011), pp. 997–1012. DOI: 10.1007/s00348-011-1117-z. URL: https://doi.org/10.1007/s00348-011-1117-z.

[81] J. LeHew. "Spatio-temporal analysis of the turbulent boundary layer and an investigation of the effects of periodic disturbances". PhD thesis. 2012. DOI: 10.7907/20CM-EV70.

[82] O. Schmidt and T. Colonius. "Guide to Spectral Proper Orthogonal Decomposition". In: *AIAA Journal* 58.3 (Mar. 2020), pp. 1023–1033. DOI: 10.2514/1.j058809.

[83] J. Jiménez. "How linear is wall-bounded turbulence?" In: *Physics of Fluids* 25.11 (Nov. 2013), p. 110814. DOI: 10.1063/1.4819081.

[84] Kathryn M. Butler and Brian F. Farrell. "Three-dimensional optimal perturbations in viscous shear flow". In: *Physics of Fluids A: Fluid Dynamics* 4.8 (Aug. 1992), pp. 1637–1650. DOI: 10.1063/1.858386.

[85] J. del Álamo and J. Jiménez. "Linear energy amplification in turbulent channels". In: *Journal of Fluid Mechanics* 559 (July 2006), p. 205. DOI: 10.1017/s0022112006000607.

[86] C. Cossu, G. Pujals, and S. Depardon. "Optimal transient growth and very large–scale structures in turbulent boundary layers". In: *Journal of Fluid Mechanics* 619 (Jan. 2009), pp. 79–94. DOI: 10.1017/s0022112008004370.

[87] I. Jacobi and B. McKeon. "Dynamic roughness perturbation of a turbulent boundary layer". In: *Journal of Fluid Mechanics* 688 (Oct. 2011), pp. 258–296. DOI: 10.1017/jfm.2011.375.

[88] A. Sharma B. McKeon and I. Jacobi. “Experimental manipulation of wall turbulence: A systems approach”. In: *Physics of Fluids* 25.3 (Mar. 2013), p. 031301. DOI: 10.1063/1.4793444.

[89] E. Pickering, G. Rigas, P. Nogueira, A. Cavalieri, O. Schmidt, and T. Colonius. “Lift-up, Kelvin–Helmholtz and Orr mechanisms in turbulent jets”. In: *Journal of Fluid Mechanics* 896 (May 2020). DOI: 10.1017/jfm.2020.301.

[90] H. Bae and B. McKeon. “Characterization of vortex regeneration mechanism in the self-sustaining process of wall-bounded flows using resolvent analysis”. In: *Journal of Physics: Conference Series* 1522 (Apr. 2020). DOI: 10.1088/1742-6596/1522/1/012001.

[91] P. Morra, P. Nogueira, A. Cavalieri, and D. Henningson. “The colour of forcing statistics in resolvent analyses of turbulent channel flows”. In: *Journal of Fluid Mechanics* 907 (Nov. 2020). DOI: 10.1017/jfm.2020.802. URL: https://doi.org/10.1017/jfm.2020.802.

[92] S. Symon, S. Illingworth, and I. Marusic. “Energy transfer in turbulent channel flows and implications for resolvent modelling”. In: *Journal of Fluid Mechanics* 911 (Jan. 2021). DOI: 10.1017/jfm.2020.929. URL: https://doi.org/10.1017/jfm.2020.929.

[93] E. Pickering, G. Rigas, O. Schmidt, D. Sipp, and T. Colonius. “Optimal eddy viscosity for resolvent-based models of coherent structures in turbulent jets”. In: *Journal of Fluid Mechanics* 917 (Apr. 2021). DOI: 10.1017/jfm.2021.232. URL: https://doi.org/10.1017/jfm.2021.232.

[94] M. Luhar, A. Sharma, and B. McKeon. *Repository for all Matlab/Python Code for the Navier-Stokes Resolvent Analysis [online database]*. https://github.com/mluhar/resolvent. 2013.

[95] S. Maslowe. “Critical layers in shear flows”. In: *Annual Review of Fluid Mechanics* 18.1 (Jan. 1986), pp. 405–432. DOI: 10.1146/annurev.fl.18.010186.002201. URL: https://doi.org/10.1146/annurev.fl.18.010186.002201.

[96] S. Dawson and B. McKeon. “On the shape of resolvent modes in wall-bounded turbulence”. In: *Journal of Fluid Mechanics* 877 (Aug. 2019), pp. 682–716. DOI: 10.1017/jfm.2019.594.

[97] S. Beneddine, D. Sipp, A. Arnault, J. Dandois, and L. Lesshafft. “Conditions for validity of mean flow stability analysis”. In: *Journal of Fluid Mechanics* 798 (June 2016), pp. 485–504. DOI: 10.1017/jfm.2016.331.

[98] A. Cavalieri, P. Jordan, and L. Lesshafft. “Wave-packet models for jet dynamics and sound radiation”. In: *Applied Mechanics Reviews* 71.2 (Mar. 2019). DOI: 10.1115/1.4042736.

[99] L. Brandt. “The lift-up effect: The linear mechanism behind transition and turbulence in shear flows”. In: *European Journal of Mechanics - B/Fluids* 47 (Sept. 2014), pp. 80–96. DOI: 10.1016/j.euromechflu.2014.03.005. URL: https://doi.org/10.1016/j.euromechflu.2014.03.005.

[100] J. Jiménez. “Coherent structures in wall-bounded turbulence”. In: *Journal of Fluid Mechanics* 842 (Mar. 2018). DOI: 10.1017/jfm.2018.144.

[101] B. Farrell and P. Ioannou. “Dynamics of streamwise rolls and streaks in turbulent wall-bounded shear flow”. In: *Journal of Fluid Mechanics* 708 (Aug. 2012), pp. 149–196. DOI: 10.1017/jfm.2012.300. URL: https://doi.org/10.1017/jfm.2012.300.